Nonequilibrium polysome dynamics promote chromosome segregation and its coupling to cell growth in *Escherichia coli*

Alexandros Papagiannakis[1,2,3], Qiwei Yu[5], Sander K. Govers[1,&], Wei-Hsiang Lin[1,2,#], Ned S. Wingreen[5,6], and Christine Jacobs-Wagner[1,2,3,4]

[1]Howard Hughes Medical Institute, Stanford University, Stanford, CA 94305, USA

[2]Sarafan Chemistry, Engineering, and Medicine for Human Health Institute, Stanford University, Stanford, CA 94305, USA

[3]Department of Biology, Stanford University, Stanford, CA 94305, USA

[4]Department of Microbiology and Immunology, School of Medicine, Stanford, CA 94305, USA

[5]Lewis-Sigler Institute for Integrative Genomics, Princeton University, Princeton NJ 08544, USA

[6]Department of Molecular Biology, Princeton University, Princeton NJ 08544, USA

[&]Current address: Department of Biology, KU Leuven, Leuven, Belgium

[#]Current address: Institute of Molecular Biology, Academia Sinica, Taipei, Taiwan

*Corresponding author: email: jacobs-wagner@stanford.edu

ABSTRACT

Chromosome segregation is essential for cellular proliferation. Unlike eukaryotes, bacteria lack cytoskeleton-based machinery to segregate their chromosomal DNA (nucleoid). The bacterial ParABS system segregates the duplicated chromosomal regions near the origin of replication. However, this function does not explain how bacterial cells partition the rest (bulk) of the chromosomal material. Furthermore, some bacteria, including *Escherichia coli*, lack a ParABS system. Yet, *E. coli* faithfully segregates nucleoids across various growth rates. Here, we provide theoretical and experimental evidence that polysome production during chromosomal gene expression helps compact, split, segregate, and position nucleoids in *E. coli* through out-of-equilibrium dynamics and polysome exclusion from the DNA meshwork, inherently coupling these processes to biomass growth across nutritional conditions. Halting chromosomal gene expression and thus polysome production immediately stops sister nucleoid migration while ensuing polysome depletion gradually reverses nucleoid segregation. Redirecting gene expression away from the chromosome and toward plasmids causes ectopic polysome accumulations that are sufficient to drive aberrant nucleoid dynamics. Cell width enlargement suggest that the proximity of the DNA to the membrane along the radial axis is important to limit the exchange of polysomes across DNA-free

regions, ensuring nucleoid segregation along the cell length. Our findings suggest a self-organizing mechanism for coupling nucleoid segregation to cell growth.

INTRODUCTION

All cells must segregate their replicated chromosomes to propagate genetic information to daughter cells at division. Remarkably, this essential process is far less understood in bacteria than eukaryotes. Eukaryotic cells use the mitotic spindle, a sophisticated cytoskeleton-based machine, for chromosome segregation. No equivalent structure has been identified in bacteria, which fold their chromosomal material into a membrane-less organelle called the nucleoid. Many bacterial species use a ParABS system to segregate a specific DNA region proximal to the chromosomal origin of replication (*oriC*) (Figge et al., 2003; Ireton et al., 1994; Jalal and Le, 2020; Lim et al., 2014; Livny et al., 2007; Mohl and Gober, 1997). However, this initial step does not explain how the terminal regions of the chromosome separates (Harju et al., 2024) or how sister nucleoids move away from each other. Moreover, the chromosomally encoded *parA* and/or *parB* gene are often not essential for cell viability in various bacteria (Bartosik et al., 2009; Charaka and Misra, 2012; Donczew et al., 2016; Donovan et al., 2010; Du et al., 2016; Ireton et al., 1994; Jakimowicz et al., 2007a, 2007b; Jecz et al., 2015; Kadoya et al., 2011; Kawalek et al., 2020; Kim et al., 2000; Lagage et al., 2016; Lee and Grossman, 2006; Lewis et al., 2002; Li, 2019; Li et al., 2015; Minnen et al., 2011; Santi and McKinney, 2015; Takacs et al., 2022; Yamaichi et al., 2007; Yu et al., 2010). In fact, some bacteria do not even encode a ParABS system for *oriC* partitioning (Livny et al., 2007), with *Escherichia coli* being a prime example. Yet, *E. coli* segregates its duplicated nucleoids faithfully.

Several non-dedicated cellular processes have been proposed to play a role. For example, DNA replication may facilitate chromosome partitioning though a DNA polymerase-dependent extrusion mechanism (Lemon and Grossman, 2000). Simulations of coarse-grained polymer models have also suggested that the conformational entropy of confined circular DNA chains could provide an unmixing force that separates two mixed DNA polymers (Jun and Mulder, 2006; Jun and Wright, 2010; Pande et al., 2023). However, recent modeling work has argued that entropic forces generated from excluded volume interactions between partially replicated chromosomes inhibit (rather than promote) their segregation (Harju et al., 2024). Mechanical stress between overlapping sister nucleoids (Fisher et al., 2013) and DNA loop extrusion (Harju et al., 2024) have also been proposed to contribute to chromosome segregation. *E. coli* mutants in which the *mukB* gene required for DNA loop extrusion is deleted exhibit moderate nucleoid segregation defects linked to the organization and condensation of the nucleoid (Danilova et al., 2007; Mäkelä et al., 2021; Sawitzke and Austin, 2000). However, even in these mutants, most cells successfully segregate and partition their nucleoids between the daughter cells. Furthermore, topoisomerase I mutations or *seqA* deletion suppress the chromosome segregation defects associated with the *mukB* deletion (Danilova et al., 2007; Sawitzke and Austin, 2000; Weitao et al., 1999), suggesting that other mechanisms exist.

Furthermore, while these various proposed mechanisms likely contribute to the splitting of the nucleoid into two objects, they cannot explain how separated sister nucleoids move away from each other. In addition, the dominant mechanism underlying the nucleoid diffusional bias must somehow be coordinated with growth rate. In the presence of a poor-quality carbon source, *E. coli* initiates nucleoid segregation late in the cell division cycle. As the quality of the carbon source improves and the growth rate increases, nucleoid segregation occurs at an increasingly earlier stage of the cell division cycle until it initiates in the preceding cycle to accommodate faster division times (Bates and Kleckner, 2005; Govers et al., 2024; Tiruvadi-Krishnan et al., 2022). Jacob et al. (1963) offered an elegant solution to couple chromosome segregation to cell growth by hypothesizing that duplicated chromosomes migrate apart through membrane attachment and localized growth of the membrane between the attachment points. Drug experiments have indeed suggested that the chromosomal DNA is attached to the cytoplasmic membrane along the radial axis through a process known as transertion (Bakshi et al., 2015; Binenbaum et al., 1999; Kaval et al., 2023; Kim et al., 2024; Matsumoto et al., 2015; Spahn et al., 2023; Woldringh, 2002), which occurs when transcription, translation, and insertion of membrane proteins occur at the same time. However, for the nucleoids to migrate directionally, the 1963 model requires localized growth of the cytoplasmic membrane between the splitting nucleoids. To our knowledge, there is no evidence of such localized expansion of the inner membrane. Even if the connection between the DNA and cytoplasmic membrane extends to the peptidoglycan cell wall, *E. coli* cells elongate via a dispersed mode of peptidoglycan growth along the cell length up to the final stage of the division cycle (Cooper and Hsieh, 1988; Navarro et al., 2022; Wientjes and Nanninga, 1989; Woldringh et al., 1987). In addition, experiments with *B. subtilis* cells stripped of their cell walls indicate that nucleoid segregation does not require cell wall attachment (Wu et al., 2020). Finally, the segregation of chromosomal loci is faster than the rate of cell elongation, ruling out cell elongation and nucleoid tethering to the membrane or cell wall as a major driver of chromosome segregation (Kuwada et al., 2013).

We hypothesized that the mechanism(s) driving nucleoid segregation and its coupling to growth rate may be linked to the bacterial cellular organization. In contrast to eukaryotes, bacteria do not insulate their DNA in membrane-bound compartments. As a result, the chromosomal meshwork can freely interact with the macromolecules present in the cytoplasm, which exhibits a high level of polydispersity and crowding (McGuffee and Elcock, 2010; Zimmerman and Trach, 1991). Experiments and modeling have suggested that macromolecular crowders exert compaction forces on the compressible nucleoids through steric (i.e., excluded-volume) interactions (Mondal et al., 2011; Pelletier et al., 2012; Wu et al., 2019b; Yang et al., 2020; Zhang et al., 2009). Monosomes and polysomes (hereafter collectively referred to as “polysomes” for simplicity), which consist of mRNAs loaded with one or more translating ribosomes, constitute a sizeable and abundant cytoplasmic crowder (McGuffee and Elcock, 2010). The proteome fraction allocated to ribosomes increases with growth rate across nutrient conditions (Chure and Cremer, 2023; Dai et al., 2017; Dourado and Lercher, 2020; Hu et al., 2020; Molenaar et al., 2009; Scott et al., 2014; Si et al., 2017). The

proportion of ribosomes engaged in translation also increases with improving nutrient quality, attaining 70-80% under fast growth (Dai et al., 2017; Forchhammer and Lindahl, 1971; Mohapatra and Weisshaar, 2018; Sanamrad et al., 2014; Varricchio and Monier, 1971). These polysomes form structures (Brandt et al., 2009) of comparable or larger size than the average ~50 nm mesh size of the nucleoid (Xiang et al., 2021). Consistent with a steric clash between polysomes and the nucleoid meshwork, fluorescently-labeled ribosomes accumulate in DNA-free regions such as the cell poles and between segregated nucleoids (Azam et al., 2000; Bakshi et al., 2015, 2012; Chai et al., 2014; Gray et al., 2019; Lewis et al., 2000; Mohapatra and Weisshaar, 2018; Robinow and Kellenberger, 1994; Sanamrad et al., 2014; Xiang et al., 2021). Interestingly, theoretical work suggests that excluded-volume effects alone may be sufficient for the DNA to spontaneously phase separate from polysomes and compact into its observed nucleoid form (Mondal et al., 2011). Furthermore, a recent nonequilibrium statistical physics model proposes that nucleoid positioning and segregation could potentially be explained by the steric interaction (i.e., repulsion) between polysomes and DNA and the nonequilibrium effects associated with mRNA synthesis and degradation (Miangolarra et al., 2021). In this theoretical model, polysome accumulation in the middle of the nucleoid emerges due to polysomes born in the middle of the nucleoid taking longer to diffuse out of the nucleoid than those born closer to the nucleoid edges. Polysome accumulation beyond a certain concentration threshold drives phase separation between the DNA and polysomes at the mid-nucleoid location, resulting in nucleoid splitting. However, we lack experimental validation of this model. Furthermore, the coupling between nucleoid segregation and growth rate has not been addressed either experimentally or theoretically.

Here, we quantitatively characterize the temporal and spatial dynamics of nucleoids and polysomes in *E. coli* under different conditions and perturbations. In this work, we refer to nucleoid segregation as a series of events observable by microscopy (Figure 1A): (i) the initiation of nucleoid splitting, marked by the depletion of a DNA marker near the mid position of the nucleoid, (ii) the end of nucleoid splitting, which results in the generation of two separable nucleoid objects, and (iii) the migration of the sister nucleoids away from each other, marked by the increasing distance between the centroid of the nucleoids. This sequence of events can be initiated in the preceding cell division cycle under nutrient-rich (fast-growth) conditions. Our experimental findings, combined with modeling, provide evidence that out-of-equilibrium and asymmetric polysome rearrangements in the cell result in both DNA compaction and the choreography of the nucleoid segregation cycle during growth. The dual involvement of polysomes in protein synthesis and nucleoid dynamics ensures self-regulating coordination between cell growth and chromosome segregation across a wide range of growth rates, even under conditions where *E. coli* divides faster than it can replicate its chromosome.

RESULTS

The rate of polysome accumulation correlates with the rate of nucleoid segregation across cells.

To carefully examine the dynamics between nucleoids and polysomes with high temporal resolution (every 1 or 3 min, Figure 1 – figure supplement 1A-D), we ran time-lapse microfluidic experiments using an *E. coli* strain carrying the 50S ribosomal protein RplA fused to GFP and the nucleoid-associated protein HupA tagged with mCherry (Xiang et al., 2021). Cells were grown at 30˚C in M9 buffer supplemented with glucose, casamino acids and thiamine (M9gluCAAT). While the ribosome signal displayed the expected polar and inter-nucleoid enrichments, the accrual of ribosome signal in the middle of the cells was particularly strong compared to the polar regions, as shown by representative individual cells (Figure 1B and Movie S1) and average kymographs (Figure 1C, n = 4122 cell division cycles). Cell constriction contributed to the apparent depletion of ribosomal signal from the mid-cell region at the end of the cell division cycle (Figure 1B-C and Figure 1 – figure supplement 2). In predivisional cells, the ribosomal signal accumulated in the middle of the segregated nucleoids near the ¼ and ¾ cell positions, as shown in average one-dimensional (1D) and two-dimensional (2D) fluorescence profiles (n = 1907 predivisional cells, Figure 1D). Drug treatment and single-ribosome tracking experiments have demonstrated that ribosomal accumulations inside *E. coli* correspond to polysomes whereas free ribosomal (or ribosomal subunits) are homogeneously distributed (Bakshi et al., 2012a; Gray et al., 2019; Lewis et al., 2000; Linnik et al., 2024; Sanamrad et al., 2014; Xiang et al., 2021). This is in agreement both with our own results obtained using rifampicin (Figure 1 – figure supplement 3), a transcriptional inhibitor that causes polysome depletion over time (Blundell and Wild, 1971; Campbell et al., 2001; Hartmann et al., 1967), and with the polysome classification in cryo-electron tomograms of *E. coli* sections (Xiang et al., 2021). Since ribosomal enrichments consist of polysomes, we will therefore refer to these enrichments as polysome accumulations hereafter.

Under our relatively nutrient-rich growth conditions (M9gluCAAT), nucleoid splitting occurred early in the division cycle and occasionally initiated in the segregated nucleoids from the preceding division cycle (Movie S1 and Figure 1B). Given the variability in nucleoid segregation timing across cells (Figure 1 – figure supplement 4A), we developed a computational method to track nucleoid dynamics independently of the cell division cycle (see Methods and Figure 1 – figure supplement 4B-C). Specifically, we focused on the nucleoid cycle—defined as the period between the ends of two nucleoid splitting events (Figure 1 – figure supplement 4D)—instead of the division cycle. By tracking the accumulation of RplA-GFP and the depletion of HupA-mCherry in the middle of nucleoids, we found that polysome accumulation and nucleoid splitting correlated in time (Figure 1E). Furthermore, the rate of polysome accumulation at mid-nucleoid ($\Delta RplA_{mid\text{-}nuc}/\Delta T$) correlated with the rate of DNA depletion in the same region ($\Delta HupA_{mid\text{-}cell}/\Delta T$) at the single-cell level (ρ = -0.52, Figure 1F). This indicates that cells that accumulated polysomes faster also split their nucleoids faster. Importantly, the fitted linear regression had an intercept close to zero for both axes (Figure 1F), indicating that when the rate of polysome accumulation approached zero, so did the rate of nucleoid splitting.

181
182 To examine what happens when sister nucleoids move away from each other, we divided the time between
183 the end of nucleoid splitting and cell division into four bins. We found that right after nucleoid splitting (0-
184 25% bin), most (~70%) cells continued to accumulate polysomes at mid-cell, i.e., between the sister
185 nucleoids (Figure 1G). For these cells, the rate of polysome accumulation ($\Delta RplA_{mid\text{-}cell}/\Delta T$) positively
186 correlated with the rate of nucleoid migration ($\Delta Distance_{nuc}/\Delta T$) ($\rho = 0.47$, Figure 1H). Thus, the faster that
187 cells accumulated polysomes at mid-cell, the faster the sister nucleoids migrated apart (and vice versa).
188
189 ***Cell elongation may also contribute to sister nucleoid migration near the end of the division cycle.***
190 As noted in the Introduction, previous work has shown that the rate of chromosomal loci is faster than that
191 of cell elongation, indicating that cell elongation is not the predominant process driving chromosome
192 segregation (Kuwada et al., 2013). This interpretation is consistent with our rate measurements of nucleoid
193 segregation and cell elongation (Figure 1H). However, several observations suggest that cell elongation
194 may play a complementary role to polysome accumulations in nucleoid segregation, particularly near the
195 end of the division cycle. First, we noted that there was a substantial percentage (~30%) of cells with
196 decreasing RplA-GFP signal at mid-cell right after nucleoid splitting ($\Delta RplA_{mid\text{-}cell}/\Delta T \leq 0$, Figure 1H).
197 Interestingly, in these cells, nucleoid migration did not stop; instead, its average rate was similar to the
198 average rate of cell elongation ($\Delta Length_{cell}/\Delta T$) (Figure 1H). In fact, when the cell elongation rate was
199 subtracted from the nucleoid migration rate for each single cell (Figure 1 – figure supplement 5A), the
200 positive correlation between polysome accumulation and nucleoid migration rates remained ($\rho = 0.47$), but
201 now the average rate of nucleoid migration was near zero in cells with no polysome accumulation ($\Delta RplA_{mid\text{-}}$
202 $_{cell}/\Delta T \leq 0$).
203
204 This finding may suggest a mixed contribution between polysome accumulation and cell elongation to
205 nucleoid migration. This was interesting considering that polysomes became less enriched at mid-cell but
206 more enriched in the middle of sister nucleoids in predivisional cells (Figure 1B-D). This change
207 corresponded to a redistribution of polysome enrichments, as the average ribosome concentration
208 remained constant during the cell division cycle (Figure 1 – figure supplement 1E). This spatial change in
209 polysome enrichments was accompanied by a steady decline in the percentage of cells that continued to
210 accumulate polysomes at mid-cell between the end of nucleoid splitting and cell division (Figure 1G).
211 Concurrent with this decline, the migration rate of sister nucleoids became less correlated with the rate of
212 polysome accumulation and more correlated with the rate of cell elongation (Figure 1 – figure supplement
213 5B). To examine the relative correlation of polysome accumulation and cell elongation with nucleoid
214 migration over time, we used a linear mixed-effects model to analyze each relative nucleoid migration
215 interval (see Methods). The coefficients of the fitted mixed linear regressions suggest the following
216 hypothesis: Early during nucleoid migration (0-25% between the completion of nucleoid splitting and cell
217 division), polysome accumulation contributes most to the measured variance in the displacement of the

218 sister nucleoids (Figure 1I). This contribution progressively decreases over time while that of cell elongation
219 increases (Figure 1I). Such a switch in relative contribution would be consistent with the spatiotemporal
220 dynamics of polysome accumulation and cell wall synthesis (see Discussion).
221
222 ***Polysome accumulation at mid-cell correlates with the relative timing of nucleoid segregation***
223 ***across nutrient conditions and growth rates.***
224 If polysome production plays a role in nucleoid segregation, it predicts that the timing and amount of
225 polysome accumulation at mid-cell will correlate with the timing of nucleoid segregation across nutrient
226 conditions. To test this prediction, we analyzed images of fluorescently labeled ribosomes and nucleoids in
227 cells grown under 30 different carbon source conditions (Table S1) that vary the doubling times (~40 min
228 to ~4 h) and average cell areas (~1.9 to ~3 μm^2) of *E. coli*. This dataset included both previously published
229 (Gray et al., 2019) and new microscopy snapshots from our laboratory. Demographs generated from these
230 images revealed that the polysome accumulation at mid-cell was reproducible across all conditions and
231 strains, irrespective of the ribosomal subunit protein (RplA or RpsB) or the fluorescent tag (msfGFP, mEos2
232 or GFP) used to mark ribosomes (Figure 2A and Figure 2 – figure supplement 1). Since these profiles were
233 generated from snapshot images, they confirmed that the mid-cell polysome accumulation observed in the
234 time-lapse microfluidic experiments (Figure 1) was not caused by a photobleaching effect.
235
236 For population snapshots, nucleoids were typically imaged using DAPI (rather than a fluorescent fusion to
237 HupA), indicating that polysome accumulation at mid-nucleoid was independent of the DNA labeling
238 method. Importantly, and consistent with our prediction, the richer the growth conditions (i.e., the larger the
239 average cell area), the earlier the polysome accumulation and the nucleoid splitting occurred in the division
240 cycle based on relative cell lengths (Figure 2A and Figure 2 – figure supplement 1). In addition, the
241 polysome accumulation at mid-cell was more pronounced in nutrient-rich media (e.g., M9malaCAAT)
242 compared to nutrient-poor ones (e.g., M9mann) where the nucleoid segregated later in the division cycle
243 (Figure 2A and Figure 2 – figure supplement 1).
244
245 To quantify these phenotypes across strains and nutrient conditions, we extracted and correlated
246 population-level polysome and nucleoid statistics. We found a strong correlation (Spearman correlation ρ
247 = -0.85) between the amplitude of the average ribosomal signal accumulation and the average nucleoid
248 signal depletion at mid-cell (Figure 2B). Since the average cell area (colormap in Figure 2B) correlated with
249 the growth rate of the population (Schaechter et al., 1958), this plot also confirmed that faster growing
250 populations displayed stronger polysome accumulation and greater DNA depletion at mid-cell on average
251 (Figure 2B). This was also observed across cells within a population under the same nutritional condition
252 (ρ = -0.84, Figure 2 – figure supplement 2).
253

Both the average proteome fraction dedicated to ribosomes and the average fraction of ribosomes engaged in translation are known to correlate with growth rate across nutrient conditions (Chure and Cremer, 2023; Dai et al., 2017; Dourado and Lercher, 2020; Hu et al., 2020; Molenaar et al., 2009; Scott et al., 2014; Si et al., 2017). Thus, a role for polysome production in nucleoid segregation may provide a mechanistic link between growth rate and the relative timing of nucleoid splitting.

Spatial polysome asymmetry correlates with nucleoid positioning.

A surprising result was the apparent higher polysome accumulation at mid-cell relative to the cell pole regions (Figures 1B-C and 2A). This was not artificially created by the smaller cytoplasmic volumes at the cell poles or constriction sites due to membrane curvature (Figure 2 – figure supplement 3). It was also not caused by photobleaching artefact during the timelapse microscopy since it was also observed from snapshot images, particularly under nutrient-rich conditions (Figure 2 – figure supplement 1 and Figure 2 – figure supplement 3). The uneven distribution of polysomes suggested limited diffusion-driven equilibration of polysome concentration between the DNA-free regions. At division, such a disequilibrium could lead to a higher concentration of polysomes at the new cell pole relative to the old pole in daughter cells through inheritance. To examine this possibility, we went back to the microfluidic experiments in which we traced cell lineages from mother to daughter cells (Figure 1 – figure supplement 1A), determined the pole identity (new vs. old) of each tracked cell (Figure 1 – figure supplement 4B), and compared the polysome accumulations between the new and old poles (see Methods and Figure 3 – figure supplement 1). Old mother cells (located at the end of the microfluidic channels) and their daughters were excluded from our analysis to avoid cell aging effects (Chao et al., 2024; Coquel et al., 2013; Koleva and Hellweger, 2015; Łapińska et al., 2019; Lindner et al., 2008; Proenca et al., 2019). We found that newborn cells had more polysomes at the new pole compared to the old one on average (Figure 3A), consistent with the notion that polysomes do not rapidly equilibrate in concentration between DNA-free regions through diffusion.

Across cells, the polysome distribution asymmetry between cell poles negatively correlated with the position of the nucleoid in newborn daughter cells (Figure 3B, cells always oriented with the new pole to the right). The *x* and *y* intercepts of a fitted linear regression to the data were not zero, indicating that a nucleoid positioned precisely at the cell center did not equate with an even distribution of polysomes between poles. Instead, newborn cells with centrally located nucleoids tended to have more polysomes at the new pole compared to the old pole (example #1 in Figure 3B-C) whereas cells born with symmetric polysome enrichments between poles tended to display an off-center nucleoid closer to the new pole (example #2 in Figure 3B-C).

Spatial polysome asymmetry correlates with asymmetric nucleoid compaction in newborn cells.

Construction of average 2D cell projections of the RplA-GFP signal in cells sorted based on their relative timing to cell division confirmed the polysome asymmetry between poles in newborn cells (Figure 3D and

291 Movie S2). Strikingly, the corresponding 2D projections of the HupA-mCherry signal revealed another
292 spatial asymmetry, this time, in the average DNA mass distribution along the nucleoid length (axial
293 asymmetry). The average HupA-mCherry signal concentration was higher toward the new pole right after
294 birth or, correspondingly, toward the middle of the cell (future new pole) in the period prior to division (Figure
295 3D and Movie S2). Quantification of this axial asymmetry in newborn cells revealed that the HupA-mCherry
296 concentration is ~20% higher toward the new pole on average (Figure 3E), suggesting that the DNA density
297 is uneven along the nucleoid length. This nucleoid mass asymmetry emerged late in the nucleoid migration
298 cycle, typically before cell division such that it was inherited by newborn cells (Figure 3D).
299
300 To examine if features of polysome accumulations (e.g., position, amplitude, or fraction of cell length
301 covered) correlate with the asymmetric nucleoid density and its variability among cells, we used a linear
302 mixed-effects model (see Methods). We found that in newborn cells, the positions of polysome enrichments
303 in the old-pole and mid-cell regions significantly correlated with the HupA-mCherry density asymmetry
304 (Figure 3 – figure supplement 2). Guided by this finding, we hypothesized that the positions of the
305 accumulating polysomes along the cell length determine the space available for the chromosome to occupy
306 and thereby dictate the DNA density distribution along the nucleoid. To examine this hypothesis, we
307 combined the correlated polysome accumulation characteristics into a compound statistic that describes
308 the relative polysome-free space between two cell halves (see Methods). Compared to other polysome
309 statistics, the relative availability of cell space depleted of polysomes (RplA-GFP signal) correlated most
310 strongly with the asymmetric distribution of DNA (HupA-mCherry signal) in newborn cells (Figure 3F). In
311 other words, the DNA concentration was higher in cell regions with more space available between polysome
312 enrichments. In most (~60%) cells, the distance between polysome enrichments, and thus the DNA
313 concentration along the nucleoid, was greater between mid-cell and the new pole (i.e., x and y values >1,
314 example #1 in Figure 3F-G). The opposite pattern was true for a small fraction (~14%) of cells, where the
315 larger distance between polysome enrichments was located between mid-cell and the old pole (x and y
316 values < 1, example #2 in Figure 3F-G). Thus, polysome asymmetry correlates with asymmetric nucleoid
317 compaction.
318
319 ***A minimal reaction-diffusion model generates experimentally observed cellular asymmetries and***
320 ***growth rate-dependent nucleoid segregation.***
321 Our single-cell correlative studies were consistent with exclusion between polysomes and DNA contributing
322 to nucleoid compaction and segregation. However, it remained unclear whether the same mechanism could
323 also explain the growth rate-dependent trends and cellular asymmetries that we observed (Figures 2 and
324 3). Therefore, we built a minimal reaction-diffusion model (see Methods) to describe the dynamics of
325 polysomes and DNA during the cell cycle based on previous work (Miangolarra et al., 2021). Our model
326 takes into account two ingredients important for nucleoid segregation: effective repulsion between DNA and
327 polysomes from steric effects (described by the Cahn-Hilliard theory) and the nonequilibrium processes of

328 polysome synthesis and degradation (described by linear reaction kinetics). The model is based on realistic
329 parameters of polysome diffusion, production, and degradation (see Methods). We assume polysome
330 production (i.e., mRNA synthesis and ribosome loading) to be uniform within the nucleoid and polysome
331 degradation (i.e., mRNA decay) to be uniform across the entire cell (from pole to pole). These assumptions
332 consider the most trivial scenarios (see Discussion for other scenarios). We also assume that the cell grows
333 exponentially and that the nucleoid expands in size proportionally to the cell during growth, which has been
334 experimentally verified (Campos et al., 2014; Govers et al., 2024; Gray et al., 2019). Since *E. coli* grows
335 along its long axis and polysomes do not readily diffuse around the nucleoid to equilibrate (Figure 3A-D and
336 Figure 2 – figure supplement 3), we reduced the problem to one dimension, the cell length. Importantly, the
337 system is driven out of equilibrium by the continuous production and degradation of polysomes. It operates
338 at a nonequilibrium steady state even at fixed cell length.
339
340 First, for simplicity and illustrative purposes, we considered the case of a non-growing virtual cell with the
341 nucleoid initially spread throughout most of the cell to show that the repulsion between polysomes and DNA
342 is sufficient to both demix (phase separate) these two macromolecules and compact the nucleoid when the
343 simulation reaches steady state (Figure 4A). The compaction force originates from the nucleoid/polysome
344 steric repulsion (which drives the phase separation). The resulting higher concentration of polysomes on
345 each side of the nucleoid produces a difference in osmotic pressure that condenses the nucleoid. This
346 compaction force is consistent with drug experiments. Depletion of polysomes through inhibition of
347 transcription with rifampicin leads to nucleoid expansion whereas stabilization of polysomes through
348 inhibition of ribosome translocation with chloramphenicol results in greater nucleoid compaction (Bakshi et
349 al., 2014; Cabrera et al., 2009; Farrar et al., 2025; Spahn et al., 2023, 2018, 2018; Stracy et al., 2015; Xiang
350 et al., 2021). In the case of chloramphenicol, fusion of nucleoids has been reported (Bakshi et al., 2014;
351 Spahn et al., 2023). This phenomenon is expected to occur for nucleoids in close proximity at the time of
352 chloramphenicol treatment. These nucleoids may touch through diffusion (thermal fluctuation) and fuse to
353 reduce their interaction with the polysomes and minimize their conformational energy. Well-separated
354 nucleoids typically did not fuse. Since division could still occur during chloramphenicol treatment, the lack
355 of fusion between well-separated condensed nucleoids was more evident in filamenting cells inhibited for
356 cell division by cephalexin (Figure 4 – figure supplement 1).
357
358 Next, we tested whether adding cell growth to our model recapitulates the experimental observations.
359 Simulations showed that polysomes accumulate in the middle of the nucleoid during growth (Figure 4B and
360 Movie S3, left panel). This is followed by division of the nucleoid into two entities, which then move apart
361 from each other as polysomes accumulated between them. Thus, the model provides a minimal mechanism
362 for nucleoid segregation: At any given point, polysomes that form in the middle of the nucleoid have a lower
363 probability of escaping the nucleoid through diffusion compared to polysomes born at the edge of the
364 nucleoid (Figure 4C). Consequently, the polysome concentration rises monotonically towards the center of

the nucleoid, with its level increasing with nucleoid length (quadratically in the quasi-steady-state limit). Once the mid-cell polysome concentration reaches a threshold (the spinodal concentration), phase separation occurs spontaneously (i.e. via spinodal decomposition), creating a new polysome-rich phase that splits the nucleoid in two. Compared to regions near the poles, this new phase has a higher polysome concentration and therefore a higher osmotic pressure. This pressure difference results in a net poleward force on the sister nucleoids that drives their migration toward the poles (Figure 4B and Movie S3, left panel). Therefore, both phase separation (due to the steric repulsion described above) and nonequilibrium polysome production and degradation (which creates the initial accumulation of polysomes around midcell) are essential ingredients for nucleoid segregation.

We wondered whether our simple model could also explain the correlation between growth rate and the relative timing of nucleoid segregation (Govers et al., 2024). Therefore, we performed simulations for different growth rates, matching the cell and nucleoid length at birth with population-level measurements (Figure 4 – figure supplement 2). To initialize each simulation in a realistic fashion, we used the last timepoint (i.e., half of the predivisional cell) of the previous simulation as initial conditions, capturing the new/old pole identity as well as any cellular asymmetries inherited between generations. The relative timing of nucleoid splitting was measured as nucleoid depletion at mid-cell. We found that our model successfully captures the negative trend between the growth rate and the relative timing of nucleoid splitting. Simulated cells that grew faster also split their nucleoids earlier from birth to division, agreeing with population-level data (Figure 4D and Movie S3). The same simulations also reproduced the relatively constant cell length at which nucleoid splitting occurs across different growth rates (Figure 4 – figure supplement 3), which was previously discovered in population-level measurements (Govers et al., 2024). These phenomenological principles are expressions of the link between the absolute nucleoid length and the rate of polysome accumulation in the middle of the nucleoid, which is explained by our mechanistic model.

To examine a potential origin for the asymmetries in polysome distribution and nucleoid compaction that we observed (Figure 3), we examined the effect of the nucleoid diffusion coefficient D_{n}, which is a model parameter that describes how fast the nucleoid relaxes towards its equilibrium configuration. Large D_{n} represents the quasi-steady-state limit where the nucleoid relaxation time scale is much shorter than the cell doubling time, and the nucleoid always assumes its (symmetric) equilibrium state. Conversely, small D_{n} (i.e., slower relaxation time) can lead to asymmetric concentration profiles that will be inherited by the daughter cells. Consistent with this expectation, we found that during relatively fast growth (~40 min doubling time), a lower nucleoid diffusion coefficient results in a larger deviation from the equilibrium concentration profiles for the nucleoid and polysomes (dotted curves vs. solid curves, Figure 4E). In fact, at diffusion coefficients below 0.005 $\mu m^2/s$, the model (Figure 4E) reproduced the experimentally observed asymmetries, including the nucleoid position offset towards the new pole at birth, the higher polysome concentration at the new pole compared to the old one, and the asymmetric nucleoid compaction (Figure

402 3). Our minimal model thus suggests that the material properties of the nucleoid (e.g., stiffness) may
403 contribute to the observed nucleoid and polysome asymmetries in *E. coli* (see Discussion).
404
405 ***Polysomes accumulate at mid-nucleoid in DNA regions inaccessible to freely diffusing particles of***
406 ***similar sizes.***
407 In the model, the early polysome accumulation in the middle of nucleoid is caused by the nonequilibrium
408 processes of polysomes being born within the nucleoid while being degraded uniformly across the cell (due
409 to mRNA turnover). It predicts that the early mid-nucleoid enrichment of polysome signal observed in our
410 experiments is the product of such nonequilibrium processes rather than of polysomes simply diffusing into
411 undetected DNA-free space. If this is correct, freely diffusing objects of similar sizes to polysomes should
412 accumulate at mid-cell after polysomes accumulate there, i.e., after free DNA-space has been generated
413 through nucleoid splitting. To test this expectation, we compared the average distribution of RplA-msfGFP
414 with that of freely diffusing mCherry-labeled μNS particles from snapshot images of DAPI-stained cells
415 (Figure 5A). These μNS particles consist of a fragment of a mammalian reovirus protein (Broering et al.,
416 2005, 2002) that self-assembles into a particle, typically one per cell, when produced orthogonally in *E. coli*
417 (Parry et al., 2014). They have sizes between 50 and 200 nm (Parry et al., 2014; Xiang et al., 2021) similar
418 to polysomes (Brandt et al., 2009; Slayter et al., 1968) and are therefore largely excluded by the nucleoid
419 mesh (Xiang et al., 2021). After sorting cells by length into four bins, the positions of mCherry-labeled μNS
420 particles from approximately 2580 cells per bin were superimposed using the relative cellular coordinates
421 to construct particle density maps. Cells were randomly oriented in this analysis (meaning that asymmetries
422 between poles cannot be observed), as the pole identity cannot be assigned from snapshot images.
423
424 We found that in the shortest (i.e., newborn) cells, RplA-msfGFP-labeled polysomes had already
425 accumulated within the nucleoid (Figure 5B, bin 1). In contrast, mCherry-μNS particles were restricted to
426 the cell poles and were not able to access the mid-cell region until after nucleoid splitting was clearly visible
427 (Figure 5B, bins 2-4). This was also shown in the corresponding 1D average concentration and particle
428 density profiles (Figure 5C). These observations support the notion that the early mid-nucleoid
429 accumulation of RplA-msfGFP is caused by nonequilibrium effects associated with polysome synthesis and
430 degradation rather than polysome diffusion into DNA-free space.
431
432 ***Arrest of polysome production immediately stops nucleoid segregation while polysome depletion***
433 ***gradually reverses it.***
434 Our correlative analyses and model (Figures 1-4) support the hypothesis that the interactions and ensuing
435 exclusion between polysomes and nucleoid promote nucleoid segregation and macromolecular
436 asymmetries along the cell length. To probe causality, we used two tests. The first one aimed to disrupt the
437 proposed mechanism using rifampicin. Rifampicin treatment is known to homogenize ribosome distribution
438 and expand the nucleoid over time through polysome depletion (Bakshi et al., 2014; Dworsky and

439 Schaechter, 1973; Koch and Gross, 1979; Pettijohn and Hecht, 1974; Xiang et al., 2021). However, our
440 hypothesis predicts a faster effect on nucleoid segregation. Blocking transcription should instantly reduce
441 the rate of polysome production to zero, causing an immediate arrest of nucleoid segregation. Gradual
442 depletion of the existing polysomes due to mRNA decay should then cause, on a slower time scale, a
443 dissipation of the phase separation between DNA and ribosomes.
444
445 To test these predictions, we subjected cells growing in M9gluCAAT in microfluidic channels to two rounds
446 of rifampicin treatment (Figure 6A and Movie S4). Rifampicin resulted in growth rate inhibition (Figure 6A)
447 and changes in the nucleoid area and nucleoid-to-cell area (NC) ratio (Figure 6 – figure supplement 1), as
448 previously described (Bakshi et al., 2014; Dworsky and Schaechter, 1973; Koch and Gross, 1979; Pettijohn
449 and Hecht, 1974; Xiang et al., 2021). In cells that completed their division cycle before antibiotic addition
450 (squares and fitted blue curve in Figure 6B), the distance between the intensity peak of each sister nucleoid
451 increased monotonically between birth and division, displaying the dynamics of normal, unperturbed
452 nucleoid segregation. Cells born 22 min to 12 min before the treatment (circles in Figure 6B) experienced
453 the same nucleoid segregation dynamics up to the time of rifampicin addition. Exposure to rifampicin led to
454 the near-immediate arrest of nucleoid segregation (Figure 6B), consistent with our prediction.
455
456 Interestingly, the distance between the sister nucleoids remained the same for close to 30 min into
457 rifampicin treatment, after which it started to decrease (Figure 6B). Average 1D and 2D cell projections of
458 the scaled (divided by the whole cell average) RplA-GFP and HupA-mCherry concentration suggest that
459 the time delay between the arrest in nucleoid segregation and its reversal is likely due to the compressible
460 nature of the nucleoid, which has been demonstrated in vitro (Pelletier et al., 2012). As the polysomes in
461 the middle of the cells started to visibly deplete (> 6 min after rifampicin addition), the DNA signal expanded
462 to fill the emerging available space without affecting the distance between the peaks of the sister nucleoids
463 (white crosses, Figure 6C). This is consistent with the removal of a compaction force exerted by the
464 accumulating polysomes on the soft nucleoid. About 30 min after rifampicin addition and further polysome
465 depletion, the peak signals of the sister nucleoids (white crosses, Figure 6C) started migrating closer to
466 each other. Eventually, after 1 h of rifampicin treatment, when the RplA-GFP fluorescence was
467 homogeneous, the two nucleoid objects fused into one (Figure 6C), consistent with the dissipation of phase
468 separation.
469
470 These results support the notion that in untreated cells, polysome accumulation effectively exerts a force
471 on the compressible nucleoid, which translates into its observed compaction and translocation (hence,
472 segregation). Gradual polysome depletion through rifampicin treatment progressively decreased this effect,
473 reversing the process. This reversal became obvious when we plotted the correlation between the relative
474 polysome accumulation and nucleoid depletion at mid-cell for two cell lineages that experienced rifampicin
475 at different times after birth (Figure 6D). Irrespective of their birth time (12 or 3 min before the addition of

476 rifampicin), the negative correlation between the two variables was reversed ~9 min after the addition of
477 the antibiotic, following the same path as for the untreated cells but in the opposite direction (Figure 6D).
478 Polysome depletion during rifampicin treatment also resulted in correlated loss of asymmetric nucleoid
479 compaction in newborn cells (Figure 6E). Altogether, these results support the notion that the asymmetric
480 accumulation of polysomes results in an anisotropic force that asymmetrically compacts and segregates
481 nucleoids.
482
483 ***Ectopic polysome production redirects nucleoid dynamics.***
484 Our second approach to test causality experimentally was to redirect polysome production away from the
485 chromosome to achieve polysome accumulation at an ectopic site. To achieve polysome accumulation at
486 ectopic sites in experiments, we overexpressed a useless protein (mTagBFP2) for the cell from a T7
487 promoter on a multi-copy pET28 plasmid (Figure 7A). The resulting CJW7798 strain also carried the
488 ribosome (RplA-msfGFP) and DNA (HupA-mCherry) markers. We reasoned that high expression of BFP2
489 from the plasmid would slow polysome production within the nucleoid and create polysome accumulations
490 at ectopic cellular locations through recruitment of ribosomes to plasmid transcripts. This, in turn, should
491 affect nucleoid dynamics according to our model.
492
493 Plasmid expression of mTagBFP2 was induced by addition of 100 μM IPTG and expression of a
494 chromosomally encoded T7 RNA polymerase (Figure 7B). The gradual increase of mTagBFP2
495 fluorescence in the cells was associated with a concomitant decrease in cell growth rate (Figure 7C),
496 consistent with reduced gene expression from the chromosome. We verified by flow cytometry that
497 induction did not block DNA replication. IPTG-induced cells displayed a similar scaling relationship between
498 the intensity of DNA (labeled with DRAQ5) and cell size (side scatter area) than uninduced cells (Figure 7
499 – figure supplement 1).
500
501 We found that induced cells displayed various patterns of polysome accumulations (Movie S5), presumably
502 due to stochastic clustering of plasmids in DNA-free regions as previously reported for multi-copy plasmids
503 devoid of DNA partitioning genes (Hsu and Chang, 2019; Reyes-Lamothe et al., 2014; Yao et al., 2007).
504 Importantly, the ectopic accumulations of polysomes had a drastic effect on nucleoid dynamics. In some
505 cells, polysomes accumulated at one pole instead of the middle of the nucleoid, preventing the nucleoid
506 from splitting (Figure 7D). Expansion of the polysome accumulation at a pole effectively pushed the nucleoid
507 toward the opposite pole of the cell. In other cells, polysome accumulation occurred between sister
508 nucleoids, but did not relocate to the segregated nucleoids at the ¼ and ¾ cell positions. Rather, polysome
509 accumulation persisted and expanded between the sister nucleoids, effectively further pushing them apart
510 (Figure 7E). Both of these phenotypes were reproduced by our model when we intentionally caused an
511 accumulation of polysomes, either at a pole or between segregated nucleoids (Figure 7 – figure supplement
512 2). In our experiments we also observed filamenting cells with correlated polysome and nucleoid dynamics

513 that changed in time (Figure 7F), resulting in transient events of nucleoid fusion, splitting, or changes in
514 migration direction depending on where polysomes accumulated. Movie S5 shows additional examples of
515 such dependency.
516
517 Upon induction, we observed the appearance of diffuse mTagBFP2 fluorescence (Figure 7B). We also
518 observed the formation of inclusion bodies (bright phase contrast) that typically remained at a pole or
519 sometimes moved along the edge of a growing polysome accumulation (Figure 7F). After a long of period
520 of IPTG induction (> 8 h), polysome accumulation eventually decreased, leading to nucleoid decompaction
521 (Figure 7 – figure supplement 3).
522
523 This experiment effectively decoupled polysome accumulation from cell growth. By redirecting a substantial
524 fraction of chromosome gene expression to a single plasmid-encoded gene, we reduced the rate of cell
525 growth but still created a large accumulation of polysomes at an ectopic location. This ectopic polysome
526 accumulation was sufficient to affect nucleoid dynamics in a correlated fashion. Altogether, these results
527 support the notion that ectopic polysome accumulation drives nucleoid dynamics.
528
529 ***Cell width enlargement leads to nucleoid splitting along the incorrect cell axis and to the fusion of***
530 ***polysome accumulations from distinct DNA-free regions.***
531 A previous study on *Bacillus subtilis* L-forms suggests that the width of the cell is also important for nucleoid
532 segregation (Wu et al., 2020). In that study, L-forms, which are spherical cells stripped of their cell wall,
533 were squeezed into narrow microfluidic channels of similar width than the diameter of walled rod-shaped
534 cells. Growth in these channels resulted into elongated cells with improved efficiency in nucleoid
535 segregation (Wu et al., 2020). In normal (walled) cells, the nucleoid is kept close to the cytoplasmic
536 membrane across the cell width, likely due to transertion (co-transcriptional translation and translocation of
537 membrane and secreted proteins) (Bakshi et al., 2014; Spahn et al., 2023; Youngren et al., 2014). We
538 reasoned that this geometric constraint reproduces some important aspects of our simple model. The
539 nucleoid proximity to the cell membrane along the cell width ensures that the nucleoid grows exclusively
540 along one dimension, the cell length. Furthermore, the nucleoid attachment to the membrane along this
541 radial cell axis may act as a diffusion barrier and limit polysome exchange between distinct DNA-free
542 regions.
543
544 To test these ideas, we first treated cultures with A22 to inhibit cell width control through the inactivation of
545 MreB (Bean et al., 2009; Iwai et al., 2002). This resulted in cells with a polysome phase at the cell center
546 surrounded by a nucleoid phase around the cell periphery (Figure 8 – figure supplement 1, top). The
547 peripheral nucleoid localization is likely due to membrane attachment through transertion, as previously
548 shown (Spahn et al., 2023). To further increase the cell width (> 2.5-fold), we exposed cells to the cell
549 division inhibitor cephalexin in addition to A22 (Figure 8A and Figure 8 – figure supplement 1, bottom). As

550 a control, we showed that cephalexin treatment alone resulted in filamentous cells (of constant cell width)
551 with multiple nucleoids separated by polysome accumulations (Figure 8B), consistent with previous reports
552 (Chai et al., 2014; Gray et al., 2019; Thappeta et al., 2024). In cells treated with both drugs, we observed
553 two types of subcellular rearrangements. In smaller cells, which started with a single nucleoid, drug
554 treatment resulted in a single large polysome accumulation at the cell center, with the nucleoid displaying
555 a toroidal shape at the cell periphery (Figure 8C and Movie S6). In longer cells with two segregated
556 nucleoids, the nucleoids expanded and often aberrantly segregated along the cell width concomitant with
557 polysome accumulation at the site of nucleoid splitting (white arrowheads, Figure 8D). Consequently, a
558 polysome "bridge" was formed between the polysome accumulations flanking the nucleoid. These
559 polysome bridges resulted in a characteristic cross-like polysome pattern, marking the two axes
560 (longitudinal and radial) of nucleoid segregation (Figure 8E). Cell width enlargement led to coalescence of
561 polysome accumulations toward the cell center and fusion of nucleoids around the cell periphery (Figure
562 8C-E and Figure 8 – figure supplement 1, bottom). As a result, the nucleoids and polysome accumulations
563 decreased in number while increasing in size in cephalexin/A22-treated cells compared to cephalexin-
564 treated cells with the same cell area distribution but normal cell width (Figure 8F). These results suggest a
565 critical role for cell width regulation in limiting the diffusion of polysomes around the nucleoid, thereby
566 promoting nucleoid segregation specifically along the cell length.
567
568 **DISCUSSION**
569 ***The flow of genetic information intrinsically couples nucleoid segregation to cell growth.***
570 This study provides experimental and theoretical evidence (Figures 1-8) that polysome production within
571 the nucleoid—an inherent product of chromosomal gene expression—contributes to nucleoid segregation
572 and positioning in *E. coli* cells. This may also be true in other bacteria, as reduced or abrogated transcription
573 via gene deletion or antibiotic treatment causes chromosome segregation defects in *Streptococcus*
574 *pneumoniae* (Kjos and Veening, 2014) and *Bacillus subtilis* (Dworkin and Losick, 2002).
575
576 An appealing feature of this proposed model is that polysomes inherently integrate the rate of nucleoid
577 segregation with that of gene expression and cell growth. The concentration of polysomes and their rate of
578 accumulation in the cell are a direct reflection of transcriptional and translational activities in the cell
579 (Balakrishnan et al., 2022). The higher the concentration of polysomes, the faster the growth rate becomes.
580 Thus, in our proposed model, an increase in polysome concentration not only leads to more protein
581 synthesis and faster cell growth but also results in faster nucleoid segregation. The reverse is true for a
582 decrease in polysome concentration, inherently coupling these processes without the help of a dedicated
583 regulatory system. Such coupling was observed across isogenic cells with variable growth rates in the same
584 nutrient condition (Figure 2 – figure supplement 2) as well as across nutrient conditions that led to a wide
585 range of growth rates (Figure 2 and Figure 2 – figure supplement 1).
586

587 ***Directional nucleoid splitting requires DNA/polysome exclusion and cell width control.***
588 A key aspect of our proposed mechanism for nucleoid segregation is that polysomes form within nucleoids
589 due to chromosomal gene expression, which, together with polysome turnover due to mRNA decay, creates
590 an out-of-equilibrium system (Figure 4) (Miangolarra et al., 2021). Redirecting polysome formation to
591 plasmid gene expression leads to ectopic polysome accumulations that is sufficient to alter nucleoid
592 dynamics (Figure 7 and Movie S5).
593
594 In normal cells, the effective force that segregates nucleoids appears to be linked to the propensity of the
595 chromosomal meshwork and polysomes to separate from each other. Mutual exclusion is, at least in part,
596 caused by the steric repulsion between the two macromolecules. While ribosomes or ribosomal subunits
597 freely diffuse across the cell unobstructed by the presence of the nucleoid (Bakshi et al., 2012; Sanamrad
598 et al., 2014), the larger polysomes are impeded by the chromosomal mesh based on size considerations
599 alone (Xiang et al., 2021). Modeling studies have suggested that such steric hinderance between large
600 crowders (polysomes) and a polymeric meshwork (chromosome) can result in phase separation and
601 polymer compaction (Bakshi et al., 2014; Castellana et al., 2016; Miangolarra et al., 2021; Mondal et al.,
602 2011; Wu et al., 2019b). Theoretically, mRNAs alone are large enough to phase separate from DNA, though
603 to a lesser degree than polysomes (Miangolarra et al., 2021). It is also possible that phase separation
604 between nucleoids and polysomes (or mRNAs) involves non-steric interactions such as electrostatic
605 repulsion between the negatively charged DNA and RNA (mRNA and rRNA), as previously hypothesized
606 (Joyeux, 2015). Such steric and non-steric interactions may contribute to the effective poor solvent quality
607 of the polysome-rich cytoplasm for the chromosome (Xiang et al., 2021). Future research will be necessary
608 to elucidate the precise nature of the interaction between chromosomes and mRNAs, whether individually
609 or in complex with ribosomes.
610
611 We found that the width of the cell controls the exclusion dynamics between polysomes and nucleoids by
612 directing nucleoid growth and segregation along a single cellular dimension, cell length (Figure 8). The
613 close proximity of the nucleoid to the membrane presumably due to transertion (Bakshi et al., 2014;
614 Rabinovitch et al., 2003; Spahn et al., 2023) effectively limits the diffusion and fusion of polysome
615 accumulations from distinct DNA-free regions, which leads to alternating enrichments of polysomes and
616 DNA along the length of elongating cells (Figure 8B). Limited polysome diffusion around the nucleoids is
617 consistent with the observed differences in ribosome concentrations between DNA-free regions (Figure 3A-
618 B, and D). Otherwise, we would expect polysome enrichments on each side of the nucleoids to rapidly
619 equilibrate in concentration. Diffusion limitation around nucleoids is consistent with our previous report that
620 polysomes diffuse much faster over short distances (within DNA-free domains) than long distances (across
621 DNA-free domains) (Gray et al., 2019). Control of cell width is vital to uphold this constraint and promote
622 that nucleoid grows along a single cell axis. This explains the drastic improvement in nucleoid segregation
623 of wall-less cells (L-forms) when compressed to normal width (Wu et al., 2020). It highlights the importance

624 of cell width regulation and suggests that nucleoid segregation may have imposed an evolutionary
625 constraint on cell width control.
626
627 ***Nucleoid segregation likely involves multiple factors.***
628 The model shows that the most trivial case of uniform production of polysomes (i.e., uniform mRNA
629 synthesis) within the nucleoid is sufficient to cause an enrichment of polysomes at mid-nucleoid (Figure 4)
630 (Miangolarra et al., 2021). Inside cells, this polysome enrichment at mid-nucleoid may be enhanced by a
631 bias in mRNA synthesis across the nucleoid. For instance, the chromosomal region close to the origin of
632 replication has been shown to be more highly expressed per gene copy than other regions on the
633 chromosome (Scholz et al., 2019) and this region is located in the middle of the nucleoid prior to DNA
634 replication (Bates and Kleckner, 2005; Cass et al., 2016; Fisher et al., 2013; Kuwada et al., 2013, 2013;
635 Mäkelä et al., 2021; Sadhir and Murray, 2023; Wang et al., 2006). In addition, this highly expressed
636 chromosomal region is the first one to replicate, which should lead to further local increase in mRNA
637 expression due to a doubling in gene dosage (Pountain et al., 2022). We did not consider such localized
638 mRNA synthesis in our model. However, if we did, it would only help the mechanism that we proposed by
639 increasing the polysome built-up at mid-nucleoid.
640
641 Other factors are likely involved in nucleoid segregation. In fact, our data revives the largely abandoned
642 sixty-year-old hypothesis by Jacob et al. (1963) that cell growth separates the sister nucleoids through their
643 potential attachment to the cell wall, but with two notable differences. First, the contribution of cell growth
644 to nucleoid splitting would be minor relative to the polysome contribution (Figure 1I and Figure 1 – figure
645 supplement 5). Second, cell growth would contribute predominantly near the end of the division cycle
646 (Figure 1I). This late timing would be attractive for two reasons. First, it corresponds to the time when
647 polysomes stop accumulating between the separated sister nucleoids and polysome accumulations
648 emerge at the middle of these nucleoids (i.e., at the ¼ and ¾ cell positions) to start the next round of
649 segregation (Figure 1D and Movie S2). Second, this is also when *E. coli* switches its cell wall growth pattern
650 from dispersed along the cell body to zonal and divisome-dependent at mid-cell (Cooper and Hsieh, 1988;
651 Gray et al., 2015; Navarro et al., 2022; Wientjes and Nanninga, 1989; Woldringh et al., 1987). Indeed, zonal
652 cell growth between the sister nucleoids was a key assumption of the 1963 model (Jacob et al., 1963).
653 What is not entirely clear is how the DNA would be attached to the peptidoglycan cell wall. Transertion links
654 the DNA to the cytoplasmic membrane. Perhaps the coupling between transcription, translation, and
655 membrane insertion extends to peptidoglycan binding.
656
657 Beyond cell elongation, thermodynamic demixing and other cellular processes such as DNA replication,
658 loop extrusion, supercoiling, and preferential loading of DNA remodeling complexes are also likely to be
659 important for robust chromosome segregation and organization (Danilova et al., 2007; Harju et al., 2024;
660 Hofmann et al., 2019; Holmes and Cozzarelli, 2000; Lemon and Grossman, 2000; Mäkelä et al., 2021;

661 Minnen et al., 2011; Sawitzke and Austin, 2000; Weitao et al., 1999; Wu et al., 2019a; Youngren et al.,
662 2014).
663
664 We note that in our time-lapse experiments, the accumulation of polysome signal appeared to slightly
665 precede the depletion of DNA signal that marked the initiation of nucleoid splitting (Figure 1E). Polysome
666 enrichment in the middle of unconstricted nucleoids was also occasionally observed in snapshot images of
667 cells growing on glycerol, a slow growth condition that results in a single nucleoid segregation event late
668 during the cell division cycle (Figure 1 – figure supplement 6). This is not seen in our model in which
669 polysome accumulation and nucleoid splitting occur at the same time (Figure 4B and Movie S3). This small
670 discrepancy may reflect a limitation of our experimental or modeling approach. For example, it is possible
671 that the point spread function of our fluorescent DNA marker slightly delays the moment at which we can
672 detect signal depletion at mid-nucleoid and thereby the initiation of nucleoid splitting. Alternatively, the small
673 difference in timing may be associated with a model simplification. In our model, the nucleoid is effectively
674 a solution of DNA fragments. In reality, the nucleoid consists of a circular polymer, crosslinked by nucleoid-
675 associated proteins. These DNA crosslinks may cause a small resistance that marginally delays the
676 initiation of nucleoid splitting relative to the polysome enrichment at mid-nucleoid.
677
678 **E. coli *is an asymmetric organism.***
679 The spatial macromolecular asymmetries uncovered in our study contrast with the common perception of
680 *E. coli* as a symmetric organism. In our relatively rich growth medium (M9gluCAAT), the distribution of
681 polysomes at the new pole in newborn cells was, on average, higher than at the old pole through inheritance
682 of the large mid-cell accumulation of polysomes from their mother cells (Figure 3A and D). We also
683 observed an asymmetric distribution in DNA density within nucleoids, which correlated with the availability
684 of polysome-free space along the cell length and width (Figure 3E-G). This asymmetry emerged before cell
685 division (Figure 3D and Movie S2). Simulations of our reaction-diffusion model suggest that slower
686 diffusing/relaxing nucleoids are more likely to reproduce these nucleoid position and compaction
687 asymmetries during the finite course of the cell division cycle (Figure 4E). A reduction in the apparent
688 nucleoid diffusivity has been linked to nucleoid-associated proteins, which bridge and thus stiffen the DNA
689 polymer (Subramanian and Murray, 2023). The physiological significance for these dynamic cellular
690 asymmetries is not clear at this time, though it is conceivable that a difference in DNA compaction within
691 the nucleoid may affect gene expression. Regardless, our study illustrates how spatial and temporal
692 asymmetries in the cytoplasm can emerge from the interactions between two of the most important
693 macromolecules in the cell.
694
695
696

697 **METHODS**

698

699 **Strains and constructs**

700 Strains and plasmids used for this study are listed in Tables S2 and S3, respectively, while the sequences
701 of the oligonucleotides used to make constructs can be found in Table S4.

702

703 To measure the concentration and spatial heterogeneity of ribosomes inside *E. coli*, we used strains in
704 which the RplA 50S ribosome subunit protein (strains CJW7323, CJW6768, CJW7020 and CJW7651) or
705 the RpsB 30S ribosome subunit protein (strains CJW6769 and CJW7021) are fused with mEos2 (strains
706 CJW6768 and CJW6769), msfGFP (strains CJW7020, CJW7021, CJW7651, and CJW7798) or GFP
707 (CJW7323) (Gray et al., 2019; Xiang et al., 2021). Nucleoid characteristics were measured using strains in
708 which HupA, a nucleoid-associated protein, is fused with mCherry (strains CJW7323, CJW6723 and
709 CJW7798) (Xiang et al., 2021). Alternatively, DAPI was used to stain the DNA (strains CJW6768,
710 CJW6769, CJW7020, CJW7021, and CJW7651).

711

712 The mCherry-μNS (CJW7651) particles were chromosomally expressed from the native Lac promoter after
713 induction with 150 μM IPTG (for 3 h for agarose pad experiments, or continuously for microfluidics
714 experiments). Strain CJW7651 was constructed as follows. The *gfp* coding sequence in the pER12
715 (pBAD322A-gfp-μNS) plasmid (kind gift from Dr. A. Janakiraman, City College of New York) was swapped
716 with the mCherry-coding sequence using megaprimer whole plasmid (MEGAWHOP) cloning (Bryksin and
717 Matsumura, 2010) and the primer pair ER12-MCR-fwd/ER12-MCR-rev2 to generate plasmid pER12-
718 mCherry. The mCherry-μNS coding sequence and the *rrnB* transcriptional terminator were amplified from
719 the pER12-mCherry plasmid (primer pair μNSmCherry fwd/rev) and assembled with the *frt* site flanked with
720 a kanamycin resistance cassette (amplified from pKD13 (Datsenko and Wanner, 2000) using the primer
721 pair FRT_KanR fwd/rev) and the ColE1 origin of replication (PCR amplified from the pBAD22A plasmid
722 (Guzman et al., 1995) using the primer pair ColE1 fwd/rev) using Gibson DNA assembly (Gibson et al.,
723 2009) to form the pAPG1 plasmid. The pAPG1 plasmid also included two 50 bp sites homologous to the
724 *attB* region of the *E. coli* chromosome, introduced as overhangs in the primers used for Gibson DNA
725 assembly. The *attB* homologous regions allowed for the integration of the arabinose inducible mCherry-
726 μNS expression cassette into the respective site, though this was not used in this study. The pAPG1
727 plasmid was verified by sequencing using the pAPG1 seq1-5 primers. The mCherry-μNS coding sequence
728 was then PCR amplified from the pAPG1 plasmid using primer pair lacZYA_redμNS fwd/rev, which includes
729 50-bp overhangs homologous to the region upstream and downstream of the *lacZYA* operon, and
730 integrated downstream of the *lac* promoter in the MG1655 strain (Guyer et al., 1981; Jensen, 1993) using
731 lambda red recombination and the pKD46 plasmid (Datsenko and Wanner, 2000) for the construction of
732 the CJW7144 strain. Correct insertion of the mCherry-μNS coding sequence to substitute the *lacZYA*
733 operon coding sequences was confirmed by colony PCR using primer pairs LacI_fwd/CynX_rev and
734 LacI_fwd/mCherry_rev. Transduction with a P1 phage lysate of the CJW7144 strain was used to transfer

735 the mCherry-μNS expression cassette into the CJW7020 strain using kanamycin as a selection marker. As
736 a result, the CJW7145 strain was constructed, which was verified using colony PCR and the primer pairs
737 LacI_fwd/CynX_rev and LacI_fwd/mCherry_rev, KanR_fwd/CynX_rev. The CJW7145 strain was then
738 transformed using the pCP20 plasmid (Datsenko and Wanner, 2000), which encodes the FLP recombinase
739 (Cherepanov and Wackernagel, 1995) to remove the kanamycin resistance cassette, yielding the CJW7651
740 strain.
741
742 The CJW7798 strain was derived from the MG1655 (DE3) strain (Tseng et al., 2010a), which carries the
743 T7 RNA polymerase-encoding gene under *lacUV5* control. Transduction with a P1 phage lysate of the
744 CJW5158 strain (Gray et al., 2019) was used to transfer the gene encoding the HupA-mCherry fusion into
745 the MG1655 (DE3) strain using kanamycin as a selection marker. The pCP20 plasmid (Datsenko and
746 Wanner, 2000), which encodes the FLP recombinase (Cherepanov and Wackernagel, 1995), was used to
747 remove the kanamycin resistance cassette, yielding the CJW7466 strain. Transduction with a P1 phage
748 lysate of the CJW7019 strain, a kanamycin-resistant intermediate of strain CJW7020 (Gray et al., 2019),
749 was used to transfer the gene encoding the RplA-msfGFP fusion into the CJW7466 strain using kanamycin
750 as a selection marker. The resulting strain (CJW7766) was grown in the presence of kanamycin since the
751 cells tend to lose msfGFP fluorescence in the absence of the antibiotic. The sequence of the CJW7766
752 strain was confirmed by whole genome sequencing.
753
754 The pET28:mTagBFP2 plasmid variant was derived from the pET28:GFP plasmid (Shis and Bennett,
755 2013), which was a gift from Mathew Bennett (Addgene plasmid # 60733 ; http://n2t.net/addgene:60733;
756 RRID:Addgene_60733). First, the GFP coding sequence was substituted with the mTagBFP2 coding
757 sequence from the pBAD-mTagBFP2 plasmid (Subach et al., 2011), a gift from Vladislav Verkhusha
758 (plasmid # 34632; http://n2t.net/addgene:34632; RRID:Addgene_34632). Specifically, the mTagBFP2
759 coding sequence was amplified using the primer pair mTagBFP2 fwd/rev and assembled (Gibson DNA
760 assembly) with the pET28 backbone, which was amplified in two pieces using the pET28_one fwd/rev and
761 the pET28_two fwd/rev primer pairs to derive the pET28:mTagBFP2 plasmid. Then, the kanamycin
762 resistance cassette that was originally present in the pET28 backbone was substituted with the
763 chloramphenicol resistance cassette from the pSB3C5-proA-B0032-E0051 plasmid (Davis et al., 2011)
764 which was a gift from Joseph Davis and Robert Sauer (Addgene plasmid # 107244;
765 http://n2t.net/addgene:107244; RRID:Addgene_107244). Specifically, the backbone of the
766 pET28:mTagBFP2 plasmid excluding the kanamycin resistance cassette was amplified using the
767 pET28mTagBFP2 fwd/rev primers and assembled (Gibson DNA assembly) with the coding sequence of
768 the chloramphenicol resistance cassette that was amplified using the cmR fwd/rev primer pair. As a result,
769 the pET28:mTagBFP2-CmR plasmid was created. The proper assembly of the pET28:mTagBFP2 and
770 pET28:mTagBFP2-CmR plasmids were confirmed by sequencing.
771

772 The pET28:mTagBFP2-CmR plasmid was introduced into CJW7766 by electroporation to create the
773 CJW7798 strain, which was used to redirect the ribosomes away from the nucleoid onto the plasmid-
774 expressed mTagBFP2 mRNAs after inducing the expression of T7 RNA polymerase with IPTG.
775
776 **Growth conditions**
777 Strains CJW6769, CJW7020 and CJW7021 used in Figure 2 and Figure 2 – figure supplement 1 were
778 grown as previously described (Gray et al., 2019) using a basic M9 medium formulation without trace
779 elements and supplemented with 0.2% (w/v) carbon source and when specified with 0.1% (w/v) casamino
780 acids (CAA) and 1 µg/mL thiamine (T). The strain CJW6768 (used in Figure 2 and and Figure 2 – figure
781 supplement 1) was grown using the same medium formulation. The abbreviations of the medium growth
782 conditions presented in Figure 2A and Figure 2 – figure supplement 1 are defined in Table S1. For the rest
783 of our experiments on agarose pads or in a microfluidic device, strains CJW7323, CJW7651 and 7798 were
784 grown in M9 salts (final concentrations: 33.7 mM Na_2HPO_4, 22 mM KH_2PO_4, 8.55 mM NaCl, 9.35 mM
785 NH_4Cl, 1 mM $MgSO_4$, 0.3 mM $CaCl_2$) supplemented with trace elements (Fe, Zn, Cu, Co, B, Mn), 0.1%
786 (w/v) thiamine, and, when specified, 0.4% (w/v) casamino acids. The pH of the 10x M9 salts was adjusted
787 to 7.2 with NaOH. The trace elements were added at a final concentration of 13.4 mM ethylene-diamine-
788 tetra-acetic-acid, 3.1 mM of $FeCl_3$-$6H_2O$, 0.62 mM of $ZnCl_2$, 76 µM of $CuCl_2$-$2H_2O$, 42 µM of $CoCl_2$-$2H_2O$,
789 162 µM of HBO_3-$2H_2O$, 8.1 µM of $MnCl_2$-$4H_2O$.
790
791 To achieve steady-state exponential growth prior to imaging, a stationary phase liquid culture in the
792 appropriate growth medium was diluted at least 10,000 times and grown to an optical density at 600 nm
793 (OD_{600}) between 0.1 and 0.3. These cells were either loaded in a mother-machine-type microfluidics device
794 (Lin and Jacobs-Wagner, 2022; Wang et al., 2010) where they were grown under the constant flow of
795 medium (~0.5 µL/sec), or spotted on 1% agarose pads prepared with the same growth medium. In the
796 microfluidic device, cells were grown for at least 3 h prior to image acquisition. All precultures and
797 experiments were performed at 30ºC.
798
799 The mCherry-µNS particles (CJW7651 strain) were imaged on agarose pads after inducing exponentially
800 growing cells with 150 µM IPTG for 3 h (Figure 4E-G). Before spotting on the 1% agarose pad, the induced
801 cells were stained with DAPI (1 µg/mL) for 5 min. In both experiments, the cells were growing in
802 M9gluCAAT.
803
804 To redirect ribosomes to plasmid-expressed, T7 promoter-driven mTagBFP2 mRNAs, exponentially
805 growing CJW7798 cells grown in M9glyCAAT to an OD ~ 0.2 were spotted on a 1% agarose pad containing
806 M9glyCAAT and 100 µM IPTG, the latter to induce the expression of the T7 RNA polymerase.
807
808
809

810 **Rifampicin treatment**
811 The antibiotic rifampicin (see Table S5) was used to block transcription, deplete mRNAs, and release the
812 mRNA-bound ribosomes (polysomes). Rifampicin treatment was performed either in batch culture (Figure
813 1 – figure supplement 2) or in microfluidics (Figure 6 and Movie S4).
814
815 For the microfluidic experiment, two rounds of rifampicin treatment were performed by switching between
816 M9gluCAAT containing antibiotic (100µg/mL) and antibiotic-free medium at 30ºC. For the medium switches,
817 solenoid valves were used in a custom-built pressurized perfusion system, achieving fast (within 1 min)
818 changes in the cellular environment. The first switch to rifampicin occurred 2 h after normal growth in
819 antibiotic-free medium (Figure 6A and Movie S4). Rifampicin treatment lasted 2 h until the system switched
820 back to antibiotic-free medium, where cells were left to recover for 8 h. Twelve hours into the experiment,
821 the system switched again to rifampicin-containing medium.
822
823 **A22 and cephalexin treatment**
824 Cephalexin (50 µg/mL) and A22 (4 µg/mL) (see Table S5) were added to exponentially growing CJW7323
825 cell cultures (OD_{600} ~ 0.1) in M9gluCAAT just prior to spotting on a 1% agarose pad, which was made with
826 the same growth medium and contained the same antibiotic concentrations. The radial expansion of the
827 cells and the polysome and nucleoid signals were tracked over time in a time-lapse experiment. The
828 selected concentration of A22 has previously been shown to not affect cell growth (Takacs et al., 2010). All
829 precultures and time-lapse imaging experiments were performed at 30ºC.
830
831 **Chloramphenicol and cephalexin treatment**
832 Exponentially growing CJW7323 cells (OD_{600} ~ 0.1) in M9gluCAAT were pre-treated with cephalexin (50
833 µg/mL) for 1 h in the shaking flask. Then the cells were spotted on a 1% agarose pad, which was made
834 with the same growth medium and contained cephalexin (50 µg/mL) and chloramphenicol (75 µg/mL). All
835 precultures and time-lapse imaging experiments were performed at 30ºC.
836
837 **Ectopic polysome accumulation experiment**
838 Exponentially growing CJW7798 cells in M9glyCAAT supplemented with kanamycin (50 µg/mL) and
839 chloramphenicol (35 µg/mL) were washed one time with M9glyCAAT minimal medium lacking antibiotics
840 but supplemented with 100 µM IPTG (see Table S5). The washed cells were spotted on a 1% agarose pad
841 prepared with M9glyCAAT also supplemented with IPTG (100 µM) for time-lapse imaging. All pre-cultures
842 and time-lapse imaging experiments were performed at 30ºC. Since chloramphenicol affects protein
843 synthesis and thus polysome formation, the agarose pads lacked chloramphenicol, resulting in a fraction
844 that loss the plasmids based on the absence of blue fluorescence. Therefore, only cells that expressed blue
845 fluorescence (and thus carried the pET28:mTagBFP2-CmR plasmid) were analyzed.
846

847 **DNA quantification using flow cytometry**

848 Exponentially growing CJW7798 cells (OD_{600} ~1) in M9glyCAAT supplemented with kanamycin (50 µg/mL)
849 and chloramphenicol (35 µg/mL) were washed with M9glyCAAT minimal medium lacking antibiotics. The
850 washed cells were used to start two cultures in M9glyCAAT without antibiotics. In one culture, the
851 expression of the mTagBFP2 was induced with 100 µM ITPG. In the second culture, the cells were not
852 supplemented with IPTG (i.e., no induction). After 200 min, the cells were fixed with 70% cold ethanol for
853 30 min, followed with stained with 5µM DRAQ5 (Invitrogen™ eBioscience™ Cat. 65-0880-92) for 30 min at
854 37ºC as previously described (Silva et al., 2010). The stained cells were washed with 0.1 Tris, 2mM $MgCl_2$
855 buffer (pH 7.4) and then used for flow cytometry. The Attune™ CytPix flow cytometer (Invitrogen™) was
856 used to quantify the DRAQ5 fluorescence in the red laser 2 (RL2) channel (637 nm excitation, 690DLP
857 beamsplitter, 720/30 emission, 440 voltage) and the cell size in the side scatter (SSC) channel (320
858 voltage). A low threshold of $0.1x10^3$ was set for the forward scatter and $0.3x10^3$ for the side scatter signal.
859 The flow was set at 12.5 µL/min for a total of 10^5 counted events per sample. The stained cells were diluted
860 appropriately (usually 100-fold) to ensure less than 10^3 events per second. For each biological replicate,
861 the DNA content (RL2-Area) and the cell size (SSC-Area) were quantified. Lower thresholds in the RL2-
862 Area and the SSC-Area channels were applied to exclude very small events without fluorescence, as well
863 as a polygon gate in the SSC-Area vs. SSC-Height statistics to exclude events with more than one cells.
864 These gates were first applied on the data from the uninduced sample and then replicated on the data from
865 the induced sample for each biological replicate. As a result, the exact same thresholds were applied
866 between the induced and uninduced samples per biological replicate for fair comparison. The analysis of
867 the flow cytometry data was performed using a custom Python package (*flowio_to_pandas*), which is based
868 on the FlowIO flow cytometry standard (FCS) file parser (White et al., 2021) and which allows for interactive
869 gating.

870

871 **Microscopy**

872 Strains CJW6769, CJW7020, and CJW7021 used in Figure 2A-B and Figure 2 – figure supplement 1, were
873 imaged on agarose pads using the same microscopy set-up and optical configurations as previously
874 described (Gray et al., 2019). Snapshots of the CJW6768 strain (used in Figure 2 and Figure 2 – figure
875 supplement 1) were taken using a Nikon Ti-E microscope equipped with a 100x Plan Apo 1.45NA Ph3 oil
876 objective, a Hamamatsu Orca-Flash4.0 V2 CMOS camera (16-bit, Slow Scan sensor mode) and a
877 Lumencor Spectra X LED (Light Emitting Diode) engine. The 395/25nm LED was used to excite DAPI and
878 the 470/24nm LED was used to excite GFP. DAPI fluorescence was acquired using an ET350/50x
879 (excitation filter), RT400lp (dichroic mirror), ET460/50m (emission filter) filter cube from Chroma. The
880 ET470/40x (excitation filter), T495lpxr (dichroic mirror), ET525/50m (emission filter) configuration from
881 Chroma was used for GFP fluorescence acquisition. The microscope was controlled using the NIS
882 Elements software by Nikon and the ND acquisition module.

883

884 For the time-lapse observation of cells (strain CJW7323) treated with chloramphenicol, A22 and/or
885 cephalexin, images were taken using a Nikon Ti-E microscope, equipped with a 100x Plan Apo 1.45NA
886 Ph3 oil objective, a Hamamatsu Orca-Flash4.0 V2 CMOS camera (16-bit, Slow Scan sensor mode), and a
887 Sola solid state white light source (Lumencor), in a temperature-controlled enclosure (Okolabs). The
888 AT470/40x excitation filter, combined with a T495LPXR beam-splitter and an ET525/50m emission filter,
889 was used for GFP. For mCherry visualization, the ET560/40x excitation filter, combined with a T585lp
890 beam-splitter and a ET630/75m emission filter, was used. A neutral density filter (32x) was applied in the
891 excitation path to reduce phototoxicity and photobleaching. Images were taken every 2.5 min in the
892 brightfield channel (phase contrast) and every 5 min in the fluorescence channels (RplA-GFP and HupA-
893 mCherry).
894
895 For the rest of the brightfield and epi-fluorescence wide-field microscopy experiments (strains CJW7323,
896 CJW7651, and CJW7798), snapshots or time-lapse images were taken using a Nikon Ti2-E inverted
897 microscope, equipped with a 100x Plan Apo 1.45NA Ph3 oil objective, a Photometrics Prime BSI back-
898 illuminated sCMOS camera (2048x2048 pixels sensor with a pixel size of 6.5 μm), and a Lumencor Spectra
899 III LED (Light Emitting Diode) engine, in a temperature-controlled enclosure (Okolabs). The HDR 16-bit
900 sensor mode was used to acquire images. The microscope was controlled using the NIS Elements software
901 by Nikon, and the JOBS or the ND acquisition module were used to acquire snapshots or time-lapse
902 images. The Perfect Focus System (by Nikon) was used to maintain focus in microfluidics experiments.
903 The auto-focus function in NIS Elements was used to locate the optimal z-position in agarose pad
904 experiments (snapshots or time-lapse). For the DAPI, BFP, GFP, or mCherry channels, a polychroic mirror
905 (FF-409/493/596-Di02 by Shemrock) combined with a triple-pass emitter (FF-1-432/523/702-25 by
906 Shemrock) was used. For DAPI, BFP, and GFP imaging, additional emission filters were applied in the
907 optical path (FF01-432-36 by Shemrock, FF01-432-36 by Shemrock and ET525/50M by Chroma,
908 respectively). DAPI, BFP, GFP, and mCherry were excited using a 390/22nm, 390/22nm, 475/28nm and
909 575/25nm LED, respectively.
910
911 For the microfluidic experiments (strain CJW7323), the excitation light intensity was reduced to 20% for the
912 1-min interval and 30% for the 3-min interval imaging of the RplA-GFP and HupA-mCherry. An exposure
913 time of 120-ms was used for both markers. In all time-lapse experiments, a neutral density filter (absorptive
914 ND filter, OD:1.3 / 5% transmission, NE13B by Thorlabs) was also applied to reduce the LED power and
915 minimize phototoxicity and photobleaching. The LED powers (factored by the neutral density filters) were
916 calibrated using a microscope slide power meter with an 18x18 mm sensor size (S170C by Thorlabs). The
917 light intensity was measured for each excitation wavelength (475/28nm and 575/25nm) at the end of the
918 objective (without immersion oil) for different LED intensities (% of maximum intensity). From the generated
919 calibration curves, the RplA-GFP excitation light power was estimated to be 524 μW and 629 μW for the 1-

920 min and 3-min fluorescence interval imaging, respectively. HupA-mCherry was excited with 109 μW light
921 power for the 1-min and 191 μW for the 3-min fluorescence interval imaging.
922
923 The type N immersion oil (by Nikon) was used in all experiments except for the time-lapse observation of
924 cephalexin, A22, A22+cephalexin, and chloramphenicol- and cephalexin-treated cells where the type F
925 immersion oil (by Nikon) was used. All imaging (time-lapse and snapshots) was done at 30ºC.
926
927 **Analysis software and code availability**
928 Cropping and alignment of the microfluidic channels were performed with MATLAB (www.mathworks.com)
929 using a previously published pipeline from our lab (Lin and Jacobs-Wagner, 2022). Supervised classification
930 and curation of the Oufti cell meshes was also implemented in MATLAB (Campos et al., 2018; Govers et
931 al., 2024; Gray et al., 2019). For the T7 experiments, segmentation and tracking of the CJW7798 cells was
932 performed using the Omnipose deep neural network architecture (Cutler et al., 2022), using a previously
933 trained model (Thappeta et al., 2024) and the SuperSegger MATLAB-based package (Stylianidou et al.,
934 2016). The remaining analyses were performed using Python 3.9 (www.python.org), that included the
935 *numpy* (Harris et al., 2020), *scipy* (Virtanen et al., 2020), *pandas* (McKinney, 2010), *scikit-mage* (Van Der
936 Walt et al., 2014), *scikit-learn* (Pedregosa et al., 2012), *shapely* (Gillies, Sean et al., 2023), *statsmodels*
937 (Seabold and Perktold, 2010) and *pytorch* (Paszke et al., 2019) libraries. The *matplotlib* (Hunter, 2007) and
938 *seaborn* (Waskom, 2021) libraries were used for plotting. The analysis pipeline and functions (summarized
939 in Table S6) are available in the Jacobs-Wagner lab GitHub repository
940 (http://www.github.com/JacobsWagnerLab/published/tree/master/Papagiannakis_2025) and the GitHub
941 repository of Alexandros Papagiannakis (https://github.com/alexSysBio).
942
943 **Cell segmentation and tracking**
944 For the CJW6768, CJW6769, CJW7020, and CJW7021 strains used in Figure 2 and Figure 2 – figure
945 supplement 1, Oufti (Paintdakhi et al., 2016) was used to draw cell meshes on the phase contrast snapshots
946 and a MATLAB-based support vector machine model was used to remove the badly segmented cells as
947 previously described (Campos et al., 2018; Govers et al., 2024; Gray et al., 2019).
948
949 The Omnipose deep neural network architecture (Cutler et al., 2022) with a previously trained model
950 (Thappeta et al., 2024) was used to segment the CJW7798 cells during T7 RNA polymerase induction on
951 an agarose pad. The segmented cells were then tracked using SuperSegger (Stylianidou et al., 2016). A
952 custom class (*omnipose_to_python_ghv.py*) was developed to transfer the SuperSegger segmentation and
953 tracking data into Python for post-processing.
954
955 Due to the unusual and variable morphology of the A22/cephalexin-treated cells, a custom Python class
956 was developed for their segmentation and tracking. The *Otsu_phase_segmentation_ghv.py* class

segments the cells by applying an Otsu-threshold (Otsu, 1979) on the inverted phase images, followed by binary dilation (*scikit-image.morphology.binary_dilation* Python function) hole filling (*scipy.ndimage.binary_fill_holes* Python function), and binary closing (*scikit-image.morphology.binary_closing Python function*). The segmentation masks were tracked between subsequent timepoints, using cell distance as well as cell area constraints, and linked into cell growth trajectories. Cell morphology criteria such as the maximum pixel distance from the medial axis and the medial axis sinuosity were used to remove bad segmentations. The remaining segmentation masks were manually curated.

For the other experiments on agarose pads, a neural network (Wiktor et al., 2021; Zhou et al., 2020) with a previously designed and trained U-net architecture (Mäkelä et al., 2024) was used to segment single cells based on phase contrast snapshots. The generated segmentation masks were further processed by watershed separation, filling the holes within masks and removing unusually small masks. Finally, a graphical interface was used to manually remove the badly curated cells (less than 5% of the segmented cell population).

In contrast to the Oufti software (Paintdakhi et al., 2016) that generated sub-pixel meshes around the cell boundaries, the other applied segmentation algorithms returned pixel-based cell masks. To deal with this discrepancy, the sub-pixel cell meshes from Oufti were converted into pixel-based cell masks by collecting the pixels within the circumscribed single cell area in Python (*oufti_snapshots_GrayGovers* class, included in the *snapshots_analysis_OUFTI_GrayGovers* Python script). After this conversion, the same Phyton-based functions were applied for the analysis of the cell fluorescence and morphology statistics regardless of the segmentation method used.

To segment cells growing in the microfluidic device, a custom library of image analysis functions (*mother_machine_segmentation* class, included in the *microfluidics_segmentation_ghv* Python script) was developed in Python. This algorithm was applied on the cropped, aligned, background-subtracted, and inverted phase contrast images that were produced using a previously published pipeline (Lin and Jacobs-Wagner, 2022) in MATLAB. Cell segmentation was performed in three steps. First, all the cells within the microfluidics channel, which were brighter than the microfluidic channel background in the inverted and background-corrected phase-contrast channel, were segmented using an Otsu intensity threshold (Otsu, 1979). This crude thresholding step, which separated the cell (brighter: 1) from the background (darker: 0) pixels, yielded at least one masked label for the entire row of stacked cells in each microfluidic channel. A watershed segmentation was then applied to define the boundaries between individual cells and split the Otsu-based binary mask(s). The watershed algorithm was guided by the number of cells and their relative positions in the microfluidic channel, which were determined using an adaptive filter combined with the local

993 decrease of the inverted phase intensity between the poles of adjacent cells. Finally, a graphical interface
994 was used to curate the cell masks by manually splitting or merging cell labels.
995
996 After segmentation, the curated single-cell masks were tracked over time and linked into trajectories from
997 birth to division using the centroid distance and the relative area difference between cells at consecutive
998 time-points (*mother_machine_tracking* class, included in the *microfluidics_segmentation_ghv* Python
999 script, or the *fluorescence_analysis* class and its depending functions in the *Time_lapse_on_agarose_pads*
1000 Python package). Examples of cell segmentation and tracking in microfluidics are shown in Movie S1 and
1001 Figure 1 – figure supplement 1A. Regardless of the image acquisition time intervals for the fluorescence
1002 channels, phase-contrast images were acquired every minute, which allowed for accurate cell tracking.
1003
1004 Fluorescence background correction was different between microfluidic and agarose-pad experiments. In
1005 microfluidics, the average background was measured within two 8-pixel (0.528 μm) wide areas, one on the
1006 left side and one the right side of the channel, at least 10 pixels (0.66 μm) away from the channel boundaries
1007 from top to bottom. The estimated background was then subtracted along the channel length. The
1008 background correction was integrated in the *get_fluorescence_image* function, located in the
1009 *microfluidics_analysis_functions*_ghv Python script.
1010
1011 In agarose-pad experiments, an Otsu threshold (Otsu, 1979) was used on the inverted phase-contrast
1012 image to segment all cells. A binary dilation was then performed on these crude cell masks before
1013 estimating the local average fluorescence of the unmasked pixels (pixels outside the dilated cell masks).
1014 The locally-averaged background was then used to fill in the cell areas and reconstruct the background of
1015 the entire field of view in the absence of cells. The smoothed (Gaussian smoothing) reconstructed
1016 background fluorescence was subtracted from each fluorescence image. This background correction
1017 pipeline (*back_sub* function) is integrated in both the *unet_snapshots* class and the
1018 *oufti_snapshots_GoversGray* class. For the time-lapse imaging of A22-treated CJW7323 cells (Figure 7)
1019 and CJW7798 cells during induction of T7 RNA polymerase expression (Figure 6), the fluorescence
1020 background was not subtracted since we did not need to quantify the raw pixel values. The normalized
1021 polysome and nucleoid fluorescence normalized by the average whole cell fluorescence is shown instead,
1022 marking the relative macromolecular rearrangements.
1023
1024 **mCherry-μNS particle localization and tracking**
1025 For the localization of the diffraction-limited mCherry-μNS particles (Figure 5), a set of custom functions
1026 were developed in Python and implemented in the *particle_positions_snapshots* class, included in the
1027 *snapshots_analysis_UNET_ghv* Python script.
1028

The fluorescent particles were segmented in the background corrected mCherry-μNS fluorescence images using a Laplace of Gaussian (LoG) and an adaptive filter combined. The particle masks that had an area larger than a specified threshold (80 pixels for the microfluidics and 90 pixels for the agarose-pad experiments), which usually included two particles from the same or adjacent cells, were further processed by applying a relative fluorescence threshold (90th percentile of masked pixel intensity) to find the local fluorescence maxima and separate the two objects. Additional minimum area and aspect ratio constraints were applied. To accurately estimate the particle position with sub-pixel resolution, a 2D Gaussian function (eq. 1) with rotation (eq. 2) was fitted (least square method: *scipy.optimize.leastsq*) to an area of 7x7 pixels centered at the centroid of the particle mask:

$$g(x,y) = A\exp\left(-\frac{1}{2}\left(\left(\frac{x_0-x_{rot}}{\sigma_x}\right)^2 + \left(\frac{y_0-y_{rot}}{\sigma_y}\right)^2\right)\right) \quad \text{[eq. 1]}$$

and

$$\begin{aligned} x_{rot} &= x\cos(\theta) - y\sin(\theta) \\ y_{rot} &= x\sin(\theta) + y\cos(\theta) \end{aligned} \quad \text{[eq. 2]}$$

where x and y are the coordinates in the 2D imaging plane, A is the amplitude of the fitted Gaussian, σ is the standard deviation in each dimension, and θ is the rotation angle in radians, which was used to rotate the Gaussian distribution (x_{rot}, y_{rot}) around the particle center or the Gaussian mean (x_0, y_0).

Two-dimensional cell mapping and alignment

Ribosome and nucleoid fluorescence statistics, as well as particle positions within cells, were mapped in relative 2D cellular coordinates from pole to pole and across the cell width. Such mapping allowed us to project the fluorescence or position statistics in 1 or 2D for specific cell length ranges and cell division cycle intervals. For this analysis, it was necessary to draw the medial axis for each of the segmented cells, which was obtained differently in microfluidic and agarose-pad images.

In the microfluidic experiments, where all the cells were stacked in a vertically oriented channel, the medial axis was drawn by fitting a second-degree polynomial to the most distant coordinates from the cell boundaries, excluding the cell caps at the poles where the medial axis was linearly extrapolated. The length of the cells, which was parallel to the length of the microfluidic channel, was used as the independent variable for the fitting. This medial axis estimation is implemented via the *all_medial_axis* function in the *microfluidics_analysis_functions_ghv* Python script.

However, in the agarose-pad experiments, cells were randomly oriented in the imaging plane. Thus, it was impossible to use one of the coordinates (x or y) as the independent variable as this would bias our medial axis estimation toward the same coordinate for cells that were not diagonally oriented. Instead, we developed an algorithm that scanned through the middle of the cells with a fixed sub-pixel step and directionality constraints to identify nodes at the most distant locations from the cell boundaries. These

ordered (from pole to pole) and numbered nodes were used to fit the x and y coordinates of the medial axis separately, using the number of the node as an independent variable and its position coordinates as dependent variables. The degree of the fitted polynomials (*d*) scaled linearly with the total number of nodes (*N*) based on the relation $d = 0.1N - 5$. Similar to the microfluidic experiments, the medial axis was linearly extrapolated at the cell caps. This medial axis estimation is implemented using the *get_medial_axis* function in both the *unet_snapshots* and *oufti_snapshots_GoversGray* classes located in the *snapshots_analysis_UNET_ghv* and *snapshots_analysis_OUFTI_GrayGovers_ghv* Python scripts respectively. The medial axis estimation function is also provided as a separate function in the *Bivariate_medial_axis_estimation.py* Python script.

The medial axis of each cell, with a resolution of 0.1 pixel, was used to map the cell pixels and particle positions along the cell length and width. The projection of each pixel or particle position on the medial axis, defined as the most proximal node on the central line, was used to determine its cell length coordinate. The distance between the pixel or particle position and its medial axis projection was used to determine its absolute cell width coordinate. The sign of the cross product $\overrightarrow{PL} \times \overrightarrow{PC}$ (plus or minus), where *L* was the location of the particle, *P* was its projection on the medial axis, and *C* was the center of mass of the cell mask, was used to determine the position of particles or cell pixels on the sagittal plane.

Cell polarity and ages

In time-lapse experiments, the old and new poles of the cells were determined as follows. The pole of the daughter cell that was closer to the mid-cell position of its predivisional mother cell, where cell constriction occurs, was defined as the new pole. The medial axis coordinates were adjusted based on this polarity. As a result, the relative cell length extended from -1 to 1, with -1 corresponding to the old pole, 1 to the new pole, and zero to the cell center (see Figure 3 – figure supplement 1B-D). The implementation of this method is included in the *get_polarity* function in the *microfluidics_analysis_functions_ghv* Python script.

Cell lineages and ages relative to the oldest mother cells (first lineage) at the closed end of the microfluidic channel were determined using the orientation of the cell poles. The daughter cells that had the same polarity as the oldest mother cells were assigned the same age and lineage as their mothers. The daughter cells with the opposite polarity, which inherited the new pole of their mother cells, were considered younger and belonged to the second lineage. The daughter cells of mother cells belonging to the second lineage were classified as lineages three and four depending on their polarity. Cells from the third lineage had opposite polarity and those from the fourth lineage had the same polarity as their second lineage mother cells. Finally, mother cells from the third lineage, which inherited the new pole of their second-lineage mother cells, divided to yield the fifth and sixth cell lineages. The fifth lineage had the same polarity as its third-lineage mother and its sister lineage (sixth) had the opposite polarity and inherited the new pole from its third-lineage mother cell. The implementation of this method is included in the *get_ages* function in the

1104 *microfluidics_analysis_functions*_ghv Python script. For the analysis of the data presented in Figure 3, only
1105 the third, fourth, fifth and sixth lineages were considered to avoid age-related effects at the cell poles (Chao
1106 et al., 2024; Coquel et al., 2013; Koleva and Hellweger, 2015; Łapińska et al., 2019; Lindner et al., 2008;
1107 Proenca et al., 2019).
1108
1109 **Construction of intensity profiles, 2D cell projections, demographs, and kymographs**
1110 With the ribosome and nucleoid fluorescence pixels as well as the μNS particle positions inside the cells
1111 having been mapped, the fluorescence and particle statistics from pole to pole (medial axis projection) and
1112 across the cell width (distance from the medial axis) were plotted for different cell division cycle intervals or
1113 cell length ranges.
1114
1115 An intensity profile represents the change in a fluorescence statistic along the cell from one pole to the
1116 other. Such a fluorescence statistic can be the average fluorescence intensity (as in Figures 1D, 3G, 5C,
1117 and Figure 3- figure supplement 1B), which corresponds to the concentration of the reported protein per
1118 cell area (sum of pixels divided by the number of pixels). In other analysis (as in Figure 6C and Figure 1 –
1119 figure supplement 6C), the protein concentration along the cell length was divided by the whole cell
1120 average. This scaled statistic is expressed as a percentage change relative to average concentration (mean
1121 %). A value above 100 indicates increase above the average, whereas a value below 100 corresponds to
1122 a decrease below the average concentration. This scaled statistic is insensitive to the RplA and HupA
1123 concentration variability between cells, or to the maturation of the GFP or mCherry fluorophores. As a result,
1124 the scaled concentrations showcase rearrangements of the tagged proteins and do not imply changes in
1125 protein synthesis relative to cell growth.
1126
1127 Intensity profiles were plotted for single cells (Figure 3 – figure supplement 1B and Figure 1 – figure
1128 supplement 6A) or populations (as in Figures 1D, 3G, 5C, 6C, 6E). In the second instance, the intensity
1129 profiles represent the average 1D projection of the fluorescence statistic for a specific cell division cycle
1130 interval, cell length range, growth rate range, polysome and nucleoid asymmetry group, or time range (e.g.,
1131 during antibiotic treatment). To generate a single-cell intensity profile, the medial axis length and its
1132 projected pixels were binned, and the average value of the selected fluorescence statistic was calculated
1133 per bin. If the number of bins was higher than the length of the medial axis in pixels, the missing values
1134 were filled in by linear interpolation. To avoid artefacts from the cell boundaries, the intensity profile was
1135 estimated for a box with a width of six pixels (~0.4 μm) centered on the medial axis (i.e., three pixels on
1136 each side of the medial axis). The intensity profile was occasionally smoothed by a moving average of a
1137 specified cell-length window, without excluding the bins at the edges which were not smoothed.
1138 Alternatively, a univariate spline (*scipy.interpolate.UnivariateSpline*) was fitted to the cell-length-binned data
1139 (as in Figure 5C). The univariate splines were fitted to the binned fluorescence intensity along the cell
1140 length. The number of cell length bins (N_{bin}) linearly scaled with the cell length in μm (l_{cell}) using the first-

order relationship: $N_{bin} = \frac{100}{4.3}\, l_{cell}$ (only the whole part of the decimal was considered). Similar to the intensity profile where a fluorescence statistic was plotted along the cell length, the density profiles (histograms of the particle positions along the cell) for the mCherry-μNS (Figure 5C) particles along the cell were also plotted. Note that the intensity profiles shown in Figures 1D, 3G, 5C, 6C, 6E, Figure 1 – figure supplement 1D, and Figure 2 – figure supplement 3D are averages of many segmented cells or cell division cycles. In these averaged profiles, the variability in the timing of nucleoid segregation across cells attenuates the appearance of polysome accumulation. Furthermore, the point spread function of fluorescent ribosome markers causes an underestimation of the magnitude of the polysome accumulations in epi-fluorescence micrographs (Bakshi et al., 2012b).

The intensity profiles were also used to construct demographs from agarose-pad experiments (Figure 2A, Figure 2 – figure supplement 1, and Figure 1 – figure supplement 6B) where cells were sorted by cell length from the shorter newborn to the longer predivisional cells. Intensity profiles were also used to construct ensemble kymographs from microfluidic experiments where the cells were sorted by their relative position in the cell division cycle (Figure 1C and Figure 2 – figure supplement 2B) or single-cell kymographs from agarose pad time-lapse measurements (Figure 7D-F). Specifically, the average intensity profile was estimated for each cell length or cell division cycle bin, and the average intensity profiles were stacked from birth to division (left to right) oriented according to the cell polarity (top to bottom). In the ensemble kymographs, the fluorescence intensities were projected along the relative cell length (cell length %), whereas in the single-cell kymographs the length of the projection linearly scales with the cell length. A Gaussian smoothing (*skimage.filters.gaussian*) was applied to smooth the demographs and ensemble kymographs.

In addition to the intensity or density profiles for a fluorescence statistic or the density of the μNS particles along the medial axis, 2D projections of the ribosome or nucleoid signal distribution (Figures 1D, 3D, 3G, 5B, 6C, 6E, and Figure 2 – figure supplement 2A) as well as the μNS particle positions (Figure 5B) were also constructed. These 2D intensity or density maps were constructed by binning the cell pixels or particle positions not only by cell length, but also by cell width. The average fluorescence statistic or the particle density was then shown per bin, including data from many single cells within a specified cell division cycle or cell length range. A Gaussian smoothing (*skimage.filters.gaussian*) was applied to smooth the 2D projections.

Extraction of population-level statistics of polysomes and nucleoids

To quantify the correlation between polysome accumulation and nucleoid segregation at the population level (Figure 2 and Figure 2 – figure supplement 1), the average polysome accumulation at mid-cell was extracted from cell snapshot images. This statistic was obtained by averaging the scaled (divided by the whole cell average concentration) RplA-GFP and HupA-mCherry intensity profiles of all the cells in the

population. Therefore, this statistic describes the average “behavior” of the population under a specific growth condition. We reasoned that if, in a specific nutrient condition, nucleoid segregation happens earlier during the division cycle, then a higher fraction of the population will have segregated nucleoids. If so, the scaled HupA-mCherry concentration should exhibit a stronger depletion at mid-cell on average. This depletion was measured as the relative concentration difference between the HupA-mCherry peaks, which corresponded to the two lobes of the constricting nucleoid, and the trough at mid-cell, which corresponds to the point of nucleoid splitting. Similarly, the average polysome accumulation was measured as the RplA-GFP relative concentration difference between the mid-cell accumulation (peak) and the polysome depleted regions near the quarter cell positions, or at the centers of the segregating sister nucleoids (troughs). The same statistics were used to quantify the relative polysome accumulation at mid-cell and the relative nucleoid depletion in the same region between cell division cycles with different growth rates in the same nutrient condition (Figure 2 – figure supplement 2).

Nucleoid segregation cycle tracking

In this work, the nucleoid segregation cycle was defined as the period from the end of a nucleoid splitting event (i.e., when a segregating nucleoid is segmented by local thresholding (custom Python function: *LoG_adaptive_image_filter.py*) as a separate object from its sister nucleoid) until the end of the splitting of the same nucleoid object (Figure 1 – figure supplement 2D), usually after cell division but sometimes in the same cell division cycle (Figure 1 – figure supplement 2A).

To track the nucleoid objects through the nucleoid segregation cycle from the mother cells to their daughters, we used the cell polarity, i.e., based on pole identity (Figure 1 – figure supplement 4B). The nucleoids of daughter cells that had opposite polarity to their mother cells were inherited from the new pole of the mother cells (groups 1 and -1 in Figure 1 – figure supplement 4B-C). The nucleoids in the daughter cells that had the same polarity as their mother cells were inherited from the old pole of the mother cells (groups 2 and -2 in Figure 1 – figure supplement 4B-C). During a complete nucleoid segregation cycle, the nucleoid was tracked from the quarter position of the mother cell to the center of its daughter cells (Figure 1 – figure supplement 4C). This method is implemented in the *track_nucleoids* function, included in the *microfluidics_analysis_functions_ghv* Python script.

To quantify the polysome accumulation and nucleoid splitting during the nucleoid segregation cycle (Figure 1E-F), we measured the RplA-GFP and HupA-mCherry concentration within the cell length region of 2.5 pixels adjacent to the center of the tracked nucleoid object (5 pixels or 0.33 μm in total).

1214 **Quantification and segmentation of polysomes and nucleoids segmentation in cells treated with**
1215 **cephalexin or cephalexin + A22**
1216 The polysome accumulations and nucleoids objects were also segmented in A22 and cephalexin-treated
1217 cells using an adaptive filter (custom Python function: *LoG_adaptive_image_filter.py*) on the masked cell
1218 fluorescence. The number of the detected polysome accumulations or nucleoid objects corresponds to the
1219 number of the segmented labels in the RplA-GFP or HupA-mCherry channel respectively. Similarly, the
1220 average polysome accumulation or nucleoid area corresponds to the average area of all segmented labels
1221 per channel. For a fair comparison between cells treated with A22 + cephalexin and cells treated with
1222 cephalexin alone, cells were randomly sampled without substitution from 12 cell area bins between 10 and
1223 13 μm^2 (bin width = 0.25 μm^2) such that the compared populations in Figure 7F had the same cell area
1224 distributions (same number of cells per cell area bin).
1225
1226 **Quantification of the distance between fusing or non-fusing nucleoids in cephalexin- and**
1227 **chloramphenicol-treated cells**
1228 The distance between nucleoids corresponds to the cell length difference between the peaks of the
1229 longitudinal HupA-mCherry signal projection (Figure 4 – figure supplement 1A-B). To calculate these
1230 distances, the HupA-mCherry longitudinal profile was first smoothed using a fourth-roder univariate
1231 regression (*scipy.interpolate.UnivariateSpline*). The optimal smoothing factor (10^3) was determined using
1232 the L-curve method (Nasehi Tehrani et al., 2012) where the x-axis corresponds to the value of the
1233 smoothing factor and the y-axis to the variance in detected nucleoid number during cell growth. The average
1234 variance was considered across the tracked cell trajectories. The smoothing factor at the elbow of the L-
1235 curve is the optimal point between overfitting, where the noise in the HupA-mCherry signal is wrongly
1236 assigned to nucleoid objects, and underfitting, where two nucleoids in proximity may be wrongly identified
1237 as one. After smoothing, the peaks of the HupA-mCherry projection were detected using the
1238 *scipy.signal.find_peaks* function, applying a lower threshold of 125 arbitrary units. The number of the
1239 detected peaks is equal to the nucleoid number per cell, whereas the distance between the peaks is equal
1240 to the distance between the nucleoid centroids. A nucleoid fusion event is indicated by the reduction in
1241 nucleoid number between consecutive frames in a cell trajectory.
1242
1243 The tracked cell trajectories were classified into those that fuse their nucleoids and those that do not. The
1244 first class includes cell trajectories that contain a nucleoid fusion event and end with less detected nucleoids
1245 objects compared to their beginning. The second class includes cell trajectories that do not contain any
1246 nucleoid fusion event and end with an equal number or more detected nucleoids compared to their
1247 beginning. All classified trajectories start at time-point 0 min, which corresponds to the first time-point of the
1248 experiment, or the first microscopy image taken after spotting the cells on the chloramphenicol-containing
1249 agarose pad. Only trajectories with more than one nucleoid at timepoint 0 min are considered. This first
1250 time-point also corresponds to when the minimum distance between adjacent nucleoids is quantified for

each cell trajectory (plotted in Figure 4 – figure supplement 1C). The nucleoid segregation variability shown in Figure 4 – figure supplement 1B, is consistent with previous observations (Spahn et al., 2014).

Linear mixed-effects models to determine the relative contribution of polysome accumulation and cell elongation to the migration of the sister nucleoids

To estimate the relative contribution of the polysome accumulation at mid-cell and that of cell elongation to the migration of the separated sister nucleoids (first seen in Figure 1H), linear mixed-effects regressions were fitted to the scaled single cell data shown in Figure 1 – figure supplement 5B (*statsmodel* package in Python, *statsmodels.formula.api.mixedlm* function). One model was fitted for each relative time interval between the end of nucleoid splitting and cell division, describing the rate of distance increase between the separated sister nucleoids (σ, response variable) as a function of the polysome concentration increase rate (ρ), the rate of cell elongation (λ), their interaction (ρλ), and noise (ε) (*statsmodels.formula.api.ols*) as follows:

$$\sigma = \beta_0 + \beta_1\rho + \beta_2\lambda + \beta_3(\rho\lambda) + \varepsilon \qquad \text{[eq. 3]}$$

The single cell data were scaled by subtracting the population mean and then dividing by the standard deviation prior to model fitting for each of the four relative time intervals (in Figure 1 – figure supplement 5B). The coefficients of the linear regression model (shown in Figure 1I) provide a measure of the relative effect of the independent variables on the dependent variable. The cell elongation (λ) had a statistically significant effect to the response variable (σ) Prob(>|Z|) < 10^{-9}) across all relative time intervals. The polysome accumulation coefficients (ρ) had a statistically significant effect to the response variable (σ) (Prob(>|Z|) < 10^{-14}) for the first three relative time intervals (0-25%, 25-50% and 50-75%) and a marginally significant one Prob(>|Z|) = 0.02) for the last quartile (75-100%). The interaction term (ρλ) had a marginally significant effect (Prob(>|Z|) = 0.002) for the first quartile (0-25%) yet with a very small coefficient of 0.06 and did not present any significance (Prob(>|Z|) > 0.05) for the remaining time intervals (25-50%, 50-75% and 75-100%). Hence, it is not shown in Figure 1I. The most significant effect on the migration of the sister nucleoids (σ) was presented by the rate of polysome accumulation at mid-cell (ρ), 0-25% from the end of nucleoid splitting to cell division, with a coefficient of 0.46 and Prob(>|Z|) < 10^{-84}.

Calculation of rates

The rates of the polysome accumulation ($\frac{\Delta RplA_{mid-nuc}\ conc.}{\Delta T}$) or nucleoid depletion ($\frac{\Delta HupA_{mid-nuc}\ conc.}{\Delta T}$) in the middle of the nucleoid (2.5 pixels adjacent the nucleoid center) (Figure 1F), correspond to the slope of a linear regression (Python fitting function: *numpy.polyfit*) fitted to the change of the mid-nucleoid RplA-GFP or HupA-mCherry concentration over time, 40-90% into the nucleoid segregation cycle (as in Figure 1E). This nucleoid cycle interval corresponds to the average time from the initiation of nucleoid splitting to just before its completion. Choosing the appropriate range to correlate the two statistics was important since

polysomes appeared to accumulate in the middle of the nucleoid before the onset of nucleoid splitting (Figures 1E and Figure 1 – figure supplement 6D).

The rate of RplA-GFP concentration increase at mid-cell ($\frac{\Delta RplA_{mid-cell\ conc.}}{\Delta T}$) was calculated (Figure 1H) within a region covering 10% of the total cell length at the cell center. The same results were obtained when the rates were calculated within a cell region covering 2.5 pixels adjacent to the cell center. The rate of nucleoid migration ($\frac{\Delta Distance_{nuc}}{\Delta T}$) corresponds to the slope of a linear regression that describes the natural log-transformed distance increase between the separated sister nucleoids over time (Figure 1H). Similarly, the rate of cell elongation ($\frac{\Delta Length_{cell}}{\Delta T}$) was calculated considering the natural log-transformed cell length increase over time (Figure 1H). The rate of RplA-GFP concentration increase at mid-cell ($\frac{\Delta RplA_{mid-cell\ conc.}}{\Delta T}$), the rate of nucleoid migration ($\frac{\Delta Distance_{nuc}}{\Delta T}$), and the rate of cell elongation ($\frac{\Delta Length_{cell}}{\Delta T}$) were calculated within four relative time intervals from the end of nucleoid splitting to cell division (Figure 1G and Figure 1 – figure supplement 5B). Only single nucleoid migration intervals with more than four timepoints were considered to ensure a reliable fitting. The small fraction (~8%) of cells that were born with two separately detected nucleoid objects, which indicates that the end of nucleoid splitting occurred in the previous cell division cycle, were removed from the analysis. The cell division cycles with a negative cell elongation rate (<1%) were also excluded from the analysis.

Reaction-diffusion model

Our theoretical model is an extension of previous work (Miangolarra et al., 2021), which showed that steric effects between the DNA and the transcription-translation machinery (including polysomes) are sufficient to drive nucleoid segregation. To simply describe these interactions, we employed the Flory-Huggins theory for regular solutions (Flory, 1942; Huggins, 1941) and modeled the non-dimensionalized free-energy density f as a function of the local volume fractions of the nucleoid (n) and polysomes (p):

$$f(n,p) = \frac{p}{v_p}\ln p + \frac{n}{v_n}\ln n + (1-p-n)\ln(1-p-n) + \chi_p p(1-p-n) + \chi_n n(1-p-n) + \chi_{np} np - \kappa_p \nabla p \nabla(1-p-n) - \kappa_n \nabla n \nabla(1-p-n) - \kappa_{np}\nabla n \nabla p\,. \qquad \text{[eq. 4]}$$

Here, $(1-n-p)$ is the volume fraction of the cytoplasm not occupied by nucleoid or polysomes, whereas v_n and v_p are proportional to the molecular volumes of the elementary translational degrees of freedom (i.e., of the nucleoid element and single polysome, respectively). χ_p, χ_n and χ_{np} are the Flory-Huggins interaction parameters, and κ_p, κ_n and κ_{np} are the interfacial tensions. We take $\kappa_{ij} = \lambda^2\chi_{ij}$, with λ being a characteristic interface width.

The time evolution of the volume fractions is described by a combination of Cahn-Hilliard theory (Cahn and Hilliard, 1958) and the reactions kinetics of the polysomes. We assume that polysomes are produced inside the nucleoid at a constant rate k_1 and degraded uniformly along the cell at a rate k_{-1}:

$$\frac{\partial p}{\partial t} = \nabla\left(M_p \nabla \mu_p\right) + k_1 n - k_{-1} p \ , \quad \text{[eq. 5]}$$

$$\frac{\partial n}{\partial t} = \nabla(M_n \nabla \mu_n), \quad \text{[eq. 6]}$$

where $\mu_p = \frac{\delta F}{\delta p}$ and $\mu_n = \frac{\delta F}{\delta n}$ are the local chemical potentials of polysomes and nucleoid elements respectively, with $F = \int f[n(x), p(x)]dx$ representing the total free energy. $M_p = v_p D_p p$ and $M_n = v_n D_n n$ are the mobility coefficients of the polysomes and the nucleoid, respectively, which depend on the diffusion coefficients of the polysomes (D_p) and the nucleoid (D_n). This recovers the Fick law of diffusion in the noninteracting limit.

Since *E. coli* grows by elongation while maintaining its cylindrical shape and cell width, we reduce the problem to one dimension, with x representing the position along the long axis of the cell. We assume that the cell length grows exponentially such that the length at time t is $L(t) = L(0)e^{\gamma t}$, with γ being the growth rate and $L(0)$ the initial cell length at birth. Exponential growth dilutes the existing polysomes with rate γ. On the other hand, we assume that the nucleoid is not diluted since DNA replication occurs continuously, and the nucleoid length is known to grow in proportion to cell length (Gray et al., 2019). Letting $\tilde{x} = x/L(t)$ be the relative position along the cell's long axis, the time evolution is given by:

$$\frac{\partial p}{\partial t} = \partial_{\tilde{x}}\left(\widetilde{M}_p \partial_{\tilde{x}} \mu_p\right) + k_1 n - (k_{-1} + \gamma)p, \quad \text{[eq. 7]}$$

$$\frac{\partial n}{\partial t} = \partial_{\tilde{x}}\left(\widetilde{M}_n \partial_{\tilde{x}} \mu_n\right), \quad \text{[eq. 8]}$$

where $\partial_{\tilde{x}} = \frac{\partial}{\partial \tilde{x}} = L(t)\frac{\partial}{\partial x}$, and $\widetilde{M}_{n,p} = M_{n,p} L(t)^{-2}$. The chemical potentials are:

$$\mu_p = v_p^{-1} \ln p - \ln(1 - p - n) + \chi_p(1 - 2p - n) + \left(\chi_{np} - \chi_n\right)n$$
$$-\chi_p \tilde{\lambda}^2 \partial_{\tilde{x}}^2 (2p + n) + \left(\chi_{np} - \chi_n\right)\tilde{\lambda}^2 \partial_{\tilde{x}}^2 n, \quad \text{[eq. 9]}$$

$$\mu_n = v_n^{-1} \ln n - \ln(1 - p - n) + \chi_n(1 - 2n - p) + \left(\chi_{np} - \chi_p\right)p$$
$$-\chi_n \tilde{\lambda}^2 \partial_{\tilde{x}}^2 (2n + p) + \left(\chi_{np} - \chi_p\right)\tilde{\lambda}^2 \partial_{\tilde{x}}^2 p, \quad \text{[eq. 10]}$$

where $\tilde{\lambda} = \lambda/L(t)$.

We take the non-dimensionalized Flory-Huggins interaction parameters to be $\chi_p = 0.2$, $\chi_n = 0.4$ and $\chi_{np} = 1.2$. The χ_{np} parameter captures the steric repulsion between the nucleoid and the polysomes (Miangolarra et al., 2021). The diffusion coefficient of the polysome was set to $D_p = 0.023\mu m^2/s$, which lies within the same order of magnitude as was previously measured by single-molecule tracking (Bakshi et al., 2012b). For simplicity, we adopt an average description of all polysomes with an average diffusion coefficient. Considering multiple polysome species does not change the physical picture. To illustrate, we considered an extension of our model, which contains three polysome species, each with a different diffusion coefficient (DP = 0.018, 0.023, or 0.028 μm2/s), reflecting that polysomes with more ribosomes will have a lower diffusion coefficient. Simulation of this model reveals that the different polysome species have essentially the same concentration distribution (Figure 4 — figure supplement 4), suggesting that the average description in our minimal model is sufficient for our purposes.

Different diffusion coefficients were tested for the nucleoid ($D_n = 0.0005, 0.001 \text{ or } 0.005\ \mu\text{m}^2/\text{s}$) to capture different levels of nucleoid stiffness and hence response time to the local changes in polysome concentration. The polysome degradation rate was set to $k_{-1} = 0.003\text{s}^{-1}$, which corresponds to a half-life of around 5 min (Bernstein et al., 2004). We take the polysome production rate to be $k_1 = k_{1,0}\left(1 + \frac{\gamma}{k_{-1}}\right)$, with $k_{1,0} = 0.002\text{s}^{-1}$, to match the observation that the nucleoid length is proportional to cell length (Gray et al., 2019). The initial cell length $L(0)$ matched the cell length at birth, which has been previously shown to increase exponentially with the growth rate (Govers et al., 2024). Hence, each of the simulated growth rates ($\gamma = 0.25, 0.36, 0.46, 0.57, 0.67, 0.78, 0.88, 0.99, 1.09, 1.2\ \text{h}^{-1}$) was matched to a cell length at birth (Figure 4 – figure supplement 2) by fitting a linear regression ($L(0) = l_0 e^{\gamma/\gamma_0}$, with fitted parameters $l_0 = 2.00\ \mu\text{m}$ and $\gamma_0 = 2.81\ \text{h}^{-1}$) to the experimental data (Govers et al., 2024). Other parameters are chosen as follows: $\lambda = 0.03\ \mu\text{m}$, $v_n = 10$, $v_p = 5$.

The dynamic equations (eqs. 7-8) were solved numerically in a fixed 1D domain $\tilde{x} \in (0,1)$, with no-flux boundary conditions. Space is discretized into $N = 128$ grid points, and time is discretized to steps of Δt. Time stepping was implemented with an implicit-explicit scheme as previously demonstrated (Mao et al., 2020, 2019). The simulations were initialized from the (symmetric) steady-state solution of the system at the initial cell length $L(0)$ (Figure 4B, dashed curves in Figure 4E, and Movie S3), or using the (asymmetric) macromolecular distribution of the predivisional cell of the former simulation as the initial condition (Figure 4D, solid curves in Figure 4E), which allowed us to capture cell polarity (new versus old pole). The cell length $L(t)$ was updated and recorded at each time step during the simulation. The nucleoid splitting time (shown in Figure 4D) was determined by thresholding the relative decrease of the nucleoid concentration at the cell center. A depletion threshold of 30% was used to mark the event of nucleoid splitting.

The *p* field in our model describes the distribution of all polysomes, which could include one, two, or multiple ribosomes (in this paper the term "polysomes" refers to both monosomes and true polysomes). For simplicity, we adopt an average description of all polysomes with an average diffusion coefficient and interaction parameters, which is sufficient for capturing the fundamental mechanism underlying nucleoid segregation. The model can be extended to include multiple polysome species: $p = \sum_i p_i$, with each species' evolution following Eq. 5 with a different diffusion coefficient. Figure 4 – figure supplement 4 shows an example containing 3 polysome species, with diffusion coefficients $D_p = 0.018, 0.023, 0.028\ \mu\mathrm{m}^2/\mathrm{s}$.

Our model can also be extended to consider ectopic polysome production, which introduces an additional polysome production term:

$$\frac{\partial p}{\partial t} = \nabla\left(M_p \nabla \mu_p\right) + k_1' n - k_{-1} p + k_{\mathrm{ect}}(x)\ , \quad \text{[eq. 5*]}$$

where $k_{\mathrm{ect}}(x)$ describes ectopic polysome production from plasmids, with x being the distance from one pole measured in μm. k_1' represents a reduced polysome production rate in the nucleoid. Figure 7 – figure supplement 2 shows two examples with details as follows. For ectopic production near the poles, we use $k_{\mathrm{ect}}(x) = 0.8\, k_1\, \Theta(x)\, \Theta(0.8 - x)$ and $k_1' = 0.5 k_1$, where $\Theta(x)$ is the Heaviside step function; this restricts ectopic production to within $0.8\ \mu$m from one pole. For ectopic production between sister nucleoids, we use $k_{\mathrm{ect}}(x) = 0.5\, k_1\, \Theta\left(0.4 - \left|\frac{L}{2} - x\right|\right)$ and $k_1' = 0.5 k_1$, where L is the cell length; this restricts ectopic production to within $0.4\ \mu$m from mid-cell. These ectopic production rates are for illustrative purposes only and the qualitative result does not depend sensitively on parameter values.

The code for the model (including scripts to reproduce all simulation figures) is available at https://github.com/qiweiyuu/polysome.

Polysome and nucleoid analysis based on fitted Gaussian functions

Quantification of polysome and nucleoid asymmetries within cells along the cell division cycle was achieved by fitting Gaussian functions (Python least squares optimization: *scipy.optimize.curve_fit*) to the RplA-GFP or the HupA-mCherry intensity profiles of cells growing in M9gluCAAT in the microfluidic device. Three Gaussian functions were fitted to the polysome signal concentration early in the cell division cycle. Two of them captured the nucleoid-excluded polysomes accumulating at the poles and the third captured the polysome accumulation in the middle of nucleoid (Figure 3 – figure supplement 1A-B):

$$Poly(l) = A_{old} \exp\left(-\frac{1}{2}\left(\frac{l_{old} - l}{\sigma_{old}}\right)^2\right) + A_{mid} \exp\left(-\frac{1}{2}\left(\frac{l_{mid} - l}{\sigma_{mid}}\right)^2\right) + A_{new} \exp\left(-\frac{1}{2}\left(\frac{l_{new} - l}{\sigma_{new}}\right)^2\right) \quad \text{[eq. 11]},$$

where A_{old}, A_{new} and A_{mid} are the amplitudes, l_{old}, l_{new} and l_{mid} are the means, and σ_{old}, σ_{new} and σ_{mid} are the standard deviations of the respective fitted functions along the relative cell length (l).

Two Gaussian functions were fitted to the concentration of constricting nucleoids (Figure 3 – figure supplement 1A-B):

$$Nuc(l) = A_{old} \exp\left(-\frac{1}{2}\left(\frac{l_{old}-l}{\sigma_{old}}\right)^2\right) + A_{new} \exp\left(-\frac{1}{2}\left(\frac{l_{new}-l}{\sigma_{new}}\right)^2\right) \qquad \text{[eq. 12]}$$

All Gaussian functions were fitted over the cell background fluorescence, which corresponds to the baseline fluorescence within the masked cell boundaries and along the relative cell length coordinates from the old pole (-1) via the cell center (0) to the new pole (1). The Gaussian functions were fitted either to single newborn cells (0-2.5% into the cell division cycle) as shown in Figure 3 – figure supplement 1A-B and as applied in Figures 3A and 3E, or to the less noisy average intensity profile of the segmented cells within the 0-10% range of their cell division cycle, as shown in Figure 3 – figure supplement 1C-D and used in Figures 3B and 3F. The areas of the Gaussian functions fitted to the polysomes (used in Figure 3A-B) were estimated using the function:

$$Area = A\,\sigma\sqrt{2\pi} \qquad \text{[eq. 13]},$$

where A is the amplitude and σ *is* the standard deviation.

The Gaussian areas were used to quantify the polysome asymmetries between the poles:

$$Poly_{asym} = log_{10}\left(\frac{Area_{new}}{Area_{old}}\right) \qquad \text{[eq. 14]},$$

where $Area_{new}$ and $Area_{old}$ are the areas of the fitted Gaussians to the nucleoid-excluded polysomes accumulating in the new and the old pole, respectively. The statistic in eq. 14 corresponds to the x-axis in Figure 3B. It is a positive value when the new pole contains more polysomes than the old one, and a negative value when the old pole contains more polysomes than the new one.

The nucleoid Gaussian statistics were used to quantify the nucleoid position asymmetry defined as:

$$Nuc_{pos} = \frac{l_{new}+l_{old}}{2}\,\frac{l_{cell}}{2} \qquad \text{[eq. 15]},$$

and the nucleoid compaction asymmetry was calculated as:

$$Nuc_{comp} = \frac{A_{new}}{A_{old}} \qquad \text{[eq. 16]},$$

where l_{old} and l_{new} are the means of the nucleoid Gaussians in relative cell coordinates (as in eq. 12) and l_{cell} is the cell length in µm. The nucleoid position was first estimated in relative cell coordinates from the old pole (-1) via the cell center (0) to the new pole (1) and then multiplied by half the cell length to convert to absolute cell length units. A_{old} and A_{new} are the amplitudes of the fitted nucleoid Gaussians (as in eq. 12) in arbitrary fluorescence units. The nucleoid position corresponds to the mid-point between the two Gaussian

means (eq. 15) and is a positive number when the nucleoid is shifted toward the new pole and a negative number when it is positioned closer to the old pole (y-axis in Figure 3B).

The nucleoid compaction asymmetry was calculated as the relative nucleoid Gaussian amplitude (eq. 16). It had a positive value greater than 1 when the nucleoid concentration was higher toward the new pole and had a positive value smaller than 1 if the nucleoid was more concentrated toward the old pole (y-axis in Figure 3F).

To determine which polysome Gaussian statistics and related asymmetries may contribute to nucleoid compaction asymmetry (eq. 16), a linear mixed-effects model was used (*statsmodel* package in Python, *statsmodels.formula.api.mixedlm* function). The polysome Gaussian statistics were used as independent variables and the nucleoid compaction asymmetry as a dependent variable:

$$Nuc_{comp} = \beta_0 + \beta_1 l_{old} + \beta_2 l_{mid} + \beta_3 l_{new} + \beta_4 \sigma_{old} + \beta_5 \sigma_{mid} + \beta_6 \sigma_{new} + \beta_7 A_{old} + \beta_8 A_{mid} + \beta_9 A_{new} + \varepsilon \quad \text{[eq. 17]},$$

where β_0 is the constant (intercept), β_n *(n=1,2…,9)* are the coefficients for each of the polysome Gaussian statistics (same as in eq. 4 and plotted in Figure 3 – figure supplement 2A-B), and ε is the error. The entire dataset was treated as a single group. Before fitting the linear mixed-effects model, all data were normalized by subtracting the average and dividing the resulting value by their standard deviation (Figure 3 – figure supplement 2B). The relative cell length positions of the polysomes at the old pole (l_{old}) and in the middle of the nucleoid (l_{mid}) were found to significantly influence the asymmetric nucleoid compaction (Figure 3 – figure supplement 2C). We reasoned that the available spaces between the polysome positions (Figure 3 – figure supplement 2A) may influence the compaction of the nucleoid and devised a new statistic that compares the available polysome-free space toward the new pole to that of toward the old pole:

$$Poly_{space} = \frac{l_{new} - l_{mid}}{l_{mid} - l_{old}} \quad \text{[eq. 18]},$$

where l_{new}, l_{mid} and l_{old} are the polysome Gaussian means (as in eq. 11), which represent the positions of the polysomes at the new pole, mid-cell region, and old pole, respectively, expressed as relative cell coordinates from the old pole (-1) via the cell center (0) to the new pole (1). The fraction above (eq. 18) has a value greater than 1 when the polysome-free space is greater toward the new pole and a value smaller than 1 when the polysome-free space is greater toward the old pole (x-axis in Figure 3F).

Linear regressions

Two types of linear regressions were used in this work. In Figure 2B, a first-degree polynomial was fitted using the ordinary least squares method and the numpy library in Python (*numpy.polyfit*), always using the

x-axis as the independent variable and the *y*-axis as the dependent variable. In Figures 1F and 3B, a principal component regression was fitted using the scikit-learn library in Python (*sklearn.decomposition.PCA*). A principal component analysis was first applied on the two-dimensional z-transformed data to find the linear regressor that explained most of the variance (the first principal component). This linear regressor was then rescaled to the original 2D plane. The principal component regression eliminates the dependent variable bias associated with a traditional univariate fit. This bias is introduced when calculating the prediction error (sum of squares) only along the dependent variable axis during the least squares optimization. The elimination of this univariate bias is particularly important for the fitted regressions in Figures 1F and 3B since their parameters were used to estimate the rate of nucleoid splitting in the absence of polysome accumulation in the middle (y-intercept in Figure 1F), the position of the nucleoid with equal polysomes at the poles (y-intercept in Figure 3B), or the polar asymmetry required for a centered nucleoid (x-intercept in Figure 3B).

Kernel density estimations

One-dimensional (Figures 3A, E, and Figure 1- figure supplement 4C) or two-dimensional (Figures 1F, 1H, Figure 1 – figure supplement 5A-B, and Figure 3 – figure supplement 2B) Gaussian kernel density estimations were fitted using the *scipy.stats.gaussian_kde* method. The bandwidth was determined using Scott's rule (Scott, 1992).

Correlation coefficient calculations

All Spearman correlation coefficients (referred to as Spearman ρ) were estimated using the *scipy.stats* Python library and the *spearmanr* function. Only those Spearman correlation coefficients with a p-value below 0.05 are shown. Otherwise, the correlation is annotated as not-significant (NS) (as in Figure 1 – figure supplement 5B).

ADDITIONAL RESOURCES

This study did not generate any additional resources.

ACKNOWLEDGMENTS

We are grateful to Dr. A Janakiraman (City College of New York) for the pER12 (pBAD322A-gfp-μNS) plasmid, Dr K. Prather (Massachusetts Institute of Technology) for the MG1655 (DE3) strain, and the members of the Jacobs-Wagner laboratory for fruitful discussions and critical reading of the manuscript. This work was supported in part by the National Institutes of Health (R01 GM082938 to N.S.W.) and by the Netherlands Organization for Scientific Research (research program Rubicon Science 2018-1, project number 019.181EN.018 to A.P). C.J.W. is an investigator of the Howard Hughes Medical Institute.

AUTHOR CONTRIBUTIONS

Conceptualization, A.P. and C.J.-W.; methodology, A.P.; software, A.P. and Q.Y.; formal analysis, A.P.; investigation, A.P., Q.Y, and S.K.G.; resources, A.P., Q.Y., and W.-H.L.; data curation, A.P.; writing – original draft, A.P. and C.J.-W.; writing – review and editing, A.P., C.J.-W , N. W., Q.Y., S.K.G., and W.-H.L; visualization, A.P. and C.J.-W.; supervision, N.W. and C.J.-W.; project administration, C.J.-W.; funding acquisition, A.P., N.W. and C.J.-W.

DECLARATION OF INTERESTS

The authors declare no competing interests.

DATA AVAILABILITY

The microscopy images and dataframes used on this study are available on BioStudies and the BioImage Archive (accession # S-BIAD-1658).

REFERENCES

Bakshi, S., Choi, H., Mondal, J., Weisshaar, J.C., 2014. Time-dependent effects of transcription- and translation-halting drugs on the spatial distributions of the *E scherichia coli* chromosome and ribosomes: Time-dependent drug effects on *E. coli* chromosome spatial distribution. Mol. Microbiol. 94, 871–887. https://doi.org/10.1111/mmi.12805

Bakshi, S., Choi, H., Weisshaar, J.C., 2015. The spatial biology of transcription and translation in rapidly growing Escherichia coli. Front. Microbiol. 6. https://doi.org/10.3389/fmicb.2015.00636

Bakshi, S., Siryaporn, A., Goulian, M., Weisshaar, J.C., 2012a. Superresolution imaging of ribosomes and RNA polymerase in live Escherichia coli cells. Mol. Microbiol. 85, 21–38. https://doi.org/10.1111/j.1365-2958.2012.08081.x

Bakshi, S., Siryaporn, A., Goulian, M., Weisshaar, J.C., 2012b. Superresolution imaging of ribosomes and RNA polymerase in live Escherichia coli cells: Superresolution imaging of ribosome and RNAP. Mol. Microbiol. 85, 21–38. https://doi.org/10.1111/j.1365-2958.2012.08081.x

Balakrishnan, R., Mori, M., Segota, I., Zhang, Z., Aebersold, R., Ludwig, C., Hwa, T., 2022. Principles of gene regulation quantitatively connect DNA to RNA and proteins in bacteria. Science 378, eabk2066. https://doi.org/10.1126/science.abk2066

Bartosik, A.A., Mierzejewska, J., Thomas, C.M., Jagura-Burdzy, G., 2009. ParB deficiency in Pseudomonas aeruginosa destabilizes the partner protein ParA and affects a variety of physiological parameters. Microbiology 155, 1080–1092. https://doi.org/10.1099/mic.0.024661-0

Bates, D., Kleckner, N., 2005. Chromosome and Replisome Dynamics in E. coli: Loss of Sister Cohesion Triggers Global Chromosome Movement and Mediates Chromosome Segregation. Cell 121, 899–911. https://doi.org/10.1016/j.cell.2005.04.013

Bean, G.J., Flickinger, S.T., Westler, W.M., McCully, M.E., Sept, D., Weibel, D.B., Amann, K.J., 2009. A22 Disrupts the Bacterial Actin Cytoskeleton by Directly Binding and Inducing a Low-Affinity State in MreB. Biochemistry 48, 4852–4857. https://doi.org/10.1021/bi900014d

1588 Bernstein, J.A., Lin, P.-H., Cohen, S.N., Lin-Chao, S., 2004. Global analysis of *Escherichia coli*
1589 RNA degradosome function using DNA microarrays. Proc. Natl. Acad. Sci. 101, 2758–
1590 2763. https://doi.org/10.1073/pnas.0308747101
1591 Binenbaum, Z., Parola, A.H., Zaritsky, A., Fishov, I., 1999. Transcription- and translation-
1592 dependent changes in membrane dynamics in bacteria: testing the transertion model for
1593 domain formation. Mol. Microbiol. 32, 1173–1182. https://doi.org/10.1046/j.1365-
1594 2958.1999.01426.x
1595 Blundell, M.R., Wild, D.G., 1971. Altered ribosomes after inhibition of *Escherichia coli* by
1596 rifampicin. Biochem. J. 121, 391–398. https://doi.org/10.1042/bj1210391
1597 Brandt, F., Etchells, S.A., Ortiz, J.O., Elcock, A.H., Hartl, F.U., Baumeister, W., 2009. The
1598 Native 3D Organization of Bacterial Polysomes. Cell 136, 261–271.
1599 https://doi.org/10.1016/j.cell.2008.11.016
1600 Broering, T.J., Arnold, M.M., Miller, C.L., Hurt, J.A., Joyce, P.L., Nibert, M.L., 2005. Carboxyl-
1601 Proximal Regions of Reovirus Nonstructural Protein μNS Necessary and Sufficient for
1602 Forming Factory-Like Inclusions. J. Virol. 79, 6194–6206.
1603 https://doi.org/10.1128/JVI.79.10.6194-6206.2005
1604 Broering, T.J., Parker, J.S.L., Joyce, P.L., Kim, J., Nibert, M.L., 2002. Mammalian Reovirus
1605 Nonstructural Protein μNS Forms Large Inclusions and Colocalizes with Reovirus
1606 Microtubule-Associated Protein μ2 in Transfected Cells. J. Virol. 76, 8285–8297.
1607 https://doi.org/10.1128/JVI.76.16.8285-8297.2002
1608 Bryksin, A.V., Matsumura, I., 2010. Overlap extension PCR cloning: a simple and reliable way
1609 to create recombinant plasmids. BioTechniques 48, 463–465.
1610 https://doi.org/10.2144/000113418
1611 Cabrera, J.E., Cagliero, C., Quan, S., Squires, C.L., Jin, D.J., 2009. Active Transcription of
1612 rRNA Operons Condenses the Nucleoid in *Escherichia coli* : Examining the Effect of
1613 Transcription on Nucleoid Structure in the Absence of Transertion. J. Bacteriol. 191,
1614 4180–4185. https://doi.org/10.1128/JB.01707-08
1615 Cahn, J.W., Hilliard, J.E., 1958. Free Energy of a Nonuniform System. I. Interfacial Free Energy.
1616 J. Chem. Phys. 28, 258–267. https://doi.org/10.1063/1.1744102
1617 Campbell, E.A., Korzheva, N., Mustaev, A., Murakami, K., Nair, S., Goldfarb, A., Darst, S.A.,
1618 2001. Structural Mechanism for Rifampicin Inhibition of Bacterial RNA Polymerase.
1619 Cell 104, 901–912. https://doi.org/10.1016/S0092-8674(01)00286-0
1620 Campos, M., Govers, S.K., Irnov, I., Dobihal, G.S., Cornet, F., Jacobs-Wagner, C., 2018.
1621 Genomewide phenotypic analysis of growth, cell morphogenesis, and cell cycle events in
1622 *Escherichia coli*. Mol. Syst. Biol. 14, e7573. https://doi.org/10.15252/msb.20177573
1623 Campos, M., Surovtsev, I.V., Kato, S., Paintdakhi, A., Beltran, B., Ebmeier, S.E., Jacobs-
1624 Wagner, C., 2014. A constant size extension drives bacterial cell size homeostasis. Cell
1625 159, 1433–1446. https://doi.org/10.1016/j.cell.2014.11.022
1626 Cass, J.A., Kuwada, N.J., Traxler, B., Wiggins, P.A., 2016. Escherichia coli Chromosomal Loci
1627 Segregate from Midcell with Universal Dynamics. Biophys. J. 110, 2597–2609.
1628 https://doi.org/10.1016/j.bpj.2016.04.046
1629 Castellana, M., Hsin-Jung Li, S., Wingreen, N.S., 2016. Spatial organization of bacterial
1630 transcription and translation. Proc. Natl. Acad. Sci. 113, 9286–9291.
1631 https://doi.org/10.1073/pnas.1604995113

1632 Chai, Q., Singh, B., Peisker, K., Metzendorf, N., Ge, X., Dasgupta, S., Sanyal, S., 2014.
1633 Organization of Ribosomes and Nucleoids in Escherichia coli Cells during Growth and in
1634 Quiescence. J. Biol. Chem. 289, 11342–11352. https://doi.org/10.1074/jbc.M114.557348
1635 Chao, L., Chan, C.K., Shi, C., Rang, U.C., 2024. Spatial and temporal distribution of ribosomes
1636 in single cells reveals aging differences between old and new daughters of Escherichia
1637 coli. eLife 12, RP89543. https://doi.org/10.7554/eLife.89543.3
1638 Charaka, V.K., Misra, H.S., 2012. Functional Characterization of the Role of the Chromosome I
1639 Partitioning System in Genome Segregation in Deinococcus radiodurans. J. Bacteriol.
1640 194, 5739–5748. https://doi.org/10.1128/JB.00610-12
1641 Cherepanov, P.P., Wackernagel, W., 1995. Gene disruption in Escherichia coli: TcR and KmR
1642 cassettes with the option of Flp-catalyzed excision of the antibiotic-resistance
1643 determinant. Gene 158, 9–14. https://doi.org/10.1016/0378-1119(95)00193-A
1644 Chure, G., Cremer, J., 2023. An optimal regulation of fluxes dictates microbial growth in and out
1645 of steady state. eLife 12, e84878. https://doi.org/10.7554/eLife.84878
1646 Cooper, S., Hsieh, M.L., 1988. The Rate and Topography of Cell Wall Synthesis during the
1647 Division Cycle of Escherichia coli Using N-Acetylglucosamine as a Peptidoglycan Label.
1648 Microbiology 134, 1717–1721. https://doi.org/10.1099/00221287-134-6-1717
1649 Coquel, A.-S., Jacob, J.-P., Primet, M., Demarez, A., Dimiccoli, M., Julou, T., Moisan, L.,
1650 Lindner, A.B., Berry, H., 2013. Localization of Protein Aggregation in Escherichia coli Is
1651 Governed by Diffusion and Nucleoid Macromolecular Crowding Effect. PLoS Comput.
1652 Biol. 9, e1003038. https://doi.org/10.1371/journal.pcbi.1003038
1653 Cutler, K.J., Stringer, C., Lo, T.W., Rappez, L., Stroustrup, N., Brook Peterson, S., Wiggins,
1654 P.A., Mougous, J.D., 2022. Omnipose: a high-precision morphology-independent
1655 solution for bacterial cell segmentation. Nat. Methods 19, 1438–1448.
1656 https://doi.org/10.1038/s41592-022-01639-4
1657 Dai, X., Zhu, M., Warren, M., Balakrishnan, R., Patsalo, V., Okano, H., Williamson, J.R.,
1658 Fredrick, K., Wang, Y.-P., Hwa, T., 2017. Reduction of translating ribosomes enables
1659 Escherichia coli to maintain elongation rates during slow growth. Nat. Microbiol. 2,
1660 16231. https://doi.org/10.1038/nmicrobiol.2016.231
1661 Danilova, O., Reyes-Lamothe, R., Pinskaya, M., Sherratt, D., Possoz, C., 2007. MukB
1662 colocalizes with the oriC region and is required for organization of the two Escherichia
1663 coli chromosome arms into separate cell halves. Mol. Microbiol. 65, 1485–1492.
1664 https://doi.org/10.1111/j.1365-2958.2007.05881.x
1665 Datsenko, K.A., Wanner, B.L., 2000. One-step inactivation of chromosomal genes in
1666 *Escherichia coli* K-12 using PCR products. Proc. Natl. Acad. Sci. 97, 6640–6645.
1667 https://doi.org/10.1073/pnas.120163297
1668 Davis, J.H., Rubin, A.J., Sauer, R.T., 2011. Design, construction and characterization of a set of
1669 insulated bacterial promoters. Nucleic Acids Res. 39, 1131–1141.
1670 https://doi.org/10.1093/nar/gkq810
1671 Donczew, M., Mackiewicz, P., Wróbel, A., Flärdh, K., Zakrzewska-Czerwińska, J., Jakimowicz,
1672 D., 2016. ParA and ParB coordinate chromosome segregation with cell elongation and
1673 division during *Streptomyces* sporulation. Open Biol. 6, 150263.
1674 https://doi.org/10.1098/rsob.150263
1675 Donovan, C., Schwaiger, A., Krämer, R., Bramkamp, M., 2010. Subcellular Localization and
1676 Characterization of the ParAB System from *Corynebacterium glutamicum*. J. Bacteriol.
1677 192, 3441–3451. https://doi.org/10.1128/JB.00214-10

1678 Dourado, H., Lercher, M.J., 2020. An analytical theory of balanced cellular growth. Nat.
1679 Commun. 11, 1226. https://doi.org/10.1038/s41467-020-14751-w
1680 Du, W.-L., Dubarry, N., Passot, F.M., Kamgoué, A., Murray, H., Lane, D., Pasta, F., 2016.
1681 Orderly Replication and Segregation of the Four Replicons of Burkholderia cenocepacia
1682 J2315. PLOS Genet. 12, e1006172. https://doi.org/10.1371/journal.pgen.1006172
1683 Dworkin, J., Losick, R., 2002. Does RNA polymerase help drive chromosome segregation in
1684 bacteria? Proc. Natl. Acad. Sci. 99, 14089–14094.
1685 https://doi.org/10.1073/pnas.182539899
1686 Dworsky, P., Schaechter, M., 1973. Effect of Rifampin on the Structure and Membrane
1687 Attachment of the Nucleoid of *Escherichia coli*. J. Bacteriol. 116, 1364–1374.
1688 https://doi.org/10.1128/jb.116.3.1364-1374.1973
1689 Farrar, A., Turner, P., El Sayyed, H., Feehily, C., Chatzimichail, S., Ta, S., Crook, D.,
1690 Andersson, M., Oakley, S., Barrett, L., Nellåker, C., Stoesser, N., Kapanidis, A., 2025.
1691 Ribosome phenotypes for rapid classification of antibiotic-susceptible and resistant
1692 strains of Escherichia coli. Commun. Biol. 8, 319. https://doi.org/10.1038/s42003-025-
1693 07740-6
1694 Figge, R.M., Easter, J., Gober, J.W., 2003. Productive interaction between the chromosome
1695 partitioning proteins, ParA and ParB, is required for the progression of the cell cycle in
1696 Caulobacter crescentus: Dominant-negative ParB alleles. Mol. Microbiol. 47, 1225–1237.
1697 https://doi.org/10.1046/j.1365-2958.2003.03367.x
1698 Fisher, J.K., Bourniquel, A., Witz, G., Weiner, B., Prentiss, M., Kleckner, N., 2013. Four-
1699 Dimensional Imaging of E. coli Nucleoid Organization and Dynamics in Living Cells.
1700 Cell 153, 882–895. https://doi.org/10.1016/j.cell.2013.04.006
1701 Flory, P.J., 1942. Thermodynamics of High Polymer Solutions. J. Chem. Phys. 10, 51–61.
1702 https://doi.org/10.1063/1.1723621
1703 Forchhammer, J., Lindahl, L., 1971. Growth rate of polypeptide chains as a function of the cell
1704 growth rate in a mutant of Escherichia coli 15. J. Mol. Biol. 55, 563–568.
1705 https://doi.org/10.1016/0022-2836(71)90337-8
1706 Gibson, D.G., Young, L., Chuang, R.-Y., Venter, J.C., Hutchison, C.A., Smith, H.O., 2009.
1707 Enzymatic assembly of DNA molecules up to several hundred kilobases. Nat. Methods 6,
1708 343–345. https://doi.org/10.1038/nmeth.1318
1709 Gillies, Sean, van der Wel, Casper, Van den Bossche, Joris, Taves, Mike W., Arnott, Joshua,
1710 Ward, Brendan C., Others, 2023. Shapely. https://doi.org/10.5281/ZENODO.5597138
1711 Govers, S.K., Campos, M., Tyagi, B., Laloux, G., Jacobs-Wagner, C., 2024. Apparent simplicity
1712 and emergent robustness in the control of the Escherichia coli cell cycle. Cell Syst. 15,
1713 19-36.e5. https://doi.org/10.1016/j.cels.2023.12.001
1714 Gray, A.N., Egan, A.J., Van'T Veer, I.L., Verheul, J., Colavin, A., Koumoutsi, A., Biboy, J.,
1715 Altelaar, A.F.M., Damen, M.J., Huang, K.C., Simorre, J.-P., Breukink, E., Den
1716 Blaauwen, T., Typas, A., Gross, C.A., Vollmer, W., 2015. Coordination of peptidoglycan
1717 synthesis and outer membrane constriction during Escherichia coli cell division. eLife 4,
1718 e07118. https://doi.org/10.7554/eLife.07118
1719 Gray, W.T., Govers, S.K., Xiang, Y., Parry, B.R., Campos, M., Kim, S., Jacobs-Wagner, C.,
1720 2019. Nucleoid Size Scaling and Intracellular Organization of Translation across
1721 Bacteria. Cell 177, 1632-1648.e20. https://doi.org/10.1016/j.cell.2019.05.017

1722 Guyer, M.S., Reed, R.R., Steitz, J.A., Low, K.B., 1981. Identification of a Sex-factor-affinity
1723 Site in E. coli as. Cold Spring Harb. Symp. Quant. Biol. 45, 135–140.
1724 https://doi.org/10.1101/SQB.1981.045.01.022
1725 Guzman, L.M., Belin, D., Carson, M.J., Beckwith, J., 1995. Tight regulation, modulation, and
1726 high-level expression by vectors containing the arabinose PBAD promoter. J. Bacteriol.
1727 177, 4121–4130. https://doi.org/10.1128/jb.177.14.4121-4130.1995
1728 Harju, J., Van Teeseling, M.C.F., Broedersz, C.P., 2024. Loop-extruders alter bacterial
1729 chromosome topology to direct entropic forces for segregation. Nat. Commun. 15, 4618.
1730 https://doi.org/10.1038/s41467-024-49039-w
1731 Harris, C.R., Millman, K.J., Van Der Walt, S.J., Gommers, R., Virtanen, P., Cournapeau, D.,
1732 Wieser, E., Taylor, J., Berg, S., Smith, N.J., Kern, R., Picus, M., Hoyer, S., Van
1733 Kerkwijk, M.H., Brett, M., Haldane, A., Del Río, J.F., Wiebe, M., Peterson, P., Gérard-
1734 Marchant, P., Sheppard, K., Reddy, T., Weckesser, W., Abbasi, H., Gohlke, C., Oliphant,
1735 T.E., 2020. Array programming with NumPy. Nature 585, 357–362.
1736 https://doi.org/10.1038/s41586-020-2649-2
1737 Hartmann, G., Honikel, K.O., Knüsel, F., Nüesch, J., 1967. The specific inhibition of the DNA-
1738 directed RNA synthesis by rifamycin. Biochim. Biophys. Acta BBA - Nucleic Acids
1739 Protein Synth. 145, 843–844. https://doi.org/10.1016/0005-2787(67)90147-5
1740 Hofmann, A., Mäkelä, J., Sherratt, D.J., Heermann, D., Murray, S.M., 2019. Self-organised
1741 segregation of bacterial chromosomal origins. eLife 8, e46564.
1742 https://doi.org/10.7554/eLife.46564
1743 Holmes, V.F., Cozzarelli, N.R., 2000. Closing the ring: Links between SMC proteins and
1744 chromosome partitioning, condensation, and supercoiling. Proc. Natl. Acad. Sci. 97,
1745 1322–1324. https://doi.org/10.1073/pnas.040576797
1746 Hsu, T.-M., Chang, Y.-R., 2019. High-Copy-Number Plasmid Segregation—Single-Molecule
1747 Dynamics in Single Cells. Biophys. J. 116, 772–780.
1748 https://doi.org/10.1016/j.bpj.2019.01.019
1749 Hu, X.-P., Dourado, H., Schubert, P., Lercher, M.J., 2020. The protein translation machinery is
1750 expressed for maximal efficiency in Escherichia coli. Nat. Commun. 11, 5260.
1751 https://doi.org/10.1038/s41467-020-18948-x
1752 Huggins, M.L., 1941. Solutions of Long Chain Compounds. J. Chem. Phys. 9, 440–440.
1753 https://doi.org/10.1063/1.1750930
1754 Hunter, J.D., 2007. Matplotlib: A 2D Graphics Environment. Comput. Sci. Eng. 9, 90–95.
1755 https://doi.org/10.1109/MCSE.2007.55
1756 Ireton, K., Gunther, N.W., Grossman, A.D., 1994. spo0J is required for normal chromosome
1757 segregation as well as the initiation of sporulation in Bacillus subtilis. J. Bacteriol. 176,
1758 5320–5329. https://doi.org/10.1128/jb.176.17.5320-5329.1994
1759 Iwai, N., Nagai, K., Wachi, M., 2002. Novel *S* -Benzylisothiourea Compound That Induces
1760 Spherical Cells in *Escherichia coli* Probably by Acting on a Rod-shape-determining
1761 Protein(s) Other Than Penicillin-binding Protein 2. Biosci. Biotechnol. Biochem. 66,
1762 2658–2662. https://doi.org/10.1271/bbb.66.2658
1763 Jacob, F., Brenner, S., Cuzin, F., 1963. On the Regulation of DNA Replication in Bacteria. Cold
1764 Spring Harb. Symp. Quant. Biol. 28, 329–348.
1765 https://doi.org/10.1101/SQB.1963.028.01.048
1766 Jakimowicz, D., Brzostek, A., Rumijowska-Galewicz, A., Żydek, P., Dołzbłasz, A., Smulczyk-
1767 Krawczyszyn, A., Zimniak, T., Wojtasz, Ł., Zawilak-Pawlik, A., Kois, A., Dziadek, J.,

1768 Zakrzewska-Czerwińska, J., 2007a. Characterization of the mycobacterial chromosome
1769 segregation protein ParB and identification of its target in Mycobacterium smegmatis.
1770 Microbiology 153, 4050–4060. https://doi.org/10.1099/mic.0.2007/011619-0
1771 Jakimowicz, D., Żydek, P., Kois, A., Zakrzewska-Czerwińska, J., Chater, K.F., 2007b.
1772 Alignment of multiple chromosomes along helical ParA scaffolding in sporulating
1773 *Streptomyces* hyphae. Mol. Microbiol. 65, 625–641. https://doi.org/10.1111/j.1365-
1774 2958.2007.05815.x
1775 Jalal, A.S.B., Le, T.B.K., 2020. Bacterial chromosome segregation by the ParABS system. Open
1776 Biol. 10, 200097. https://doi.org/10.1098/rsob.200097
1777 Jecz, P., Bartosik, A.A., Glabski, K., Jagura-Burdzy, G., 2015. A Single parS Sequence from the
1778 Cluster of Four Sites Closest to oriC Is Necessary and Sufficient for Proper Chromosome
1779 Segregation in Pseudomonas aeruginosa. PLOS ONE 10, e0120867.
1780 https://doi.org/10.1371/journal.pone.0120867
1781 Jensen, K.F., 1993. The Escherichia coli K-12 "wild types" W3110 and MG1655 have an rph
1782 frameshift mutation that leads to pyrimidine starvation due to low pyrE expression levels.
1783 J. Bacteriol. 175, 3401–3407. https://doi.org/10.1128/jb.175.11.3401-3407.1993
1784 Jun, S., Mulder, B., 2006. Entropy-driven spatial organization of highly confined polymers:
1785 Lessons for the bacterial chromosome. Proc. Natl. Acad. Sci. 103, 12388–12393.
1786 https://doi.org/10.1073/pnas.0605305103
1787 Jun, S., Wright, A., 2010. Entropy as the driver of chromosome segregation. Nat. Rev.
1788 Microbiol. 8, 600–607. https://doi.org/10.1038/nrmicro2391
1789 Kadoya, R., Baek, J.H., Sarker, A., Chattoraj, D.K., 2011. Participation of Chromosome
1790 Segregation Protein ParAI of *Vibrio cholerae* in Chromosome Replication. J. Bacteriol.
1791 193, 1504–1514. https://doi.org/10.1128/JB.01067-10
1792 Kaval, K.G., Chimalapati, S., Siegel, S.D., Garcia, N., Jaishankar, J., Dalia, A.B., Orth, K., 2023.
1793 Membrane-localized expression, production and assembly of Vibrio parahaemolyticus
1794 T3SS2 provides evidence for transertion. Nat. Commun. 14, 1178.
1795 https://doi.org/10.1038/s41467-023-36762-z
1796 Kawalek, A., Wawrzyniak, P., Bartosik, A.A., Jagura-Burdzy, G., 2020. Rules and Exceptions:
1797 The Role of Chromosomal ParB in DNA Segregation and Other Cellular Processes.
1798 Microorganisms 8, 105. https://doi.org/10.3390/microorganisms8010105
1799 Kim, H.-J., Calcutt, M.J., Schmidt, F.J., Chater, K.F., 2000. Partitioning of the Linear
1800 Chromosome during Sporulation of *Streptomyces coelicolor* A3(2) Involves an *oriC* -
1801 Linked *parAB* Locus. J. Bacteriol. 182, 1313–1320.
1802 https://doi.org/10.1128/JB.182.5.1313-1320.2000
1803 Kim, Seunghyeon, Wang, Y.-H., Hassan, A., Kim, Sangjin, 2024. Re-defining how mRNA
1804 degradation is coordinated with transcription and translation in bacteria.
1805 https://doi.org/10.1101/2024.04.18.588412
1806 Kjos, M., Veening, J.-W., 2014. Tracking of chromosome dynamics in live *S treptococcus*
1807 *pneumoniae* reveals that transcription promotes chromosome segregation: Transcription
1808 promotes chromosome segregation. Mol. Microbiol. 91, 1088–1105.
1809 https://doi.org/10.1111/mmi.12517
1810 Koch, A.L., Gross, G.H., 1979. Growth Conditions and Rifampin Susceptibility. Antimicrob.
1811 Agents Chemother. 15, 220–228. https://doi.org/10.1128/AAC.15.2.220

1812 Koleva, K.Z., Hellweger, F.L., 2015. From protein damage to cell aging to population fitness in
1813 E. coli: Insights from a multi-level agent-based model. Ecol. Model. 301, 62–71.
1814 https://doi.org/10.1016/j.ecolmodel.2015.01.024
1815 Kuwada, N.J., Cheveralls, K.C., Traxler, B., Wiggins, P.A., 2013. Mapping the driving forces of
1816 chromosome structure and segregation in Escherichia coli. Nucleic Acids Res. 41, 7370–
1817 7377. https://doi.org/10.1093/nar/gkt468
1818 Lagage, V., Boccard, F., Vallet-Gely, I., 2016. Regional Control of Chromosome Segregation in
1819 Pseudomonas aeruginosa. PLOS Genet. 12, e1006428.
1820 https://doi.org/10.1371/journal.pgen.1006428
1821 Łapińska, U., Glover, G., Capilla-Lasheras, P., Young, A.J., Pagliara, S., 2019. Bacterial ageing
1822 in the absence of external stressors. Philos. Trans. R. Soc. B Biol. Sci. 374, 20180442.
1823 https://doi.org/10.1098/rstb.2018.0442
1824 Lee, P.S., Grossman, A.D., 2006. The chromosome partitioning proteins Soj (ParA) and Spo0J
1825 (ParB) contribute to accurate chromosome partitioning, separation of replicated sister
1826 origins, and regulation of replication initiation in Bacillus subtilis. Mol. Microbiol. 60,
1827 853–869. https://doi.org/10.1111/j.1365-2958.2006.05140.x
1828 Lemon, K.P., Grossman, A.D., 2000. Movement of Replicating DNA through a Stationary
1829 Replisome. Mol. Cell 6, 1321–1330. https://doi.org/10.1016/S1097-2765(00)00130-1
1830 Lewis, P.J., Thaker, S.D., Errington, J., 2000. Compartmentalization of transcription and
1831 translation in Bacillus subtilis. EMBO J. 19, 710–718.
1832 https://doi.org/10.1093/emboj/19.4.710
1833 Lewis, R.A., Bignell, C.R., Zeng, W., Jones, A.C., Thomas, C.M., 2002. Chromosome loss from
1834 par mutants of Pseudomonas putida depends on growth medium and phase of growth.
1835 Microbiology 148, 537–548. https://doi.org/10.1099/00221287-148-2-537
1836 Li, H., 2019. Random Chromosome Partitioning in the Polyploid Bacterium *Thermus*
1837 *thermophilus* HB27. G3 GenesGenomesGenetics 9, 1249–1261.
1838 https://doi.org/10.1534/g3.119.400086
1839 Li, H., Angelov, A., Pham, V.T.T., Leis, B., Liebl, W., 2015. Characterization of chromosomal
1840 and megaplasmid partitioning loci in Thermus thermophilus HB27. BMC Genomics 16,
1841 317. https://doi.org/10.1186/s12864-015-1523-3
1842 Lim, H.C., Surovtsev, I.V., Beltran, B.G., Huang, F., Bewersdorf, J., Jacobs-Wagner, C., 2014.
1843 Evidence for a DNA-relay mechanism in ParABS-mediated chromosome segregation.
1844 eLife 3, e02758. https://doi.org/10.7554/eLife.02758
1845 Lin, W.-H., Jacobs-Wagner, C., 2022. Connecting single-cell ATP dynamics to overflow
1846 metabolism, cell growth, and the cell cycle in Escherichia coli. Curr. Biol. 32, 3911-
1847 3924.e4. https://doi.org/10.1016/j.cub.2022.07.035
1848 Lindner, A.B., Madden, R., Demarez, A., Stewart, E.J., Taddei, F., 2008. Asymmetric
1849 segregation of protein aggregates is associated with cellular aging and rejuvenation. Proc.
1850 Natl. Acad. Sci. 105, 3076–3081. https://doi.org/10.1073/pnas.0708931105
1851 Linnik, D., Maslov, I., Punter, C.M., Poolman, B., 2024. Dynamic structure of E. coli cytoplasm:
1852 supramolecular complexes and cell aging impact spatial distribution and mobility of
1853 proteins. Commun. Biol. 7, 508. https://doi.org/10.1038/s42003-024-06216-3
1854 Livny, J., Yamaichi, Y., Waldor, M.K., 2007. Distribution of Centromere-Like *parS* Sites in
1855 Bacteria: Insights from Comparative Genomics. J. Bacteriol. 189, 8693–8703.
1856 https://doi.org/10.1128/JB.01239-07

Mäkelä, J., Papagiannakis, A., Lin, W.-H., Lanz, M.C., Glenn, S., Swaffer, M., Marinov, G.K., Skotheim, J.M., Jacobs-Wagner, C., 2024. Genome concentration limits cell growth and modulates proteome composition in *Escherichia coli*. https://doi.org/10.1101/2024.02.26.582181

Mäkelä, J., Uphoff, S., Sherratt, D.J., 2021. Nonrandom segregation of sister chromosomes by *Escherichia coli* MukBEF. Proc. Natl. Acad. Sci. 118, e2022078118. https://doi.org/10.1073/pnas.2022078118

Mao, S., Chakraverti-Wuerthwein, M.S., Gaudio, H., Košmrlj, A., 2020. Designing the Morphology of Separated Phases in Multicomponent Liquid Mixtures. Phys. Rev. Lett. 125, 218003. https://doi.org/10.1103/PhysRevLett.125.218003

Mao, S., Kuldinow, D., Haataja, M.P., Košmrlj, A., 2019. Phase behavior and morphology of multicomponent liquid mixtures. Soft Matter 15, 1297–1311. https://doi.org/10.1039/C8SM02045K

Matsumoto, K., Hara, H., Fishov, I., Mileykovskaya, E., Norris, V., 2015. The membrane: transertion as an organizing principle in membrane heterogeneity. Front. Microbiol. 6. https://doi.org/10.3389/fmicb.2015.00572

McGuffee, S.R., Elcock, A.H., 2010. Diffusion, Crowding & Protein Stability in a Dynamic Molecular Model of the Bacterial Cytoplasm. PLoS Comput. Biol. 6, e1000694. https://doi.org/10.1371/journal.pcbi.1000694

McKinney, W., 2010. Data Structures for Statistical Computing in Python. Presented at the Python in Science Conference, Austin, Texas, pp. 56–61. https://doi.org/10.25080/Majora-92bf1922-00a

Miangolarra, A.M., Li, S.H.-J., Joanny, J.-F., Wingreen, N.S., Castellana, M., 2021. Steric interactions and out-of-equilibrium processes control the internal organization of bacteria. Proc. Natl. Acad. Sci. 118, e2106014118. https://doi.org/10.1073/pnas.2106014118

Minnen, A., Attaiech, L., Thon, M., Gruber, S., Veening, J.-W., 2011. SMC is recruited to oriC by ParB and promotes chromosome segregation in Streptococcus pneumoniae: Chromosome segregation in S. pneumoniae. Mol. Microbiol. 81, 676–688. https://doi.org/10.1111/j.1365-2958.2011.07722.x

Mohapatra, S., Weisshaar, J.C., 2018. Functional mapping of the *E. coli* translational machinery using single-molecule tracking. Mol. Microbiol. 110, 262–282. https://doi.org/10.1111/mmi.14103

Mohl, D.A., Gober, J.W., 1997. Cell Cycle–Dependent Polar Localization of Chromosome Partitioning Proteins in Caulobacter crescentus. Cell 88, 675–684. https://doi.org/10.1016/S0092-8674(00)81910-8

Molenaar, D., Van Berlo, R., De Ridder, D., Teusink, B., 2009. Shifts in growth strategies reflect tradeoffs in cellular economics. Mol. Syst. Biol. 5, 323. https://doi.org/10.1038/msb.2009.82

Mondal, J., Bratton, B.P., Li, Y., Yethiraj, A., Weisshaar, J.C., 2011. Entropy-Based Mechanism of Ribosome-Nucleoid Segregation in E. coli Cells. Biophys. J. 100, 2605–2613. https://doi.org/10.1016/j.bpj.2011.04.030

Nasehi Tehrani, J., McEwan, A., Jin, C., Van Schaik, A., 2012. L1 regularization method in electrical impedance tomography by using the L1-curve (Pareto frontier curve). Appl. Math. Model. 36, 1095–1105. https://doi.org/10.1016/j.apm.2011.07.055

Navarro, P.P., Vettiger, A., Ananda, V.Y., Llopis, P.M., Allolio, C., Bernhardt, T.G., Chao, L.H., 2022. Cell wall synthesis and remodelling dynamics determine division site architecture

and cell shape in Escherichia coli. Nat. Microbiol. 7, 1621–1634. https://doi.org/10.1038/s41564-022-01210-z

Otsu, N., 1979. A Threshold Selection Method from Gray-Level Histograms. IEEE Trans. Syst. Man Cybern. 9, 62–66. https://doi.org/10.1109/TSMC.1979.4310076

Paintdakhi, A., Parry, B., Campos, M., Irnov, I., Elf, J., Surovtsev, I., Jacobs-Wagner, C., 2016. Oufti: an integrated software package for high-accuracy, high-throughput quantitative microscopy analysis: Oufti: image analysis software. Mol. Microbiol. 99, 767–777. https://doi.org/10.1111/mmi.13264

Pande, S., Mitra, D., Chatterji, A., 2023. Entropy mediated organization of E.coli chromosome in fast growth conditions. https://doi.org/10.48550/ARXIV.2304.02275

Parry, B.R., Surovtsev, I.V., Cabeen, M.T., O'Hern, C.S., Dufresne, E.R., Jacobs-Wagner, C., 2014. The Bacterial Cytoplasm Has Glass-like Properties and Is Fluidized by Metabolic Activity. Cell 156, 183–194. https://doi.org/10.1016/j.cell.2013.11.028

Paszke, A., Gross, S., Massa, F., Lerer, A., Bradbury, J., Chanan, G., Killeen, T., Lin, Z., Gimelshein, N., Antiga, L., Desmaison, A., Köpf, A., Yang, E., DeVito, Z., Raison, M., Tejani, A., Chilamkurthy, S., Steiner, B., Fang, L., Bai, J., Chintala, S., 2019. PyTorch: An Imperative Style, High-Performance Deep Learning Library. https://doi.org/10.48550/ARXIV.1912.01703

Pedregosa, F., Varoquaux, G., Gramfort, A., Michel, V., Thirion, B., Grisel, O., Blondel, M., Müller, A., Nothman, J., Louppe, G., Prettenhofer, P., Weiss, R., Dubourg, V., Vanderplas, J., Passos, A., Cournapeau, D., Brucher, M., Perrot, M., Duchesnay, É., 2012. Scikit-learn: Machine Learning in Python. https://doi.org/10.48550/ARXIV.1201.0490

Pelletier, J., Halvorsen, K., Ha, B.-Y., Paparcone, R., Sandler, S.J., Woldringh, C.L., Wong, W.P., Jun, S., 2012. Physical manipulation of the *Escherichia coli* chromosome reveals its soft nature. Proc. Natl. Acad. Sci. 109. https://doi.org/10.1073/pnas.1208689109

Pettijohn, D.E., Hecht, R., 1974. RNA Molecules Bound to the Folded Bacterial Genome Stabilize DNA Folds and Segregate Domains of Supercoiling. Cold Spring Harb. Symp. Quant. Biol. 38, 31–41. https://doi.org/10.1101/SQB.1974.038.01.006

Pountain, A.W., Jiang, P., Yao, T., Homaee, E., Guan, Y., Podkowik, M., Shopsin, B., Torres, V.J., Golding, I., Yanai, I., 2022. Transcription-replication interactions reveal principles of bacterial genome regulation (preprint). Systems Biology. https://doi.org/10.1101/2022.10.22.513359

Proenca, A.M., Rang, C.U., Qiu, A., Shi, C., Chao, L., 2019. Cell aging preserves cellular immortality in the presence of lethal levels of damage. PLOS Biol. 17, e3000266. https://doi.org/10.1371/journal.pbio.3000266

Rabinovitch, A., Zaritsky, A., Feingold, M., 2003. DNA–membrane interactions can localize bacterial cell center. J. Theor. Biol. 225, 493–496. https://doi.org/10.1016/S0022-5193(03)00292-3

Reyes-Lamothe, R., Tran, T., Meas, D., Lee, L., Li, A.M., Sherratt, D.J., Tolmasky, M.E., 2014. High-copy bacterial plasmids diffuse in the nucleoid-free space, replicate stochastically and are randomly partitioned at cell division. Nucleic Acids Res. 42, 1042–1051. https://doi.org/10.1093/nar/gkt918

Sadhir, I., Murray, S.M., 2023. Mid-cell migration of the chromosomal terminus is coupled to origin segregation in Escherichia coli. Nat. Commun. 14, 7489. https://doi.org/10.1038/s41467-023-43351-7

Sanamrad, A., Persson, F., Lundius, E.G., Fange, D., Gynnå, A.H., Elf, J., 2014. Single-particle tracking reveals that free ribosomal subunits are not excluded from the *Escherichia coli* nucleoid. Proc. Natl. Acad. Sci. 111, 11413–11418. https://doi.org/10.1073/pnas.1411558111

Santi, I., McKinney, J.D., 2015. Chromosome Organization and Replisome Dynamics in Mycobacterium smegmatis. mBio 6, e01999-14. https://doi.org/10.1128/mBio.01999-14

Sawitzke, J.A., Austin, S., 2000. Suppression of chromosome segregation defects of *Escherichia coli muk* mutants by mutations in topoisomerase I. Proc. Natl. Acad. Sci. 97, 1671–1676. https://doi.org/10.1073/pnas.030528397

Schaechter, M., MaalOe, O., Kjeldgaard, N.O., 1958. Dependency on Medium and Temperature of Cell Size and Chemical Composition during Balanced Growth of Salmonella typhimurium. J. Gen. Microbiol. 19, 592–606. https://doi.org/10.1099/00221287-19-3-592

Scholz, S.A., Diao, R., Wolfe, M.B., Fivenson, E.M., Lin, X.N., Freddolino, P.L., 2019. High-Resolution Mapping of the Escherichia coli Chromosome Reveals Positions of High and Low Transcription. Cell Syst. 8, 212-225.e9. https://doi.org/10.1016/j.cels.2019.02.004

Scott, D.W., 1992. Multivariate Density Estimation: Theory, Practice, and Visualization, 1st ed, Wiley Series in Probability and Statistics. Wiley. https://doi.org/10.1002/9780470316849

Scott, M., Klumpp, S., Mateescu, E.M., Hwa, T., 2014. Emergence of robust growth laws from optimal regulation of ribosome synthesis. Mol. Syst. Biol. 10, 747. https://doi.org/10.15252/msb.20145379

Seabold, S., Perktold, J., 2010. Statsmodels: Econometric and Statistical Modeling with Python. Presented at the Python in Science Conference, Austin, Texas, pp. 92–96. https://doi.org/10.25080/Majora-92bf1922-011

Shis, D.L., Bennett, M.R., 2013. Library of synthetic transcriptional AND gates built with split T7 RNA polymerase mutants. Proc. Natl. Acad. Sci. 110, 5028–5033. https://doi.org/10.1073/pnas.1220157110

Si, F., Li, D., Cox, S.E., Sauls, J.T., Azizi, O., Sou, C., Schwartz, A.B., Erickstad, M.J., Jun, Y., Li, X., Jun, S., 2017. Invariance of Initiation Mass and Predictability of Cell Size in Escherichia coli. Curr. Biol. 27, 1278–1287. https://doi.org/10.1016/j.cub.2017.03.022

Silva, F., Lourenço, O., Pina-Vaz, C., Rodrigues, A.G., Queiroz, J.A., Domingues, F.C., 2010. The Use of DRAQ5 to Monitor Intracellular DNA in Escherichia coli by Flow Cytometry. J. Fluoresc. 20, 907–914. https://doi.org/10.1007/s10895-010-0636-y

Slayter, H., Kiho, Y., Hall, C.E., Rich, A., 1968. AN ELECTRON MICROSCOPIC STUDY OF LARGE BACTERIAL POLYRIBOSOMES. J. Cell Biol. 37, 583–590. https://doi.org/10.1083/jcb.37.2.583

Spahn, C., Endesfelder, U., Heilemann, M., 2014. Super-resolution imaging of Escherichia coli nucleoids reveals highly structured and asymmetric segregation during fast growth. J. Struct. Biol. 185, 243–249. https://doi.org/10.1016/j.jsb.2014.01.007

Spahn, C., Middlemiss, S., Gómez-de-Mariscal, E., Henriques, R., Bode, H.B., Holden, S., Heilemann, M., 2023. Transertion and cell geometry organize the *Escherichia coli* nucleoid during rapid growth. https://doi.org/10.1101/2023.10.16.562172

Spahn, C.K., Glaesmann, M., Grimm, J.B., Ayala, A.X., Lavis, L.D., Heilemann, M., 2018. A toolbox for multiplexed super-resolution imaging of the E. coli nucleoid and membrane using novel PAINT labels. Sci. Rep. 8, 14768. https://doi.org/10.1038/s41598-018-33052-3

Stracy, M., Lesterlin, C., Garza De Leon, F., Uphoff, S., Zawadzki, P., Kapanidis, A.N., 2015. Live-cell superresolution microscopy reveals the organization of RNA polymerase in the bacterial nucleoid. Proc. Natl. Acad. Sci. 112. https://doi.org/10.1073/pnas.1507592112

Stylianidou, S., Brennan, C., Nissen, S.B., Kuwada, N.J., Wiggins, P.A., 2016. *SuperSegger* : robust image segmentation, analysis and lineage tracking of bacterial cells. Mol. Microbiol. 102, 690–700. https://doi.org/10.1111/mmi.13486

Subach, O.M., Cranfill, P.J., Davidson, M.W., Verkhusha, V.V., 2011. An Enhanced Monomeric Blue Fluorescent Protein with the High Chemical Stability of the Chromophore. PLoS ONE 6, e28674. https://doi.org/10.1371/journal.pone.0028674

Subramanian, S., Murray, S.M., 2023. Subdiffusive movement of chromosomal loci in bacteria explained by DNA bridging. Phys. Rev. Res. 5, 023034. https://doi.org/10.1103/PhysRevResearch.5.023034

Takacs, C.N., Wachter, J., Xiang, Y., Ren, Z., Karaboja, X., Scott, M., Stoner, M.R., Irnov, I., Jannetty, N., Rosa, P.A., Wang, X., Jacobs-Wagner, C., 2022. Polyploidy, regular patterning of genome copies, and unusual control of DNA partitioning in the Lyme disease spirochete. Nat. Commun. 13, 7173. https://doi.org/10.1038/s41467-022-34876-4

Thappeta, Y., Cañas-Duarte, S.J., Kallem, T., Fragasso, A., Xiang, Y., Gray, W., Lee, C., Cegelski, L., Jacobs-Wagner, C., 2024. Glycogen phase separation drives macromolecular rearrangement and asymmetric division in *E. coli*. https://doi.org/10.1101/2024.04.19.590186

Tiruvadi-Krishnan, S., Männik, Jaana, Kar, P., Lin, J., Amir, A., Männik, Jaan, 2022. Coupling between DNA replication, segregation, and the onset of constriction in Escherichia coli. Cell Rep. 38, 110539. https://doi.org/10.1016/j.celrep.2022.110539

Tseng, H.-C., Harwell, C.L., Martin, C.H., Prather, K.L., 2010a. Biosynthesis of chiral 3-hydroxyvalerate from single propionate-unrelated carbon sources in metabolically engineered E. coli. Microb. Cell Factories 9, 96. https://doi.org/10.1186/1475-2859-9-96

Tseng, H.-C., Harwell, C.L., Martin, C.H., Prather, K.L., 2010b. Biosynthesis of chiral 3-hydroxyvalerate from single propionate-unrelated carbon sources in metabolically engineered E. coli. Microb. Cell Factories 9, 96. https://doi.org/10.1186/1475-2859-9-96

Van Der Walt, S., Schönberger, J.L., Nunez-Iglesias, J., Boulogne, F., Warner, J.D., Yager, N., Gouillart, E., Yu, T., 2014. scikit-image: image processing in Python. PeerJ 2, e453. https://doi.org/10.7717/peerj.453

Varricchio, F., Monier, R., 1971. Ribosome Patterns in *Escherichia coli* Growing at Various Rates. J. Bacteriol. 108, 105–110. https://doi.org/10.1128/jb.108.1.105-110.1971

Virtanen, P., Gommers, R., Oliphant, T.E., Haberland, M., Reddy, T., Cournapeau, D., Burovski, E., Peterson, P., Weckesser, W., Bright, J., Van Der Walt, S.J., Brett, M., Wilson, J., Millman, K.J., Mayorov, N., Nelson, A.R.J., Jones, E., Kern, R., Larson, E., Carey, C.J., Polat, İ., Feng, Y., Moore, E.W., VanderPlas, J., Laxalde, D., Perktold, J., Cimrman, R., Henriksen, I., Quintero, E.A., Harris, C.R., Archibald, A.M., Ribeiro, A.H., Pedregosa, F., Van Mulbregt, P., SciPy 1.0 Contributors, Vijaykumar, A., Bardelli, A.P., Rothberg, A., Hilboll, A., Kloeckner, A., Scopatz, A., Lee, A., Rokem, A., Woods, C.N., Fulton, C., Masson, C., Häggström, C., Fitzgerald, C., Nicholson, D.A., Hagen, D.R., Pasechnik, D.V., Olivetti, E., Martin, E., Wieser, E., Silva, F., Lenders, F., Wilhelm, F., Young, G., Price, G.A., Ingold, G.-L., Allen, G.E., Lee, G.R., Audren, H., Probst, I., Dietrich, J.P., Silterra, J., Webber, J.T., Slavič, J., Nothman, J., Buchner, J., Kulick, J., Schönberger, J.L., De Miranda Cardoso, J.V., Reimer, J., Harrington, J., Rodríguez, J.L.C., Nunez-

Iglesias, J., Kuczynski, J., Tritz, K., Thoma, M., Newville, M., Kümmerer, M., Bolingbroke, M., Tartre, M., Pak, M., Smith, N.J., Nowaczyk, N., Shebanov, N., Pavlyk, O., Brodtkorb, P.A., Lee, P., McGibbon, R.T., Feldbauer, R., Lewis, S., Tygier, S., Sievert, S., Vigna, S., Peterson, S., More, S., Pudlik, T., Oshima, T., Pingel, T.J., Robitaille, T.P., Spura, T., Jones, T.R., Cera, T., Leslie, T., Zito, T., Krauss, T., Upadhyay, U., Halchenko, Y.O., Vázquez-Baeza, Y., 2020. SciPy 1.0: fundamental algorithms for scientific computing in Python. Nat. Methods 17, 261–272. https://doi.org/10.1038/s41592-019-0686-2

Wang, P., Robert, L., Pelletier, J., Dang, W.L., Taddei, F., Wright, A., Jun, S., 2010. Robust Growth of Escherichia coli. Curr. Biol. 20, 1099–1103. https://doi.org/10.1016/j.cub.2010.04.045

Wang, X., Liu, X., Possoz, C., Sherratt, D.J., 2006. The two *Escherichia coli* chromosome arms locate to separate cell halves. Genes Dev. 20, 1727–1731. https://doi.org/10.1101/gad.388406

Waskom, M., 2021. seaborn: statistical data visualization. J. Open Source Softw. 6, 3021. https://doi.org/10.21105/joss.03021

Weitao, T., Nordstrom, K., Dasgupta, S., 1999. Mutual suppression of mukB and seqA phenotypes might arise from their opposing influences on the Escherichia coli nucleoid structure. Mol. Microbiol. 34, 157–168. https://doi.org/10.1046/j.1365-2958.1999.01589.x

White, S., Quinn, J., Enzor, J., Staats, J., Mosier, S.M., Almarode, J., Denny, T.N., Weinhold, K.J., Ferrari, G., Chan, C., 2021. FlowKit: A Python Toolkit for Integrated Manual and Automated Cytometry Analysis Workflows. Front. Immunol. 12, 768541. https://doi.org/10.3389/fimmu.2021.768541

Wientjes, F.B., Nanninga, N., 1989. Rate and topography of peptidoglycan synthesis during cell division in Escherichia coli: concept of a leading edge. J. Bacteriol. 171, 3412–3419. https://doi.org/10.1128/jb.171.6.3412-3419.1989

Wiktor, J., Gynnå, A.H., Leroy, P., Larsson, J., Coceano, G., Testa, I., Elf, J., 2021. RecA finds homologous DNA by reduced dimensionality search. Nature 597, 426–429. https://doi.org/10.1038/s41586-021-03877-6

Woldringh, C.L., 2002. The role of co-transcriptional translation and protein translocation (transertion) in bacterial chromosome segregation. Mol. Microbiol. 45, 17–29. https://doi.org/10.1046/j.1365-2958.2002.02993.x

Woldringh, C.L., Huls, P., Pas, E., Brakenhoff, G.J., Nanninga, N., 1987. Topography of Peptidoglycan Synthesis during Elongation and Polar Cap Formation in a Cell Division Mutant of Escherichia coli MC4100. Microbiology 133, 575–586. https://doi.org/10.1099/00221287-133-3-575

Wu, F., Japaridze, A., Zheng, X., Wiktor, J., Kerssemakers, J.W.J., Dekker, C., 2019a. Direct imaging of the circular chromosome in a live bacterium. Nat. Commun. 10, 2194. https://doi.org/10.1038/s41467-019-10221-0

Wu, F., Swain, P., Kuijpers, L., Zheng, X., Felter, K., Guurink, M., Solari, J., Jun, S., Shimizu, T.S., Chaudhuri, D., Mulder, B., Dekker, C., 2019b. Cell Boundary Confinement Sets the Size and Position of the E. coli Chromosome. Curr. Biol. 29, 2131-2144.e4. https://doi.org/10.1016/j.cub.2019.05.015

2085 Wu, L.J., Lee, S., Park, S., Eland, L.E., Wipat, A., Holden, S., Errington, J., 2020. Geometric
2086 principles underlying the proliferation of a model cell system. Nat. Commun. 11, 4149.
2087 https://doi.org/10.1038/s41467-020-17988-7
2088 Xiang, Y., Surovtsev, I.V., Chang, Y., Govers, S.K., Parry, B.R., Liu, J., Jacobs-Wagner, C.,
2089 2021. Interconnecting solvent quality, transcription, and chromosome folding in
2090 Escherichia coli. Cell 184, 3626-3642.e14. https://doi.org/10.1016/j.cell.2021.05.037
2091 Yamaichi, Y., Fogel, M.A., McLeod, S.M., Hui, M.P., Waldor, M.K., 2007. Distinct
2092 Centromere-Like *parS* Sites on the Two Chromosomes of *Vibrio* spp. J. Bacteriol. 189,
2093 5314–5324. https://doi.org/10.1128/JB.00416-07
2094 Yang, D., Männik, Jaana, Retterer, S.T., Männik, Jaan, 2020. The effects of polydisperse
2095 crowders on the compaction of the *Escherichia coli* nucleoid. Mol. Microbiol. 113, 1022–
2096 1037. https://doi.org/10.1111/mmi.14467
2097 Yao, S., Helinski, D.R., Toukdarian, A., 2007. Localization of the Naturally Occurring Plasmid
2098 ColE1 at the Cell Pole. J. Bacteriol. 189, 1946–1953. https://doi.org/10.1128/JB.01451-
2099 06
2100 Youngren, B., Nielsen, H.J., Jun, S., Austin, S., 2014. The multifork *Escherichia coli*
2101 chromosome is a self-duplicating and self-segregating thermodynamic ring polymer.
2102 Genes Dev. 28, 71–84. https://doi.org/10.1101/gad.231050.113
2103 Yu, W., Herbert, S., Graumann, P.L., Götz, F., 2010. Contribution of SMC (Structural
2104 Maintenance of Chromosomes) and SpoIIIE to Chromosome Segregation in
2105 Staphylococci. J. Bacteriol. 192, 4067–4073. https://doi.org/10.1128/JB.00010-10
2106 Zhang, C., Shao, P.G., Van Kan, J.A., Van Der Maarel, J.R.C., 2009. Macromolecular crowding
2107 induced elongation and compaction of single DNA molecules confined in a nanochannel.
2108 Proc. Natl. Acad. Sci. 106, 16651–16656. https://doi.org/10.1073/pnas.0904741106
2109 Zhou, Z., Siddiquee, M.M.R., Tajbakhsh, N., Liang, J., 2020. UNet++: Redesigning Skip
2110 Connections to Exploit Multiscale Features in Image Segmentation. IEEE Trans. Med.
2111 Imaging 39, 1856–1867. https://doi.org/10.1109/TMI.2019.2959609
2112 Zimmerman, S.B., Trach, S.O., 1991. Estimation of macromolecule concentrations and excluded
2113 volume effects for the cytoplasm of Escherichia coli. J. Mol. Biol. 222, 599–620.
2114 https://doi.org/10.1016/0022-2836(91)90499-V
2115
2116
2117 **FIGURE LEGENDS**
2118 **Figure 1: Correlations between polysome and nucleoid dynamics at the single-cell level.** CJW7323
2119 cells were grown in M9gluCAAT in a microfluidic device**. A.** Schematic illustrating observable nucleoid
2120 segregation events. **B.** Fluorescence images of RplA-GFP and HupA-mCherry for a representative cell
2121 (CJW7323) from birth to division. **C.** Ensemble kymographs of the average RplA-GFP and HupA-mCherry
2122 fluorescence during the cell division cycle (>300,000 segmented cell instances from 4122 complete cell
2123 division cycles). The average relative timing of cell constriction initiation was estimated as shown in Figure
2124 1 – figure supplement 2. **D.** Two-dimensional projections of the average RplA-GFP and HupA-mCherry
2125 fluorescence signals in predivisional cells (4564 cells with two nucleoid objects, from 1907 cell division
2126 cycles, 95-100% into the cell division cycle) and their intensity profiles. White arrows indicate RplA-GFP
2127 enrichments at the quarter cell positions, while the black arrow indicates the site of cell constriction. **E.** Plot

2128 showing the dynamics of RplA-GFP accumulation and HupA-mCherry depletion at mid-nucleoid (median ±
2129 IQR) during the nucleoid cycle (see Figure 1 – Figure supplement 2D). Data from 3240 nucleoid segregation
2130 cycles are shown (40 nucleoid cycle bins, 2512-4823 segmented nucleoids per bin). **F.** Correlation
2131 (Spearman ρ = -0.52, p-value < 10^{-10}) between the rate of RplA-GFP accumulation in the middle of the
2132 nucleoid ($\frac{\Delta RplA_{mid-nuc}\ conc.}{\Delta T}$) and the rate of HupA-mCherry depletion in the same region ($\frac{\Delta HupA_{mid-nuc}\ conc.}{\Delta T}$)
2133 between the initiation of nucleoid splitting and just before the end of nucleoid splitting (3214 complete
2134 nucleoid cycles). The colormap indicates the Gaussian kernel density estimation (KDE). Solid black line
2135 indicates the linear-regression fit to the data. **G.** Percentage of cells that continue to accumulate polysomes
2136 in the middle of the cell ($\frac{\Delta RplA_{mid-cell}\ conc.}{\Delta T}$) during four relative time bins (1335 to 1957 cell division cycles
2137 per bin) covering the period from the end of nucleoid splitting until cell division. **H.** Correlation (Spearman
2138 ρ = 0.47, p-value < 10^{-10}) between the rate of RplA-GFP accumulation at mid-cell ($\frac{\Delta RplA_{mid-cell}\ conc.}{\Delta T}$) and the
2139 rate of distance increase between the sister nucleoids ($\frac{\Delta Distance_{nuc}}{\Delta T}$) during the first quartile (0-25%) of the
2140 period between the end of nucleoid splitting and cell division (1376 cell division cycles). The black markers
2141 correspond to nine bins (mean ± SEM, 75 to 177 cell division cycles per bin) within the 5th-95th percentiles
2142 of *x*-axis range. Also shown is the distribution of the cell elongation rates ($\frac{\Delta Length_{cell}}{\Delta T}$) during the same time
2143 interval, with the mean and SD shown by the solid and dashed lines, respectively. **I.** Plot showing the
2144 coefficients of a linear mixed-effects model (see eq. 3 in Methods and Figure 1 – figure supplement 3B) for
2145 four interval bins between the completion of nucleoid splitting and cell division. The coefficients quantify the
2146 relative contribution of polysome accumulation at mid-cell ($\frac{\Delta RplA_{mid-cell}\ conc.}{\Delta T}$) and cell elongation ($\frac{\Delta Length_{cell}}{\Delta T}$)
2147 to the rate of sister nucleoid migration ($\frac{\Delta Distance_{nuc}}{\Delta T}$). All coefficients are significant (Prob(<|Z|) < 10^{-9}), except
2148 for the one marked with an asterisk that is marginally significant (Prob(<|Z|) = 0.02).
2149
2150 **Figure 2: Correlation of the extent and relative timing of polysome accumulation with nucleoid**
2151 **segregation at the population level. A.** RplA-mEos2 and DAPI (scaled by the whole cell average)
2152 demographs constructed from snapshots of DAPI-stained CJW6768 cells (815 to 2771 cells per
2153 demograph) expressing RplA-mEos2 and growing in different nutrient conditions (see Table S1 for
2154 abbreviations). The demographs were arranged from smallest (M9mann, top) to biggest average cell area
2155 (M9malaCAAT, bottom). Additional demographs for different ribosomal reporters and nutrient conditions
2156 are shown in Figure 2 – figure supplement 1. **B.** Correlation between average polysome accumulation and
2157 average nucleoid depletion at mid-cell for all tested strains (Spearman ρ_{all} = -0.85, p-value < 10^{-10}) with
2158 different ribosomal and nucleoid reporters, and within each strain (-0.75 < Spearman ρ_{strain} < -0.95, p-values
2159 < 10^{-3}) across nutrient conditions. A linear regression was fitted to all the data.
2160
2161 **Figure 3: Correlations between polysome and nucleoid asymmetries. A.** Distributions of RplA-GFP
2162 concentration in the new (grey) and the old (black) pole regions of newborn cells (0-2.5% of the cell division

2163 cycle, n = 912 cell division cycles). The histograms were smoothed using Gaussian kernel density
2164 estimations. **B.** Correlation (Spearman ρ = -0.41, p-value < 10^{-10}) between the polar polysome asymmetry
2165 and the position of the nucleoid centroid around the cell center of cells at the beginning of the division cycle
2166 (0-10%, n = 1179 cell division cycles). The contour plot consists of 9 levels with a lower data density
2167 threshold of 25%. The polar polysome profile for cells with correlations indicated by the numbers 1 and 2
2168 are schematically illustrated in the next panel. A linear regression (solid grey line) was fitted to the data. **C.**
2169 Schematic illustrating the effects of the relative polysome abundance between the poles on the position of
2170 the nucleoid. **D.** Average 2D projections of the RplA-GFP and HupA-mCherry concentration (conc.) at
2171 different cell division cycle intervals (~9440 to 47240 cell images per cell division cycle interval from 4122
2172 cell division cycles). The dotted line indicates the boundary between two cell division cycles. **E.** Density plot
2173 comparing the distribution of the HupA-mCherry maximum concentration toward the new pole (gray) to that
2174 toward the old pole (black) in newborn cells (0-2.5% of the division cycle, n = 912 cell division cycles). The
2175 histograms were smoothed using Gaussian kernel density estimations. **F.** Correlation (Spearman ρ = 0.52,
2176 p-value<10^{-10}) between the nucleoid density asymmetry and the relative availability of polysome-free space
2177 between the two cell halves early in the cell division cycle (0-10% of the division cycle, n = 2150 cell division
2178 cycles). The contour plot consists of 9 levels with a lower data density threshold of 25%. Values above 1
2179 on the *x*-axis indicate more polysome-free space toward the new pole, and values below 1 correspond to
2180 cells with more polysome-free space toward the old pole. On the *y*-axis, values above 1 indicate higher
2181 DNA density toward the new pole and values below 1 indicate higher DNA density toward the old pole. **G.**
2182 Average 2D projections of newborn cells (0-10% into the cell division cycle) from the lower-left quartile in
2183 panel C (region 2, n = 223 cell division cycles) and the upper right quartile in panel C (region 1, n = 557 cell
2184 division cycles) and their 1D intensity profiles.
2185
2186 **Figure 4: Simulation results of the reaction-diffusion model for different growth rates or nucleoid**
2187 **diffusion rates. A.** Simulation of a non-growing virtual cell, initialized with homogeneous polysome
2188 concentration and a nucleoid spread between the two poles (t = 0 s). It reaches steady state with the
2189 nucleoid compacted at mid-cell at t = 998 s. **B.** 1D simulation of polysome (blue) and nucleoid (red)
2190 dynamics during slow growth (growth rate = 0.25 h^{-1}, D_n = 0.001 μm^2/s, cell length at birth = 2.2 μm) at
2191 different relative cell division cycle timepoints. The simulation was initialized from the equilibrium polysome
2192 and nucleoid distribution (at 0%). **C.** Schematic summarizing how polysomes accumulate in the middle of
2193 the elongating nucleoid, causing nucleoid splitting. **D.** Correlation between the relative timing of nucleoid
2194 splitting and the growth rate as captured by our reaction-diffusion model (D_n = 0.001 μm^2/sec) across six
2195 growth rate bins. The cell and nucleoid lengths for each growth rate bin matched previously published data
2196 (Govers et al., 2024). **E.** Deviation between the steady state after infinite relaxation time (dashed curves)
2197 and the polysome or nucleoid profiles in newborn cells after one simulation round (solid curves) for
2198 increasing nucleoid diffusion constants. The simulations were performed for a growth rate of 0.57 h^{-1}, which
2199 is comparable to the average growth rate in our microfluidic experiments (Figure 2 – figure supplement 2A).

2200

2201 **Figure 5: Comparison of the nonequilibrium polysome accumulation with freely diffusing particles.**
2202 **A.** Phase contrast and fluorescence (fluor.) images of two representative single cells (CJW7651). The red
2203 circles indicate the position of the mCherry-μNS particle in each cell. **B.** Two-dimensional average cell
2204 projections of the DAPI concentration (conc.) and the RplA-msfGFP concentration, and 2D histogram of
2205 the mCherry-μNS particle density for four cell length bins of CJW7651 cells (~2580 cells per bin) grown in
2206 M9gluCAAT and spotted on an agarose pad containing the same medium. Since the cell pole identity
2207 cannot be inferred from snapshot images, pole assignment was random. **C.** Average 1D profiles of the
2208 scaled DAPI and RplA-msfGFP concentrations and the mCherry-μNS probability density.

2209

2210 **Figure 6: Effects of rifampicin treatment and polysome depletion on nucleoid segregation and**
2211 **compaction. A.** Plot showing the average instantaneous growth rate (mean ± SD shown by the solid black
2212 curve and grey shaded region, respectively) of a cell population (n = 2629 cell division cycles) undergoing
2213 two rounds of rifampicin treatment in a microfluidic device supplemented with M9gluCAAT. The distribution
2214 of the average cell cycle growth rate of unperturbed populations is also shown on the right (n = 4122 cell
2215 division cycles from a different microfluidics experiment). The solid horizontal line indicates the average
2216 growth rate. **B.** Plot showing the average distance between nucleoid peaks for a population of cells
2217 (squares, 114 cell division cycles) that were born (-112 to -102 min) and divided before the addition of
2218 rifampicin, and for a population of cells (circles, 112 cell division cycles) that were born just before (-22 to -
2219 12 min) and divided after the addition of rifampicin. A third-degree polynomial was fitted to the data from
2220 the unperturbed population (solid blue curve) and juxtaposed (dashed blue curve) with the data from the
2221 interrupted population. **C.** Average 1D profile and 2D projections of the scaled (divided by the whole cell
2222 average concentration) RplA-GFP and HupA-mCherry signals for cells before and after rifampicin addition
2223 (n = 112 cell division cycles). The red dashed horizontal lines in the 1D intensity profiles and the white
2224 crosses in the 2D profiles mark the nucleoid peaks. **D.** Plot showing the RplA-GFP accumulation relative to
2225 the HupA-mCherry depletion at mid-cell from 0 to 24 min after birth (colormap) for cells that completed their
2226 division cycle before the addition of rifampicin (n = 114 cell division cycles) and for cells that were subjected
2227 to rifampicin 12 min (n = 112 cell division cycles) or 3 min (n = 99 cell division cycles) after birth. **E.** Average
2228 1D and 2D scaled RplA-GFP and HupA-mCherry intensity profiles for newborn cells (0 to 10 min after birth)
2229 before (left, n = 726 cell division cycles), just after (middle, n = 367 cell division cycles), and much after
2230 (right, n = 235 cell division cycles) rifampicin addition.

2231

2232 **Figure 7: Effects of ectopic polysome accumulation on nucleoid dynamics. A.** Schematic
2233 summarizing the experiment. **B.** Representative phase contrast and mTagBFP2 fluorescence images at
2234 different times after induction with IPTG (100 μM) are shown, next to a plot showing the mTagBFP2
2235 fluorescence of the entire population (mean ± SD, n = 3624 cell trajectories) over time. **C.** Plot showing how
2236 instantaneous growth rate (mean ±SD, n = 3624 mTagBFP2 induction trajectories) decreases following

2237 induction of mTagBFP2 synthesis. **D-F.** Representative kymographs and images of the normalized (divided
2238 by the whole cell average) RplA-msfGFP and HupA-mCherry fluorescence signals in cells (CJW7798) born
2239 during mTagBFP2 over-expression. **F.** Phase contrast images are shown to illustrate the formation of
2240 inclusion bodies (see also Figure 6 – figure supplement 1). Additional cell examples are shown in Movie
2241 S5.
2242
2243 **Figure 8: Effects of cell width increase on polysome and nucleoid dynamics. A.** Comparison of the
2244 cell width increase during cell growth between CJW7323 cells treated with cephalexin (mean ± SD, 360 cell
2245 growth trajectories, 418 to 1511 segmented cells per bin) and cells treated with both cephalexin (50 µg/mL)
2246 and A22 (4 µg/mL) (grey, mean ± SD, 309 cell growth trajectories, 51 to 1684 segmented cells per bin).
2247 The same cell area bins are compared between the two populations. **B.** Phase contrast and fluorescence
2248 images of a representative cephalexin-treated cell expressing RplA-GFP and HupA-mCherry. **C.** Same as
2249 B but for a short cell growing in the presence of A22 and cephalexin. **D.** Same as C but for a longer cell.
2250 The white arrowheads indicate the polysome bridges that connect polysome accumulations between two
2251 DNA-free regions. Additional examples are shown in Movie S6 **E.** Representative fluorescence images of
2252 RplA-GFP and HupA-mCherry in a cell treated with A22 and cephalexin. The dotted lines indicate the
2253 representative cross-like polysome accumulation, which forms during the fusion of the polysome
2254 accumulation towards the center (see also Movie S6). **F.** Comparison of the segmented polysome
2255 accumulations and nucleoid objects between A22+cephalexin (150 sampled segmented cells from 47
2256 growth trajectories) and cephalexin-treated (150 sampled segmented cells from 100 growth trajectories)
2257 cells. The polysome and nucleoid areas per cell were normalized by the population-average statistic from
2258 cephalexin-treated cells. All differences between the two populations are statistically significant (Mann-
2259 Whitney p-value < 10^{-10}).
2260
2261 **SUPPLEMENTARY FIGURE LEGENDS**
2262 **Figure 1 – figure supplement 1: Reproducibility analysis of the dynamic ribosome and nucleoid**
2263 **distributions between microfluidic experiments.** While phase-contrast images were acquired every
2264 minute in all microfluidics experiments, two different intervals (1 min and 3 min) were used for fluorescence
2265 image acquisition. **A.** Kymographs showing the RplA-GFP and HupA-mCherry concentration in CJW7323
2266 cells growing in microfluidic channels in M9gluCAAT. Cell and nucleoid contours are shown in each channel
2267 using a different color for each cell lineage (from dark purple to bright orange). **B-E.** Two biological replicate
2268 experiments were performed for this strain and nutrient condition using different intervals of fluorescence
2269 image acquisition (1 or 3 min). **B.** Plots showing that the instantaneous and average division cycle growth
2270 rates were nearly identical between the two experiments. **C.** Plots showing the distributions of the indicated
2271 fluorescence signals for the 1-min acquisition interval (black) compared to the 3-min frame rate interval
2272 (orange) before and after correction. The difference in the excitation power between the two experiments
2273 was 50% (240 %ms vs. 360 %ms), which was also reflected in the ratio of their average fluorescence values

2274 (1.4 for RplA-GFP and 1.6 for HupA-mCherry). The fluorescence values from the 1-min interval experiment
2275 were corrected by multiplying by these ratios, resulting in a near-perfect overlap between fluorescence
2276 distributions after correction. **D.** Plots showing that the scaled (z-score) RplA-GFP and HupA-mCherry
2277 intensity profiles from birth to division were almost identical between the two experiments. The intensity
2278 profiles are shown for 10 cell division cycle intervals (1489 and 2633 cell division cycles for the 1-min and
2279 3-min interval experiments, respectively). The z-score was calculated for each segmented cell by
2280 subtracting the whole cell average fluorescence and then dividing the difference by the standard deviation.
2281 Each intensity profile corresponds to the average z-score of all segmented cell instances within the
2282 corresponding cell cycle interval. **E.** Plot showing that the average RplA-GFP concentration from birth to
2283 division (averages ± SD across 20 cell division cycle bins) remained constant and was virtually identical
2284 between the two experiments.
2285
2286 **Figure 1 – figure supplement 2: Determination of the relative timing of cell constriction.** The average
2287 cell width at mid-cell was used to estimate the relative timing of cell constriction from birth (0%) to division
2288 (100%). Considering the variability in the constriction onset across single cells, the average timing
2289 corresponds to the elbow of the curve, or the point with the maximum distance from the linear segment that
2290 connects the ends of the cell width curve, also known as the chord.
2291
2292 **Figure 1 – figure supplement 3: Intracellular distributions of RplA-GFP in rifampicin-treated cells**
2293 **following rifampicin removal. A.** Representative image of RplA-GFP fluorescence in cells (CJW7323)
2294 treated with rifampicin (100 µg/mL). The cells were treated for 45 min, washed, and spotted on an
2295 M9gluCAAT agarose pad without antibiotic. The presented snapshot corresponds to the first timepoint
2296 immediately after cell spotting showing diffuse distribution of RplA-GFP signal. **B.** Time-lapse fluorescence
2297 (fluor.) images showing the emergence of RplA-GFP signal accumulation at mid-cell (single arrow) or
2298 quarter cell positions (double arrows) during recovery from rifampicin treatment (same experiment as in
2299 panel A).
2300
2301 **Figure 1 – figure supplement 4: Tracking nucleoid segregation cycles.** Since the timing of nucleoid
2302 segregation varied between cell division cycles, the nucleoid segregation cycles were tracked
2303 independently of the cell division cycles for each cell lineage to measure the relative timing of RplA-GFP
2304 accumulation and HupA-mCherry depletion in the middle of the nucleoid (as shown in Figure 1E). **A.** Plots
2305 showing the frequency of cells with one, two, three, or four detected nucleoid objects across 10 cell division
2306 cycle bins from birth (top) to division (bottom). Data from 4122 cell division cycles are shown. **B.** The polarity
2307 of the cells (+/-) and the relative position of the nucleoid mask (toward the new or old pole) was used to
2308 track the nucleoid segregation cycle. This strategy was used to identify four groups of nucleoid segregation
2309 cycles (group -2, -1, 1 and 2). Group -2 includes nucleoids that were “born” toward the old cell pole in a
2310 mother cell with negative (-) polarity and were inherited at the center of a daughter cell with a negative

2311 polarity. Group -1 includes nucleoids that were "born" toward the new cell pole in a mother cell with negative
2312 (-) polarity and were inherited at the center of a daughter cell with a positive (+) polarity. Group 1 includes
2313 nucleoids that were "born" toward the new cell pole in a mother cell with positive (+) polarity and were
2314 inherited at the center of a daughter cell with negative (-) polarity. Group 2 includes nucleoids that were
2315 "born" toward the old cell pole in a mother cell with positive (+) polarity and were inherited at the center of
2316 a daughter cell with positive (+) polarity. **C.** Plots showing the distributions of nucleoid positions around the
2317 cell center for 10 nucleoid segregation cycle bins, from the time a nucleoid was "born" (top) until it split
2318 (bottom). These plots show the inheritance of the nucleoids from the quarter cell positions of the mother
2319 cells to the middle of their daughters for the four groups of nucleoid segregation cycles. The solid gray line
2320 represents the average density of the nucleoid positions for all four groups. Data from 2286 complete
2321 nucleoid cycles are shown. **D.** Schematic that explains the definition of a nucleoid cycle. The nucleoid cycle
2322 ranges from the end of a nucleoid splitting event, until the next splitting of the sister nucleoids. It usually
2323 extends beyond cell division, into the next cell division cycle.
2324
2325 **Figure 1 – figure supplement 5: Correlations used to calculate the relative contribution of polysome**
2326 **accumulation and cell elongation to nucleoid migration. A.** Correlation (Spearman ρ = 0.47, p-value <
2327 10^{-10}) between the rate of RplA-GFP accumulation at mid-cell ($\frac{\Delta RplA_{mid-cell}\ conc.}{\Delta T}$) and the rate of distance
2328 increase between the sister nucleoids minus the rate of cell elongation ($\frac{\Delta Distance_{nuc}}{\Delta T} - \frac{\Delta Length_{cell}}{\Delta T}$) across
2329 cells. The colormap corresponds to a Gaussian kernel density estimation. Binned data are also shown
2330 (mean ± SEM, 75 to 177 cell division cycles per bin, 9 bins in total) within the 5th-95th percentiles of the *x*-
2331 axis range. **B.** Scaled correlations (z-scores) between $\frac{\Delta RplA_{mid-cell}\ conc.}{\Delta T}$ (blue) or $\frac{\Delta Length_{cell}}{\Delta T}$ (grey) and
2332 $\frac{\Delta Distance_{nuc}}{\Delta T}$ (y-axis) during four relative time bins (1335 to 1957 cell division cycles per bin) covering the
2333 period from the end of nucleoid splitting until cell division. Shown are the Spearman correlations (ρ), all with
2334 a p-value below 10^{-6}, except for the one marked with an asterisk (p-value = 0.02).
2335
2336 **Figure 1 – figure supplement 6: Examination of the relative timing of the initiation of nucleoid**
2337 **constriction and the accumulation of polysomes at mid-nucleoid. A.** RplA-GFP and HupA-mCherry
2338 concentration (fluorescence arbitrary units) images of four representative single cells (CJW7323) growing
2339 in M9glyT and their fluorescence intensity profiles along the cell length. **B.** Demographs of the scaled RplA-
2340 GFP and HupA-mCherry concentration from 13554 *E. coli* cells grown in M9glyT. **C.** Average 1D intensity
2341 profiles of the scaled (divided by the whole cell average) RplA-GFP and HupA-mCherry concentration for
2342 12 bins of cells lengths (>1100 cells per intensity profile). **D.** Plot showing the scaled RplA-GFP and HupA-
2343 mCherry concentration in the middle of the cells for increasing cell length (~370 cells per bin, 25 bins). Cells
2344 longer than 3 μm were excluded to avoid the effects of cell constriction. The arrow and vertical dashed line
2345 indicate the minimum cell length bin with an apparent HupA-mCherry depletion at mid-cell, marking the
2346 initiation of nucleoid splitting. The error bars indicate mean ± standard error of the mean (SEM).

2347

2348 **Figure 2 – figure supplement 1: Demographs of scaled ribosome and nucleoid fluorescence for**
2349 **strains with different ribosome markers and under various nutrient conditions.** Demographs are
2350 ordered according to increasing average cell area, which scales with growth rate (Schaechter et al., 1958),
2351 from left to right and top to bottom. These demographs were constructed from snapshots of the following
2352 strains: **A.** CJW6768 (RplA-mEos2 ribosomal marker, 747 to 2446 cells per condition), **B.** CJW6769 (RpsB-
2353 mEos2 ribosomal marker, 690 to 3169 cells per condition), **C.** CJW7020 (RplA-msfGFP ribosomal marker,
2354 657 to 2432 cells per condition) and **D.** CJW7021 (RpsB-msfGFP ribosomal marker, 788 to 1950 cells per
2355 condition), using the cell length as a proxy for the cell division cycle, with the signal intensity profile sorted
2356 from the shortest newborn cells to the longest predivisional cells. Note that the demographs for the
2357 CJW6768 strain (panel A) in the nutrient conditions M9mann, M9mala, M9malt, M9mannCAAT,
2358 M9glyCAAT and M9malaCAAT are not shown here, as they are presented in Figure 2A. The nutrient
2359 abbreviations and compositions are explained in Table S1.
2360

2361 **Figure 2 – figure supplement 2: Correlation of the extent and relative timing of polysome**
2362 **accumulation with nucleoid segregation at the single-cell level. A.** Plot showing the variability in growth
2363 rate (GR) across cell division cycles for cells growing in microfluidics in M9gluCAAT (4114 cell division
2364 cycles, 9 growth rate bins with 93 to 860 cell division cycles each). **B.** Ensemble kymographs of the RplA-
2365 GFP and HupA-mCherry concentration normalized by the average fluorescence for the slowest,
2366 intermediate and fastest growing population bins shown in panel A. **C.** Plot showing the correlation between
2367 the average RplA-GFP accumulation and HupA-mCherry depletion at mid-cell across the growth rate bins
2368 (mean ± SD, 93 to 860 cell division cycles per bin) shown in panel A.
2369

2370 **Figure 2 – figure supplement 3: Calculation of RplA-msfGFP concentration after cell curvature**
2371 **correction. A.** Average 2D RplA-msfGFP projections for short (2.5 to 3 μm – left), unconstricted cells and
2372 long (3.5 and 5.5 μm - right) constricted cells. The average RplA-msfGFP signal from 1000 sampled cells
2373 (CJW7651) is shown for each population. **B.** The 2D cell areas were divided in cylindrical sectors with a
2374 height (h) of a single pixel. The number of cylindrical sectors corresponds to the average cell length in pixels
2375 (40 and 60 sectors for the unconstricted and constricted cells, respectively). The radius (r) of each
2376 cylindrical segment corresponds to half the cell diameter for that specific cell length position. The cylindrical
2377 segments at the poles or constriction site have a smaller radius due to the curvature of the cell boundaries.
2378 The division of the cell area into cylindrical segments allowed us to calculate the volume for each segment
2379 ($V_{cylinder} = \pi\, r^2\, h$). The sum of the fluorescence per segment was corrected for the 3D curvature of the cell
2380 boundaries by dividing by the volume of the cylinder, either considering the entire cell width or different
2381 depths of view narrower than the maximal cell width. **C.** One-dimensional profiles of the cylinder diameter
2382 are also indicative of the cell curvature at the poles and constriction site. **D.** Comparisons of the 1D average
2383 RplA-msfGFP projection between the poles before (dashed lines) or after correcting for the cell curvature

(solid lines) for different depths of view (colormap). The uncorrected signal (dashed lines) corresponds to the average fluorescence along each cylindrical segment (mean of pixel intensities). The 1D profiles were normalized by dividing by the maximal RplA-msfGFP concentration at mid-cell. This correction shows that the pronounced decrease of the RplA-msfGFP fluorescence at the poles is the result of the curvature of the cell boundaries. The observed over-correction at the cell poles for larger depths of view (> 8 pixels or px) is likely due to the over-estimation of the cell segmentation mask that was determined based on the phase contrast snapshot images of cells on agarose pads.

Figure 3 – figure supplement 1: Quantification of the polysome and nucleoid asymmetries using fitted Gaussian functions. A. Example images of RplA-GFP and HupA-mCherry fluorescence signals in a single newborn cell instance. **B.** Plots showing the Gaussian-function fitting on RplA-GFP and HupA-mCherry intensity profiles from the single cell snapshot shown in panel A. Three Gaussian functions were fitted to the RplA-GFP fluorescence in newborn cells (eq. 11 in Methods), capturing the accumulation of polysomes at mid-cell and the poles. Two Gaussian functions were fitted to the HupA-mCherry fluorescence (eq. 12 in methods) capturing the two lobes of the segregating sister nucleoids. The parameters of the fitted Gaussian functions provided information about the position (μ: mean) and the concentration (A: amplitude) of each fluorescence statistic, as well as the cell length range occupied by it (σ: standard deviation). The Gaussian area (eq. 13 in Methods) corresponds to the abundance of each macromolecule. The RplA-GFP Gaussians were fitted above the cellular background, which presumably corresponds to the uniform fluorescence of free ribosomes or ribosomal subunits. For the HupA-mCherry Gaussian fittings, the cellular background corresponds to the DNA-free cell regions. The Gaussian parameters were also used to describe the polysome asymmetries between the poles (eq. 14 in Methods) as well as the position of the nucleoid around the cell center (eq. 15 in Methods). These statistics were used in Figure 3B. **C.** Gaussian functions were also fitted to the ensemble average RplA-GFP and HupA-mCherry fluorescence (right) calculated from all the cell segmentation instances of a single cell division cycle, 0-10% from birth to division (left). **D.** The Gaussian fitting to the ensemble RplA-GFP and HupA-mCherry intensity profiles (concentration in arbitrary fluorescence units) early in the cell division cycle for the 2D projection shown in panel C (right).

Figure 3 – figure supplement 2: Correlations between the polysome distribution statistics and the nucleoid compaction asymmetries. A. Plots showing the nucleoid and polysome density axial asymmetry determined using the parameters of the fitted Gaussians on the HupA-mCherry and RplA-GFP fluorescence (eq. 16 and eq. 18 in Methods). **B.** Plots showing the scaled correlations between the polysome Gaussian parameters (μ, A, and σ for each polysome accumulation) and the nucleoid density asymmetry (eq. 16 in Method; 2103 cell division cycles). Each marker corresponds to the data for a single cell division cycle (0-10% into the cell division cycle) as in Figure 3 – figure supplement 1C-D. A Gaussian kernel density estimation (KDE) was used to illustrate the density of the scatter plots (see Methods). **C.** Bar graph showing

the coefficients of a linear mixed-effects model (see eq. 17 in Methods) used to identify the polysome statistics that contribute to the nucleoid density asymmetry. The highly contributing polysome statistics were combined into a compound polysome statistic (eq. 18 in Methods) that describes the available DNA space between polysome accumulations. This compound statistic correlates with the nucleoid density asymmetry (eq. 16 in Methods) as shown in Figure 3F. The stars indicate the polysome statistics that most significantly correlate with the nucleoid density asymmetry (absolute coefficient above 0.3).

Figure 4 – figure supplement 1: Effects of chloramphenicol treatment on nucleoids in non-dividing cells. A. Representative example of an elongated cephalexin-treated cell that does not fuse its nucleoids upon chloramphenicol treatment. **B.** Representative example of an elongated cephalexin-treated cell that fuses two of its nucleoids upon chloramphenicol treatment. **C.** Plot showing the distributions of the minimum distance between adjacent nucleoids in cells where nucleoid fusion happens (n = 67), compared to cells that do not display nucleoid fusion (n = 134). The two subpopulations were classified as described in the Methods section.

Figure 4 – figure supplement 2: Determination of simulated cell growth parameters based on experimental measurements. Polysome and nucleoid dynamics were simulated for 10 different growth rates. The predivisional polysome and nucleoid profiles of simulated trajectories initialized from the steady state (Figure 4A) were used as initial conditions (D_n = 10^{-3} μm^2/s). The cell length at birth increased with growth rate according to published measurements (Govers et al., 2024).

Figure 4 – figure supplement 3: Comparison of cell length at nucleoid splitting between simulations and experimental data. Across different growth rates, the cell lengths at nucleoids splitting are compared between our model simulations and the experimentally determined population-averaged statistics (Govers et al., 2024). The range of the y-axis spans 2 μm (between 3 and 5 μm) to match the ~2 μm range of the cell areas at birth across nutrient conditions, which spans between 2 and 4 μm in Figure 4 – figure supplement 2.

Figure 4 – figure supplement 4: Simulation of an extended model with three different polysome species. Kymographs of simulated data of an extended version of the theoretical model that considers three polysome species with different diffusion coefficients $D_p = 0.018,\ 0.023, or\ 0.028\ \mu\mathrm{m}^2/\mathrm{s}$, representing polysomes with a decreasing number of ribosomes.

Figure 6 – figure supplement 1: Phenotypic effects of transcription inhibition. Plots showing cellular parameters (instantaneous growth rate, cell area, nucleoid area, and the ratio between nucleoid area and cell area, or NC ratio) affected by the rifampicin treatment. The instantaneous growth rate was estimated

using the log-transformed cell area, using a rolling window of 10 min. The black line corresponds to the averages from 1859 cell division cycles and the gray-shaded area indicates the range of one standard deviation around the mean. The two cycles of rifampicin treatment (as shown in Figure 5A) were overlaid for this plot, using the time of rifampicin addition as t = 0 min.

Figure 7 – figure supplement 1: DNA content during protein overexpression from plasmids. Plots showing the scaling between the DNA content (DRAQ5 fluorescence area) and the cell size (side scatter area) quantified by flow cytometry, comparing uninduced and induced (100μM IPTG for 200 min) conditions for CJW7798 cells. Data from three biological data are shown.

Figure 7 – figure supplement 2: Simulations of ectopic polysome formations away from the nucleoid. Polysome formation was introduced at fixed nucleoid-free regions in the theoretical model to mimic the ectopic polysome formation due to plasmid-driven expression in experiments (as in Figure 7). The model recapitulates the two main phenotypes observed in experiments. The simulations were initialized from the steady-state polysome and nucleoid distribution, similar to the steady state in Figure 4A. **A.** Kymograph of simulated data for which polysomes are ectopically produced near the cell pole, at a rate equivalent to 46% of total polysome production at cell birth. **B.** Kymograph of simulated data for which polysomes are produced between the sister nucleoids, at a rate equivalent to 47% of total polysome production at cell birth.

Figure 7 – figure supplement 3: Phenotypic effects of prolonged protein overexpression from plasmids. Representative phase contrast and fluorescence images of cells (CJW7798) after prolonged induction (100 μM IPTG, for 9 h and 15 min) of mTagBFP2 expression from aT7 promoter on a multi-copy plasmid.

Figure 8 – figure supplement 1: Phenotypic of effects of cell growth under A22 and cephalexin treatment. Representative phase contrast and fluorescence images of cells (CJW7323) treated with A22 (4 μg/mL) alone or with both A22 (4 μg/mL) and cephalexin (50 μg/mL) for 130 min.

Movie legends

Movie S1: Example time-lapse sequence showing ribosome and nucleoid dynamics during cell growth under steady state condition in a microfluidic channel. Shown are corresponding inverted phase contrast signal, RplA-GFP signal, HupA-mCherry signal, cell contours (based on phase contrast signals) and nucleoid contours (based on nucleoid signal segmentation) of *E. coli* cells (CJW7323) grown in a microfluidic channel supplemented with M9gluCAAT. The white circles indicate the centroid of the cell segmentation masks and the extending lines indicate the tracked cell traces.

Movie S2: Video showing the average subcellular distribution of ribosome and nucleoid signals from birth to division. Shown are 2D average RplA-GFP (top) and HupA-mCherry (bottom) projections from birth to division, with corresponding average intensity profiles (right). The cell projections are oriented from the old pole on the left to the new pole on the right. The average cell contour is also drawn. Ensemble data from 4122 division cycles of CJW7323 cells growing in M9gluCAAT are shown.

Movie S3: Video showing simulated 1D profiles of polysome and nucleoid concentration during slow and fast cell growth. Simulations during slow (left) and fast (right) growth are shown. The simulations were initialized from the equilibrium configuration, with a compact symmetric nucleoid (Dn = 10^{-3} μm^2/sec) at the cell center.

Movie S4: Video showing the effects of rifampicin addition on cell growth, ribosome signal heterogeneity, nucleoid segregation, and nucleoid compaction. Examples of five microfluidic channels showing the corresponding inverted phase contrast, RplA-GFP and HupA-mCherry signals (from left to right) of cells (CJW7323) growing within microfluidic channels. Rifampicin was added at 120 and 720 min. Each antibiotic treatment lasted 120 min.

Movie S5: Video showing the effects of ectopic polysome formation on nucleoid dynamics over time. The RplA-GFP and HupA-mCherry fluorescence normalized (norm.) by the average cell fluorescence are shown, together with their corresponding phase contrast image, for multiple cells (CJW7798) in succession following induction of mTagBFP2 expression from a T7 promoter on a multi-copy plasmid. The scale bar indicates 1 μm, and the time since cell birth is shown in minutes. The cell contours indicate the boundaries of the cell masks obtained by cell segmentation of the corresponding phase contrast images.

Movie S6 Video showing how the loss of cell width confinement due to cephalexin and A22 treatment affects ribosome and nucleoid distributions over time. Fluorescence images of RplA-GFP and HupA-mCherry fluorescence (fluor.) normalized by the average cellular fluorescence images, together with their corresponding phase contrast images, are shown for cells (CJW7323) following treatment with A22 (4 μg/mL) and cephalexin (50 μm/mL). The scale bar indicates 1 μm. The time since drug addition is shown in minutes.

2532 **Supplementary tables**

2533 **Table S1. Growth medium abbreviation and composition.**

Abbreviation	Composition
M9acet	1x M9 salts, 0.2% acetate (sodium salt)
M9acetCAAT	1x M9 salts, 0.2% acetate, 0.1% casamino acids, 1µg/mL thiamine
M9fuc	1x M9 salts, 0.2% fucose
M9fucCAAT	1x M9 salts, 0.2% fucose, 0.1% casamino acids, 1µg/mL thiamine
M9fum	1x M9 salts, 0.2% fumarate (disodium salt)
M9fumCAAT	1x M9 salts, 0.2% fumarate, 0.1% casamino acids, 1µg/mL thiamine
M9GlcNAc	1x M9 salts, 0.2% N-acetylglucosamine
M9GlcNAcCAAT	1x M9 salts, 0.2% N-acetylglucosamine, 0.1% casamino acids, 1µg/mL thiamine
M9glu	1x M9 salts, 0.2% glucose
M9gluCAAT	1x M9 salts, 0.2% glucose, 0.1% casamino acids, 1µg/mL thiamine
M9gly	1x M9 salts, 0.2% glycerol
M9glyCAAT	1x M9 salts, 0.2% glycerol, 0.1% casamino acids, 1µg/mL thiamine
M9Lala	1x M9 salts, 0.2% L-alanine
M9LalaCAAT	1x M9 salts, 0.2% L-alanine, 0.1% casamino acids, 1µg/mL thiamine
M9Lara	1x M9 salts, 0.2% L-arabinose
M9LaraCAAT	1x M9 salts, 0.2% L-arabinose, 0.1% casamino acids, 1µg/mL thiamine
M9mala	1x M9 salts, 0.2% malate (sodium salt)
M9malaCAAT	1x M9 salts, 0.2% malate, 0.1% casamino acids, 1µg/mL thiamine
M9malt	1x M9 salts, 0.2% maltose
M9maltCAAT	1x M9 salts, 0.2% maltose, 0.1% casamino acids, 1µg/mL thiamine
M9mann	1x M9 salts, 0.2% mannose
M9mannCAAT	1x M9 salts, 0.2% mannose, 0,1% casamino acids, 1µg/mL thiamine
M9pyr	1x M9 salts, 0.2% pyruvate (sodium salt)
M9pyrCAAT	1x M9 salts, 0.2% pyruvate, 0,1% casamino acids, 1µg/mL thiamine
M9sorb	1x M9 salts, 0.2% sorbitol
M9sorbCAAT	1x M9 salts, 0.2% sorbitol, 0,1% casamino acids, 1µg/mL thiamine
M9succ	1x M9 salts, 0.2% succinate (disodium salt)
M9succCAAT	1x M9 salts, 0.2% succinate, 0,1% casamino acids, 1µg/mL thiamine
M9treh	1x M9 salts, 0.2% trehalose
M9trehCAAT	1x M9 salts, 0.2% trehalose, 0,1% casamino acids, 1µg/mL thiamine
M9xyl	1x M9 salts, 0.2% xylose
M9xylCAAT	1x M9 salts, 0.2% xylose, 0,1% casamino acids, 1µg/mL thiamine

2534

2535

2536 **Table S2: *Escherichia coli* strains used in this study.**

Strain	Genotype	Source
MG1655	*E. coli* MG1655 (F-lambda- *ilvG- rfb-50 rph-1*)	(Guyer et al., 1981; Jensen, 1993)
MG1655 (DE3)	*E. coli* MG1655 (DE3)	Kind gift from Dr K. Prather (Massachusetts Institute of Technology), (Tseng et al., 2010b)
CJW5158	*E. coli* BW25113 *hupA*::*hupA-mcherry-frt-kanR-frt*	(Gray et al., 2019)
CJW6723	*E. coli* MG1655 Δ*lacZYA*::P_{lac}-*egfp-µNS hup*A:*hupA-mcherry*	(Gray et al., 2019)
CJW6768	*E. coli* MG1655 *rplA*::*rplA-meos2*	(Sanamrad et al., 2014)
CJW6769	*E. coli* MG1655 *rspB*::*rpsB-meos2*	(Sanamrad et al., 2014)
CJW7019	*E. coli* MG1655 *rplA*::*rplA-msfgfp-frt-kanR-frt*	(Gray et al., 2019)
CJW7020	*E. coli* MG1655 *rplA*::*rplA-msfgfp*	(Gray et al., 2019)
CJW7021	*E. coli* MG1655 *rpsB*::*rpsB-msfgfp*	(Gray et al., 2019)
CJW7144	*E. coli* MG1655 Δ*lacZYA*::P_{lac}-*mcherry-µNS-frt-kanR-frt*	This study
CJW7145	*E. coli* MG1655 Δ*lacZYA*::P_{lac}-*mcherry-µNS-frt-kanR-frt rplA*::*rplA-msfgfp*	This study
CJW7323	*E. coli* MG1655 *rplA*::*rplA-msfgfp hupA*::*hupA-mcherry*	(Xiang et al., 2021)
CJW7466	*E. coli* MG1655 (DE3) *hup*A:*hupA-mcherry*	This study
CJW7651	*E. coli* MG1655 Δ*lacZYA*::P_{lac}-*mcherry-µNS rplA*::*rplA-msfgfp*	This study
CJW7766	*E. coli* MG1655 (DE3) *hup*A:*hupA-mcherry rplA*::*rplA-msfgfp-frt-kanR-frt*	This study
CJW7798	*E. coli* MG1655 (DE3) *hup*A:*hupA-mcherry rplA*::*rplA-msfgfp-frt-kanR-frt* | *pET28:mTagBFP2-CmR*	This study

2537

2538

2539 **Table S3: Plasmids used in this study.**

Plasmid name	Relevant genetic elements	Source
pKD13	*frt-kanR-frt-R6Kori-ampR*	(Datsenko and Wanner, 2000)
pKD46	*araC-bet-exo-A101(Ts)ori-ampR*	(Datsenko and Wanner, 2000)
pCP20	*cmR-A101(Ts)ori-ampR-flp-λ-repressor(Ts)*	(Datsenko and Wanner, 2000)
pER12	*pBAD322A-gfp-μNS*	Kind gift from Dr A. Janakiraman (City College of New York), (Broering et al., 2005)
pER12-mcherry	*pBAD322A-mcherry-μNS*	This study
pAPG1	*attB-pBAD322A-mcherry-μNS-attB-kanR-ColE1ori*	This study
pSB3C5-proA-B0032-E0051	*PproA-lacZα-GFP-p15Aori-cmR*	(Davis et al., 2011)
pET28:GFP	*PT7-lacO-GFP-kanR-pMB1ori-lacI*	(Shis and Bennett, 2013)
pBAD:TagBFP2	*araC-ParaBAD-mTagBFP2-ampR-pBAD322ori*	(Subach et al., 2011)
pET28:mTagBFP2	*PT7-lacO-mTagBFP2-kanR-pMB1ori-lacI*	This study
pET28:mTagBFP2-CmR	*PT7-lacO-mTagBFP2-cmR-pMB1ori-lacI*	This study

2540
2541
2542 **Table S4: DNA oligonucleotides used in this study.**

Oligo name	Sequence	Source
ER12-MCR-fwd	5' CTCCATACCCGTTTTTTTGGGCTAGCAGGAGGAATTCATGGTGAGCAAGGGCG AGGAG 3'	This study
ER12-MCR-rev2	5' CACTGGAGGAGCCTGCTTTTTTGTACAAACTTGTTGACTTGTACAGCTCGTCCA TG 3'	This study
μNSmCherry fwd	5' CACAGGTTGCTCCGGGCTATGAAATAGAAAAATGAATCCGTTGAAGCCTGATC GATGCATAATGTGCC 3'	This study
μNSmCherry rev	5' AGCTCCAGCCTACACAGAGTTTGTAGAAACGCAAAAAG 3'	This study
FRT_KanR fwd	5' GTTTCTACAAACTCTGTGTAGGCTGGAGCTGC 3'	This study
FRT_KanR Rev	5' TTAAAGGTATTAAAAACAACTTTTTGTCTTTTTACCTTCCCGTTTCGCTC CTGTCAAACATGAGAATTAATTCC 3'	This study
ColE1 fwd	5' GAGCGAAACGGGAAGGTAAAAAGACAAAAAGTTGTTTTTAATACCTTTAA CGTTCCACTGAGCGTC 3'	This study
ColE1 rev	5' CAGGCTTCAACGGATTCATTTTTCTATTTCATAGCCCGGAGCAACCTGTG GGTTATCCACAGAATCAGG 3'	This study
pAPG1 seq1	5' GATCAAGCAGAGGCTGAAG 3'	This study
pAPG1 seq2	5' CCAGGCATCAAATTAAGC 3'	This study
pAPG1 seq3	5' TCTACGTGTTCCGCTTCC 3'	This study
pAPG1 seq4	5' TTGAAGCCTGATCGATGC 3'	This study
pAPG1 seq5	5' AAGATTAGCGGATCCTACC 3'	This study
lacZYA_redμNS fwd	5' TATGTTGTGTGGAATTGTGAGCGGATAACAATTTCACACAGGAAACAGCT ATGGTGAGCAAGGGCGA 3'	This study
lacZYA_redμNS rev	5' CAATTTTTATAATTTAAACTGACGATTCAACTTTATAATCTTTGAAATAA GGATCCGTCGACCTGCAG 3'	This study
LacI fwd	5' GGCCGATTCATTAATGCAGCTGGC 3'	This study
CynX rev	5' GGCCTGATAAGCGCAGCGTATC 3'	This study
mCherry rev	5' GGTGCTTCACGTAGGCCTTGG 3'	This study
KanR fwd	5' CGGAGAACCTGCGTGCAATCC 3'	This study
mTagBFP2 fwd	5' CGGAGCTCGAATTCGGATCCTTAATTAAGCTTGTGCCCCAGTTTG 3'	This study
mTagBFP2 fwd	5' CTTTAAGAAGGAGATATACCATGAGCGAGCTGATTAAGGAGAAC 3'	This study
pET28_one fwd	5' TCCTTAATCAGCTCGCTCATGGTATATCTCCTTCTTAAAGTTAAAC 3'	This study
pET28_one rev	5' GGATAACCGTATTACCGCCTTTGAGTGAGCTGATACCG 3'	This study
pET28_two fwd	5' AGCGGTATCAGCTCACTCAAAGGCGGTAATACGGTTATCC 3'	This study
pET28_two rev	5' TGGGGCACAAGCTTAATTAAGGATCCGAATTCGAGCTCC 3'	This study
pET28mTagBFP2 fwd	5' CTTAGTGACTCGAATTCGCGCGCCAATCCGGATATAGTTCC 3'	This study
pET28mTagBFP2 rev	5' ACTTTCTGGCTGGATGATGGACGTGAGTTTTCGTTCCACTG 3'	This study
cmR fwd	5' AGTGGAACGAAAACTCACGTCCATCATCCAGCCAGAAAGTG 3'	This study
cmR rev	5' GAACTATATCCGGATTGGCGCGCGAATTCGAGTCACTAAGG 3'	This study

2543
2544

2545 **Table S5: Chemicals used in this study.**

Chemical	Source	Catalog number
Agarose	AmericanBio	Cat#AB00972-00500
4',6-diamidine-2'-phenylindole (DAPI), dihydrochloride fluorescent dye	Thermo Fisher Scientific	Cat#D1306
Isopropyl β-D-1-thiogalactopyranoside (IPTG)	Sigma Aldrich	Cat#I5502
Rifampicin	Sigma Aldrich	Cat#R3501
Cephalexin	Sigma Aldrich	Cat#C4895
A22	Sigma Aldrich	Cat#SML0471
Chloramphenicol	Sigma Aldrich	Cat#C0378
4',6-Diamidine-2-phenylindole dihydrochloride (DAPI)	Thermo Fisher Scientific	Cat#D1306
eBioscience™ DRAQ5™	Thermo Fisher Scientific	Cat#65-0880-92

2546
2547
2548 **Table S6: Software used in this study.**

Program / library / script	Package	Source
Oufti	www.oufti.org	(Paintdakhi et al., 2016)
MATLAB	www.mathworks.com	Mathworks
Python	www.python.org	Python Software Foundation
Numpy	www.numpy.org	(Harris et al., 2020)
Scipy	www.scipy.org	(Virtanen et al., 2020)
Pytorch	www.pytorch.org	(Paszke et al., 2019)
Scikit-image	www.scikit-image.org	(Van Der Walt et al., 2014)
Scikit-learn	www.scikit-learn.org/stable/	(Pedregosa et al., 2012)
Statsmodels	www.statsmodels.org/stable/index.html	(Seabold and Perktold, 2010)
Shapely	www.pypi.org/project/shapely/	(Gillies, Sean et al., 2023)
Matplotlib	www.matplotlib.org	(Hunter, 2007)
Seaborn	www.seaborn.pydata.org	(Waskom, 2021)
Pandas	www.pandas.pydata.org	(McKinney, 2010)
Python	Omnipose neural network	(Cutler et al., 2022)
MATLAB	SuperSegger	(Stylianidou et al., 2016)
Python	Unet neural network	(Wiktor et al., 2021; Zhou et al., 2020)
snapshots_analysis_UNET_ghv.py	Snapshot image analysis (from UNET masks) – custom Python class	This study (www.github.com/JacobsWagnerLab/published/tree/master/Papagiannakis_2025)
snapshots_analysis_OUFTI_GrayGovers_ghv.py	Snapshot image analysis (from Oufti masks) – custom Python class	This study (www.github.com/JacobsWagnerLab/published/tree/master/Papagiannakis_2025)
snapshots_analysis_functions.py	Extraction of fluorescence and morphology statistics from cell snapshots – custom Python functions	This study (www.github.com/JacobsWagnerLab/published/tree/master/Papagiannakis_2025)
microfluidics_segmentation_ghv.py	Cell segmentation and tracking from time-lapse images in microfluidics – custom Python class	This study (www.github.com/JacobsWagnerLab/published/tree/master/Papagiannakis_2025)
microfluidics_analysis_functions_ghv.py	Extraction of fluorescence and morphology statistics from time-lapse images	This study (www.github.com/JacobsWagnerLab/published/tree/master/Papagiannakis_2025)

	in microfluidics – custom Python functions	
Omnipose_to_python_ghv.py	Extraction of segmentation masks and tracked lineages from Omnipose/SuperSegger to Python for further analysis	This study (www.github.com/JacobsWagnerLab/published/tree/master/Papagiannakis_2025)
Otsu_phase_segmentation_ghv.py	Cell segmentation and tracking using Otsu thresholding (Otsu, 1979)	This study (www.github.com/JacobsWagnerLab/published/tree/master/Papagiannakis_2025)
LoG_adaptive_image_filter.py	Image filter that applies relative and local thresholding to segment fluorescence objects and particles	This study (www.github.com/JacobsWagnerLab/published/tree/master/Papagiannakis_2025)
Microfluidics_segmentation_and_tracking_example.pdf	Example for cell segmentation and tracking in microfluidics	This study (www.github.com/JacobsWagnerLab/published/tree/master/Papagiannakis_2025)
Analysis_of_cell_morphology_and_fluorescence_in_microfluidics.pdf	Example for the extraction of fluorescence and morphology statistics from time-lapse images in microfluidics	This study (www.github.com/JacobsWagnerLab/published/tree/master/Papagiannakis_2025)
Analysis_of_cell_morphology_and_fluorescence_in_agarose_pads.pdf	Example for the extraction of fluorescence and morphology statistics from cell snapshots	This study (www.github.com/JacobsWagnerLab/published/tree/master/Papagiannakis_2025)
Example_of_using_Otsu_based_segmentation_ghv.pdf	Example for the segmentation of antibiotic-treated cells using the Otsu threshold	This study (www.github.com/JacobsWagnerLab/published/tree/master/Papagiannakis_2025)
tune_diffusion.ipynb	Simulations of the minimal reaction-diffusion model that describes nucleoid segregation in *E. coli*.	This study (https://github.com/qiweiyuu/polysome)
Time_lapse_on_agarose_pad	Python repository that includes the *fluorescence_analysis* class and its associated functions, used to track cell trajectories and analyze their fluorescence statistics in time-lapse images on agarose pads.	This study (https://github.com/alexSysBio/Time_lapse_on_agarose_pad)
flowio_to_pandas	Python repository that includes the *flow_cytometry_class* class and its associated functions, used to parse FCS files into Pandas. This class can also be used for polygon and histogram gating.	This study (https://github.com/alexSysBio/flowio_to_pandas)
nd2_to_array.py	Function used to	This study

	parse .nd2 files into numpy arrays.	(https://github.com/alexSysBio/Adding_ND2_images_to_python)
Bivariate_medial_axis_estimation.py	Functions used to draw the medial axis in segmented cell masks from snapshots or time-lapse images on agarose pads.	This study (https://github.com/alexSysBio/Cell_medial_axis_definitions)
Unever_background_correction.py	Functions used to subtract the background from agarose-pad images.	This study (https://github.com/alexSysBio/Image_background_subtraction)

2549

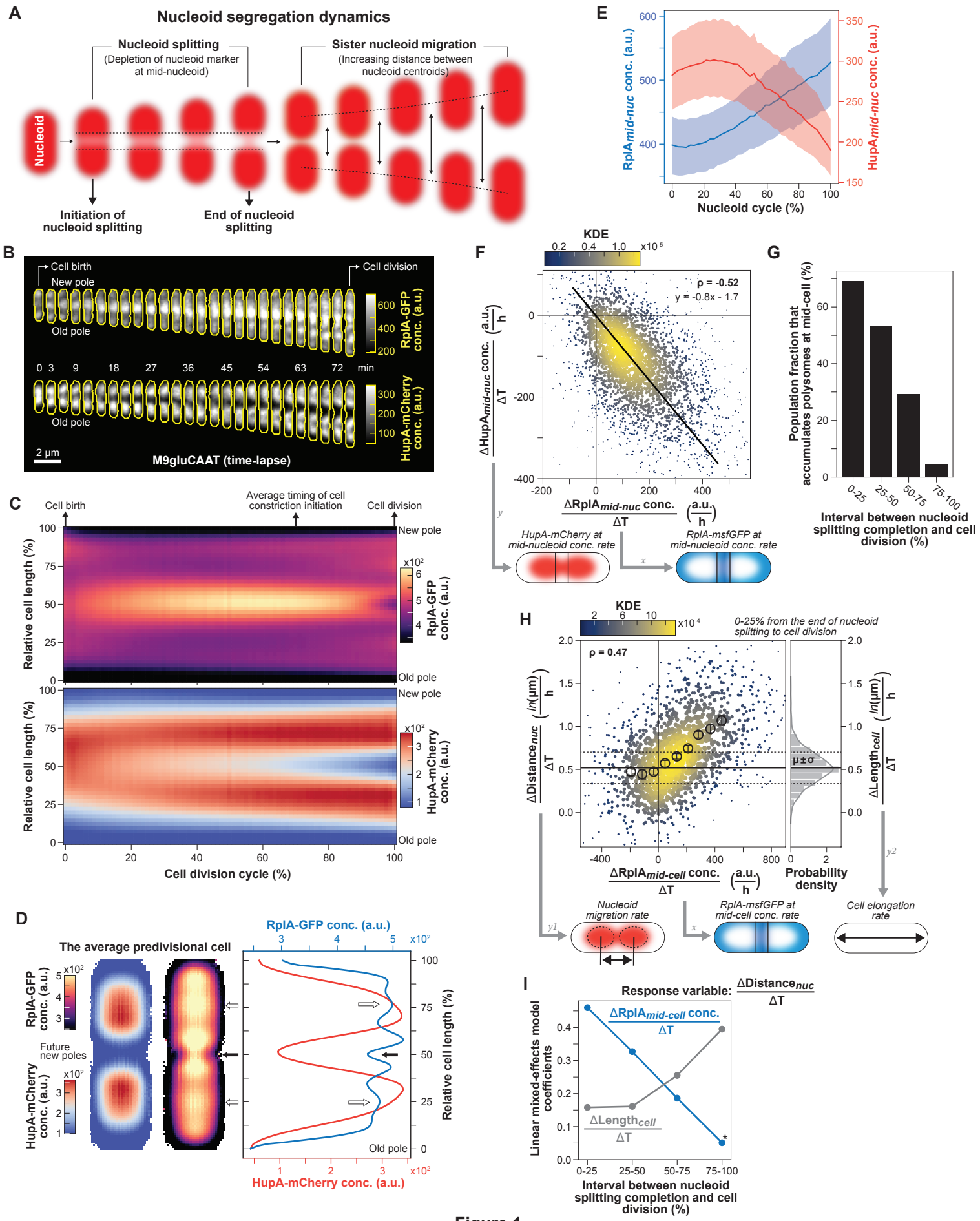
A
Nucleoid segregation dynamics
Nucleoid splitting
(Depletion of nucleoid marker at mid-nucleoid)
Sister nucleoid migration
(Increasing distance between nucleoid centroids)
Nucleoid
Initiation of nucleoid splitting
End of nucleoid splitting
B
Cell birth
New pole
Cell division
Old pole
RplA-GFP conc. (a.u.)
HupA-mCherry conc. (a.u.)
0 3 9 18 27 36 45 54 63 72 min
2 µm
M9gluCAAT (time-lapse)
C
Cell birth
Average timing of cell constriction initiation
Cell division
New pole
Old pole
Relative cell length (%)
RplA-GFP conc. (a.u.)
HupA-mCherry conc. (a.u.)
Cell division cycle (%)
D
The average predivisional cell
RplA-GFP conc. (a.u.)
HupA-mCherry conc. (a.u.)
Future new poles
Old pole
Relative cell length (%)
E
RplA mid-nuc conc. (a.u.)
HupA mid-nuc conc. (a.u.)
Nucleoid cycle (%)
F
KDE
ρ = -0.52
y = -0.8x - 1.7
ΔHupA mid-nuc conc. / ΔT (a.u./h)
ΔRplA mid-nuc conc. / ΔT (a.u./h)
HupA-mCherry at mid-nucleoid conc. rate
RplA-msfGFP at mid-nucleoid conc. rate
G
Population fraction that accumulates polysomes at mid-cell (%)
0-25
25-50
50-75
75-100
Interval between nucleoid splitting completion and cell division (%)
H
KDE
0-25% from the end of nucleoid splitting to cell division
ρ = 0.47
μ±σ
ΔDistance nuc / ΔT (ln(µm)/h)
ΔLength cell / ΔT (ln(µm)/h)
ΔRplA mid-cell conc. / ΔT (a.u./h)
Probability density
Nucleoid migration rate
RplA-msfGFP at mid-cell conc. rate
Cell elongation rate
I
Response variable: ΔDistance nuc / ΔT
ΔRplA mid-cell conc. / ΔT
ΔLength cell / ΔT
Linear mixed-effects model coefficients
Interval between nucleoid splitting completion and cell division (%)

Figure 1

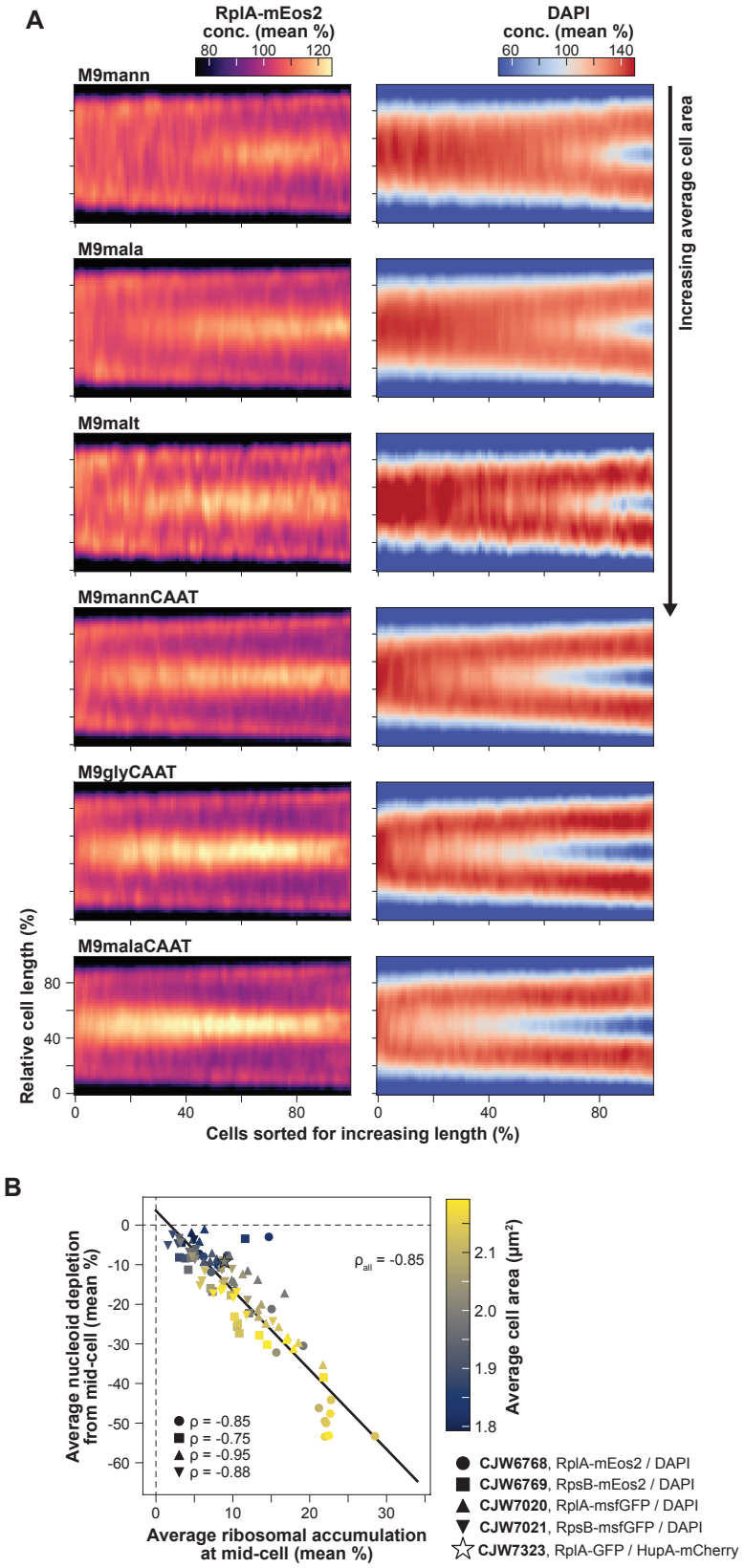
A
RplA-mEos2
conc. (mean %)
80 100 120
DAPI
conc. (mean %)
60 100 140
M9mann
M9mala
M9malt
M9mannCAAT
M9glyCAAT
M9malaCAAT
Increasing average cell area
Relative cell length (%)
0 40 80
Cells sorted for increasing length (%)
B
Average nucleoid depletion from mid-cell (mean %)
Average ribosomal accumulation at mid-cell (mean %)
ρall = -0.85
ρ = -0.85
ρ = -0.75
ρ = -0.95
ρ = -0.88
Average cell area (μm²)
1.8 1.9 2.0 2.1
CJW6768, RplA-mEos2 / DAPI
CJW6769, RpsB-mEos2 / DAPI
CJW7020, RplA-msfGFP / DAPI
CJW7021, RpsB-msfGFP / DAPI
CJW7323, RplA-GFP / HupA-mCherry

Figure 2

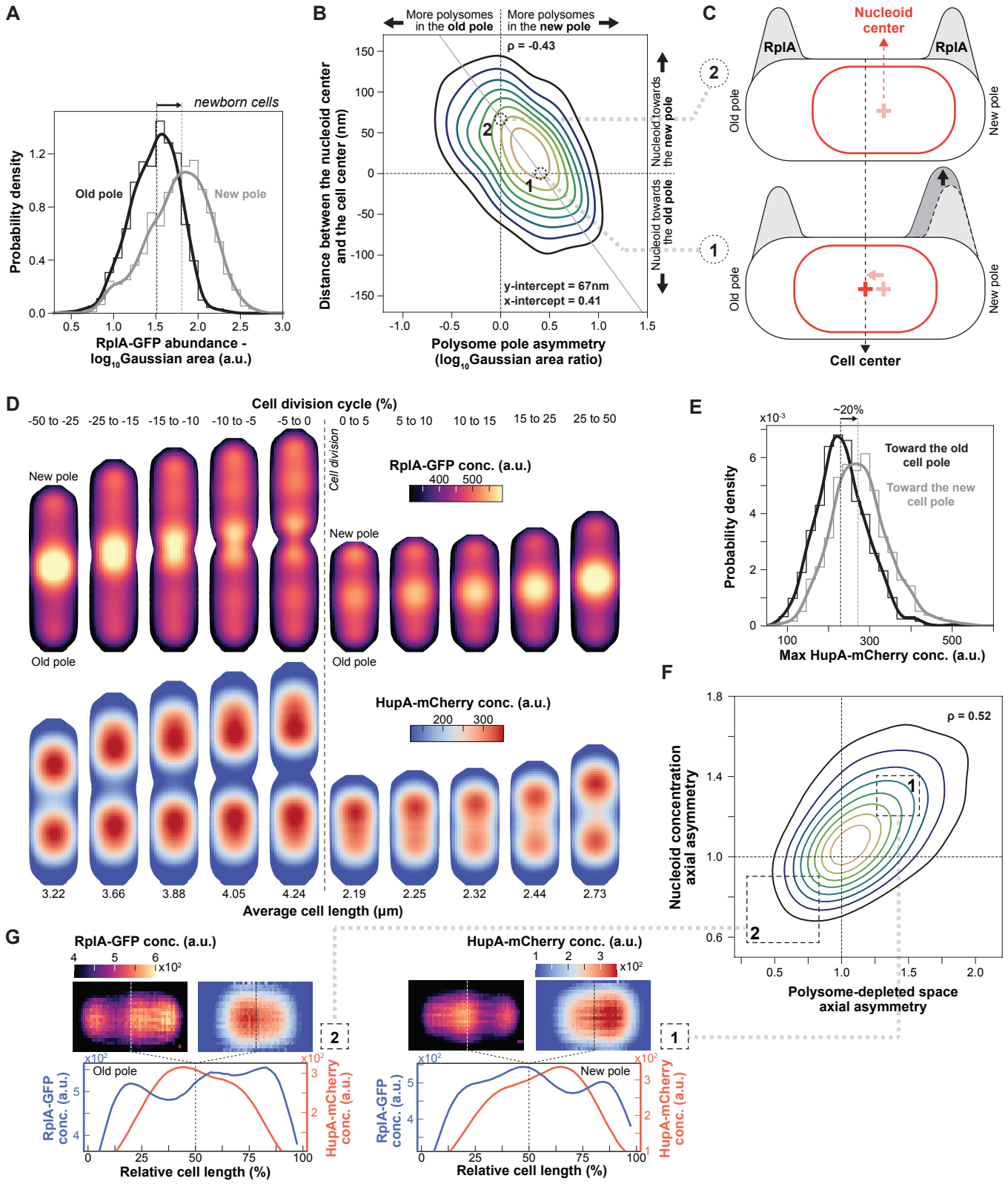
A
newborn cells
Old pole
New pole
Probability density
RplA-GFP abundance - log10Gaussian area (a.u.)
B
More polysomes in the old pole
More polysomes in the new pole
ρ = -0.43
Distance between the nucleoid center and the cell center (nm)
Nucleoid towards the new pole
Nucleoid towards the old pole
y-intercept = 67nm
x-intercept = 0.41
Polysome pole asymmetry (log10Gaussian area ratio)
C
Nucleoid center
RplA
RplA
Old pole
New pole
Cell center
D
Cell division cycle (%)
-50 to -25
-25 to -15
-15 to -10
-10 to -5
-5 to 0
0 to 5
5 to 10
10 to 15
15 to 25
25 to 50
Cell division
RplA-GFP conc. (a.u.)
HupA-mCherry conc. (a.u.)
New pole
Old pole
3.22
3.66
3.88
4.05
4.24
2.19
2.25
2.32
2.44
2.73
Average cell length (µm)
E
~20%
Toward the old cell pole
Toward the new cell pole
Probability density
Max HupA-mCherry conc. (a.u.)
F
ρ = 0.52
Nucleoid concentration axial asymmetry
Polysome-depleted space axial asymmetry
G
RplA-GFP conc. (a.u.)
HupA-mCherry conc. (a.u.)
Old pole
New pole
Relative cell length (%)

Figure 3

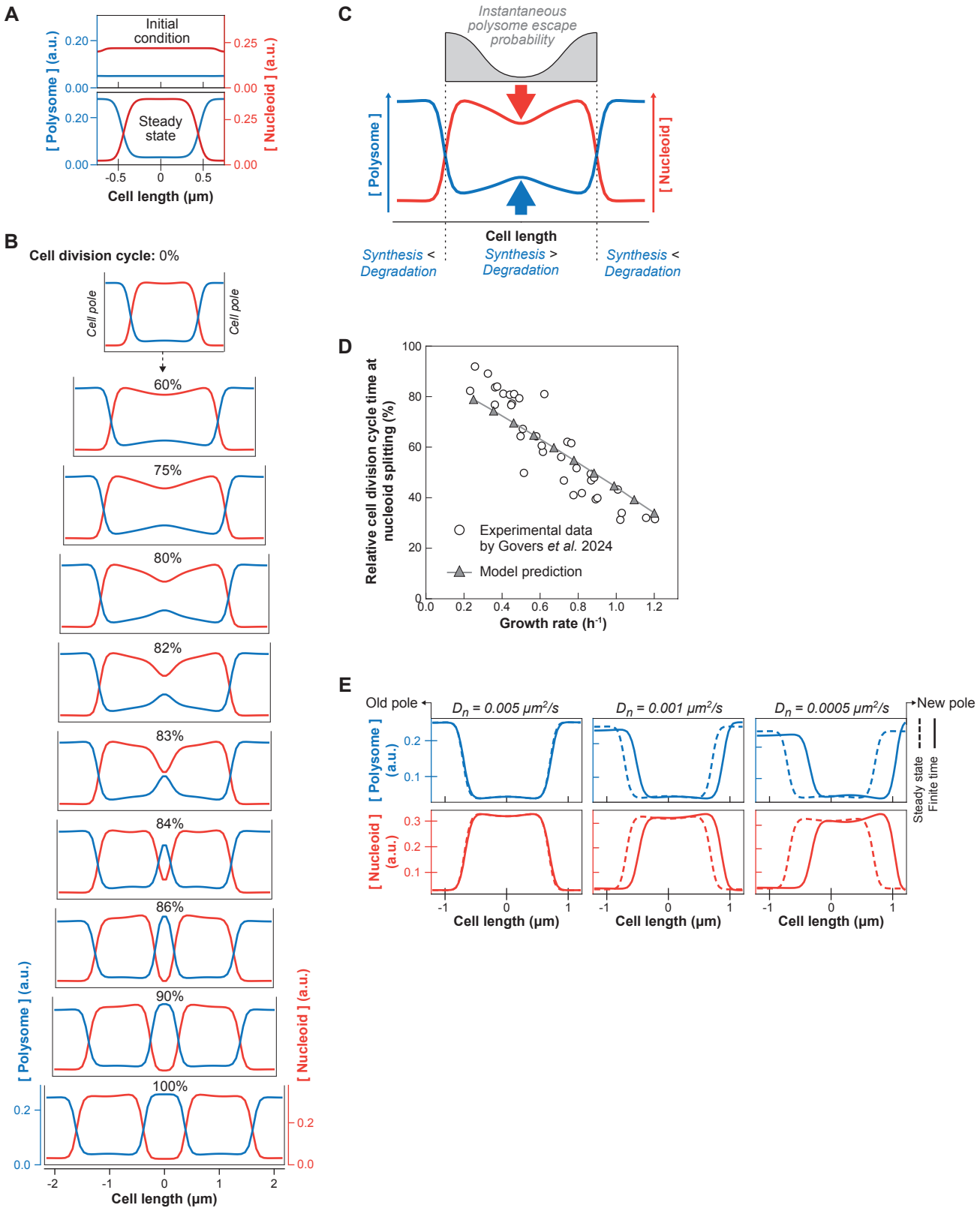
A
Initial condition
Steady state
[Polysome] (a.u.)
[Nucleoid] (a.u.)
Cell length (μm)
B
Cell division cycle: 0%
Cell pole
Cell pole
60%
75%
80%
82%
83%
84%
86%
90%
100%
[Polysome] (a.u.)
[Nucleoid] (a.u.)
Cell length (μm)
C
Instantaneous polysome escape probability
[Polysome]
[Nucleoid]
Cell length
Synthesis < Degradation
Synthesis > Degradation
Synthesis < Degradation
D
Relative cell division cycle time at nucleoid splitting (%)
Experimental data by Govers et al. 2024
Model prediction
Growth rate (h-1)
E
Old pole
New pole
Dn = 0.005 μm2/s
Dn = 0.001 μm2/s
Dn = 0.0005 μm2/s
[Polysome] (a.u.)
[Nucleoid] (a.u.)
Steady state
Finite time
Cell length (μm)
Cell length (μm)
Cell length (μm)

Figure 4

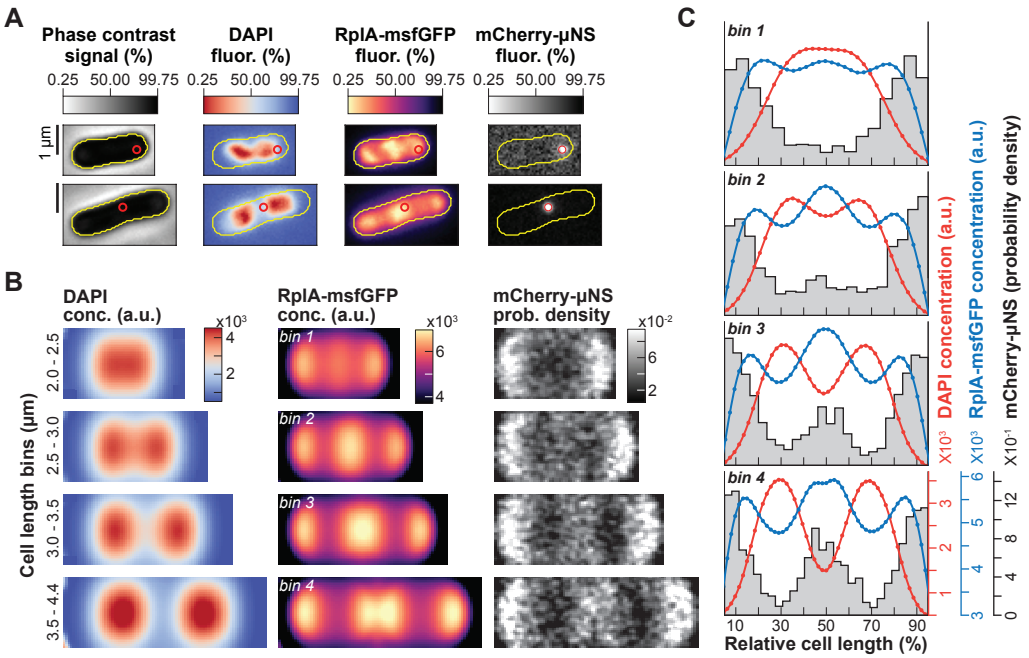
A
Phase contrast signal (%)
DAPI fluor. (%)
RplA-msfGFP fluor. (%)
mCherry-μNS fluor. (%)
0.25 50.00 99.75
1 μm
B
DAPI conc. (a.u.)
RplA-msfGFP conc. (a.u.)
mCherry-μNS prob. density
Cell length bins (μm)
2.0 - 2.5
2.5 - 3.0
3.0 - 3.5
3.5 - 4.4
bin 1
bin 2
bin 3
bin 4
C
DAPI concentration (a.u.)
RplA-msfGFP concentration (a.u.)
mCherry-μNS (probability density)
Relative cell length (%)

Figure 5

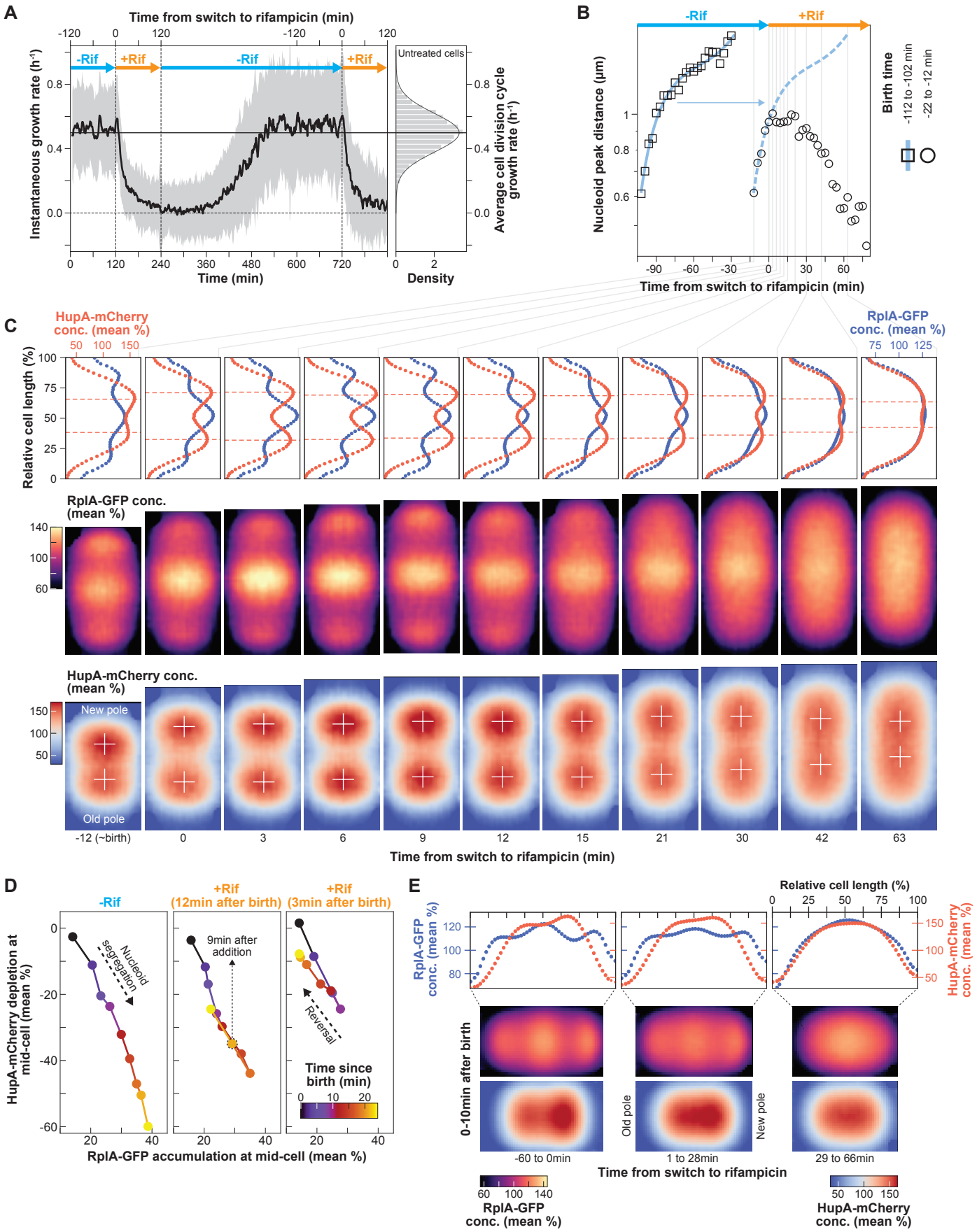
A
Time from switch to rifampicin (min)
-Rif
+Rif
Instantaneous growth rate (h-1)
Time (min)
Untreated cells
Density
Average cell division cycle growth rate (h-1)
B
Nucleoid peak distance (µm)
Time from switch to rifampicin (min)
Birth time
-112 to -102 min
-22 to -12 min
C
HupA-mCherry conc. (mean %)
RplA-GFP conc. (mean %)
Relative cell length (%)
RplA-GFP conc. (mean %)
HupA-mCherry conc. (mean %)
New pole
Old pole
-12 (~birth)
Time from switch to rifampicin (min)
D
-Rif
+Rif (12min after birth)
+Rif (3min after birth)
HupA-mCherry depletion at mid-cell (mean %)
Nucleoid segregation
9min after addition
Reversal
Time since birth (min)
RplA-GFP accumulation at mid-cell (mean %)
E
Relative cell length (%)
RplA-GFP conc. (mean %)
HupA-mCherry conc. (mean %)
0-10min after birth
Old pole
New pole
-60 to 0min
1 to 28min
29 to 66min
Time from switch to rifampicin
RplA-GFP conc. (mean %)
HupA-mCherry conc. (mean %)

Figure 6

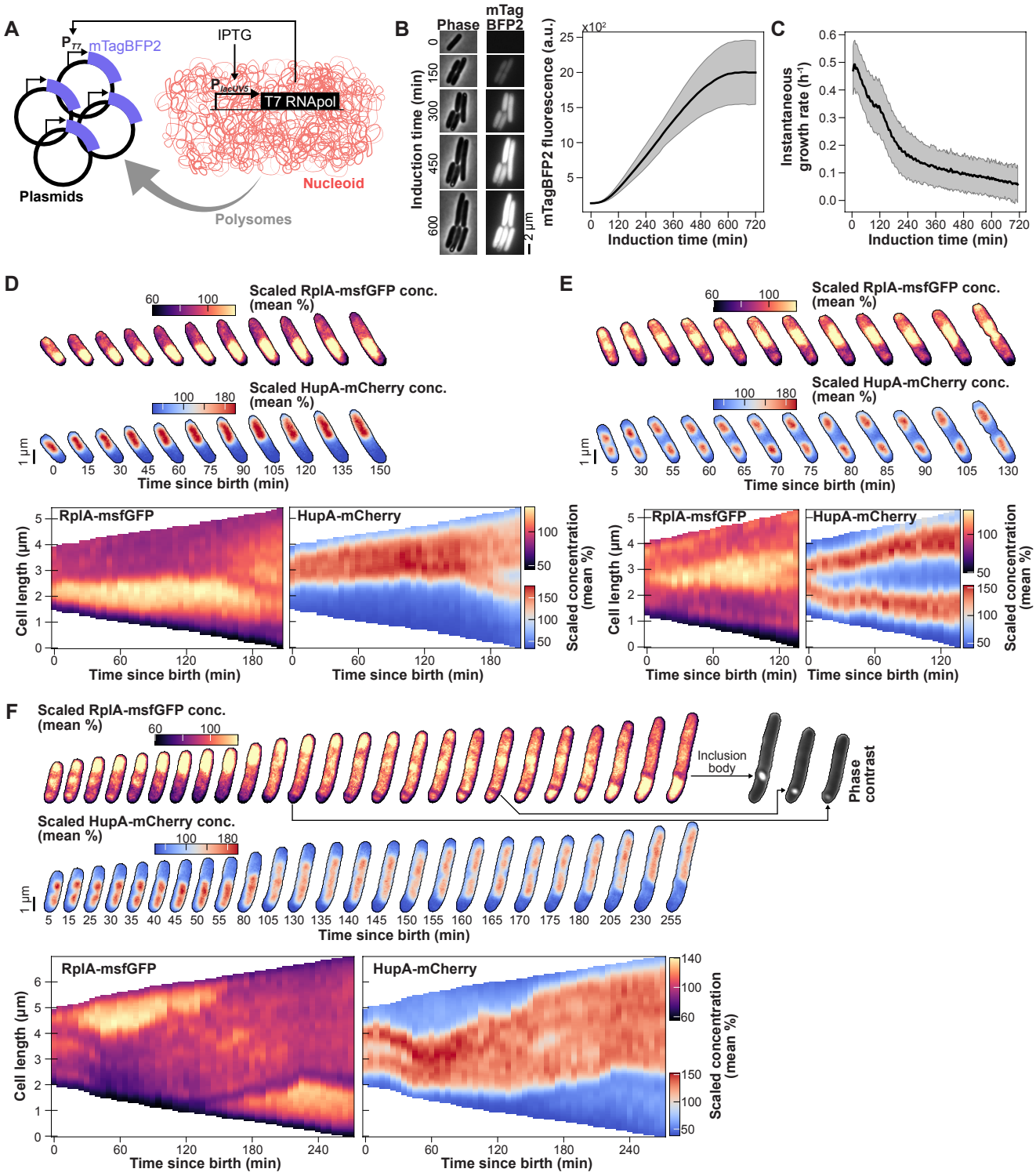
A
IPTG
mTagBFP2
T7 RNApol
Plasmids
Nucleoid
Polysomes
B
Phase
mTag BFP2
Induction time (min)
mTagBFP2 fluorescence (a.u.)
Induction time (min)
C
Instantaneous growth rate (h⁻¹)
Induction time (min)
D
Scaled RplA-msfGFP conc. (mean %)
Scaled HupA-mCherry conc. (mean %)
Time since birth (min)
RplA-msfGFP
HupA-mCherry
Cell length (µm)
Scaled concentration (mean %)
E
Scaled RplA-msfGFP conc. (mean %)
Scaled HupA-mCherry conc. (mean %)
Time since birth (min)
RplA-msfGFP
HupA-mCherry
Cell length (µm)
Scaled concentration (mean %)
F
Scaled RplA-msfGFP conc. (mean %)
Inclusion body
Phase contrast
Scaled HupA-mCherry conc. (mean %)
Time since birth (min)
RplA-msfGFP
HupA-mCherry
Cell length (µm)
Scaled concentration (mean %)

Figure 7

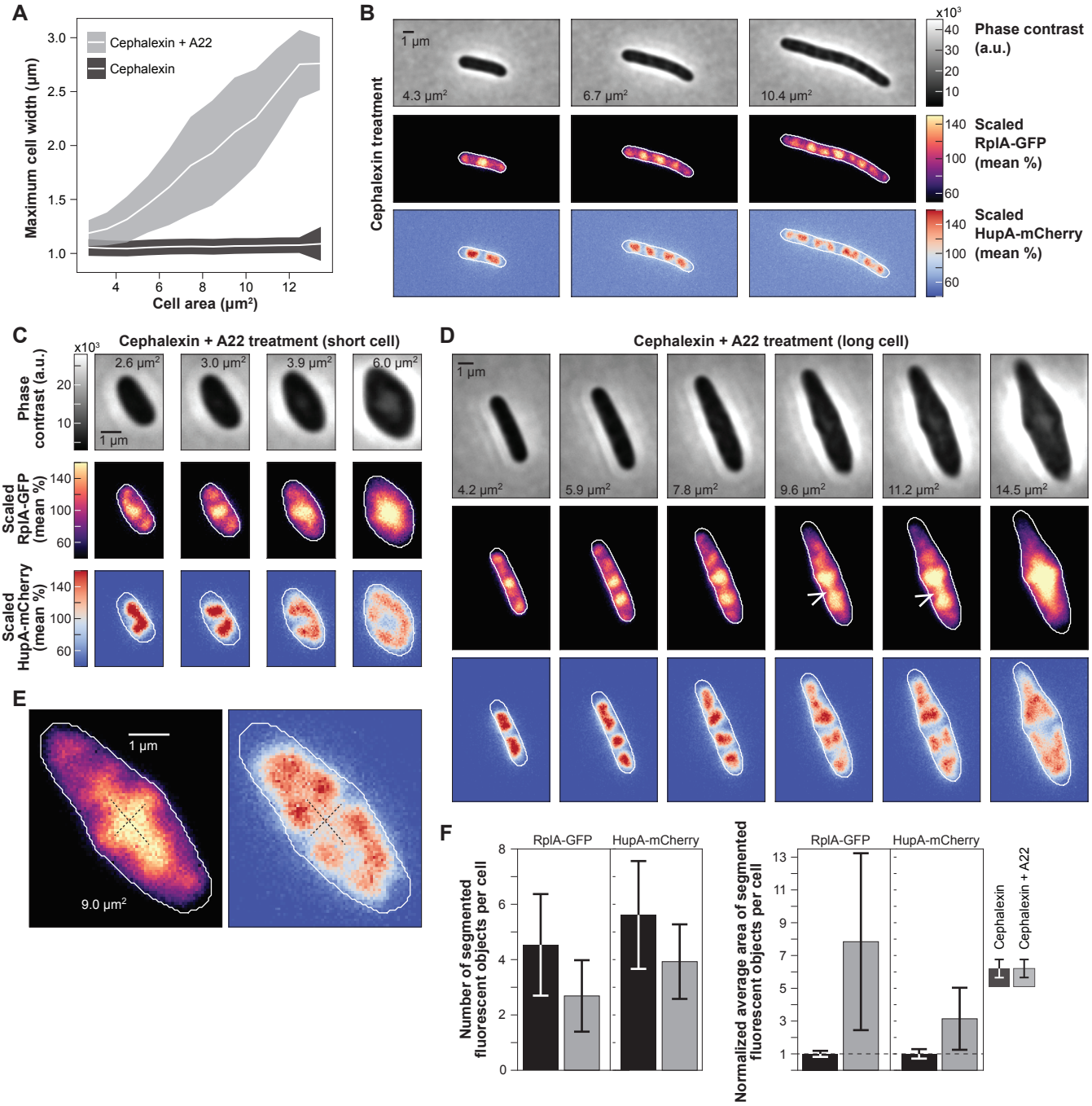
A
Cephalexin + A22
Cephalexin
Maximum cell width (µm)
Cell area (µm²)
B
Cephalexin treatment
1 µm
4.3 µm²
6.7 µm²
10.4 µm²
x10³
Phase contrast (a.u.)
Scaled RplA-GFP (mean %)
Scaled HupA-mCherry (mean %)
C
Cephalexin + A22 treatment (short cell)
2.6 µm²
3.0 µm²
3.9 µm²
6.0 µm²
D
Cephalexin + A22 treatment (long cell)
4.2 µm²
5.9 µm²
7.8 µm²
9.6 µm²
11.2 µm²
14.5 µm²
E
9.0 µm²
F
RplA-GFP
HupA-mCherry
Number of segmented fluorescent objects per cell
Normalized average area of segmented fluorescent objects per cell
Cephalexin
Cephalexin + A22

Figure 8

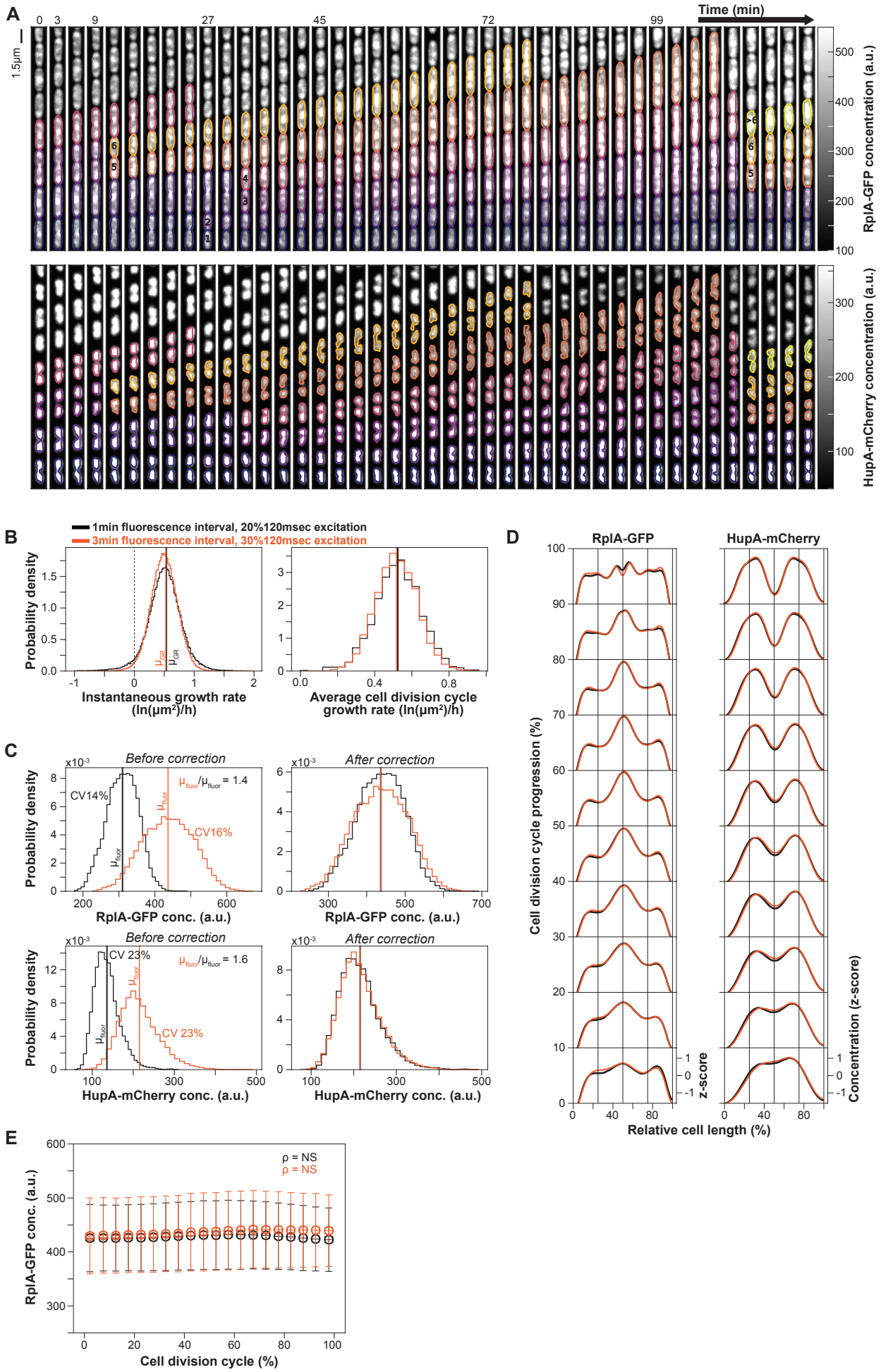

Figure 1 - figure supplement 1

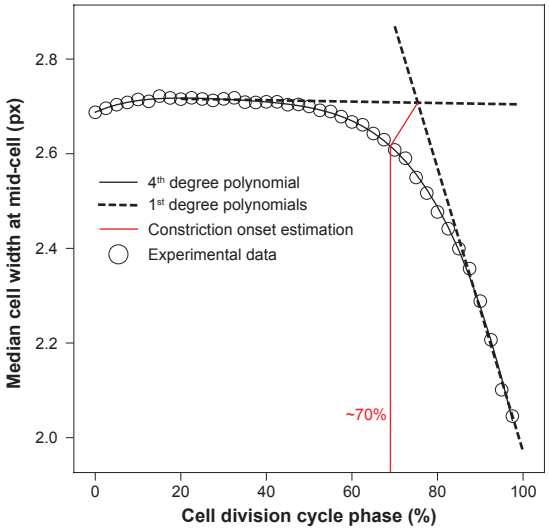

Figure 1 - Figure supplement 2

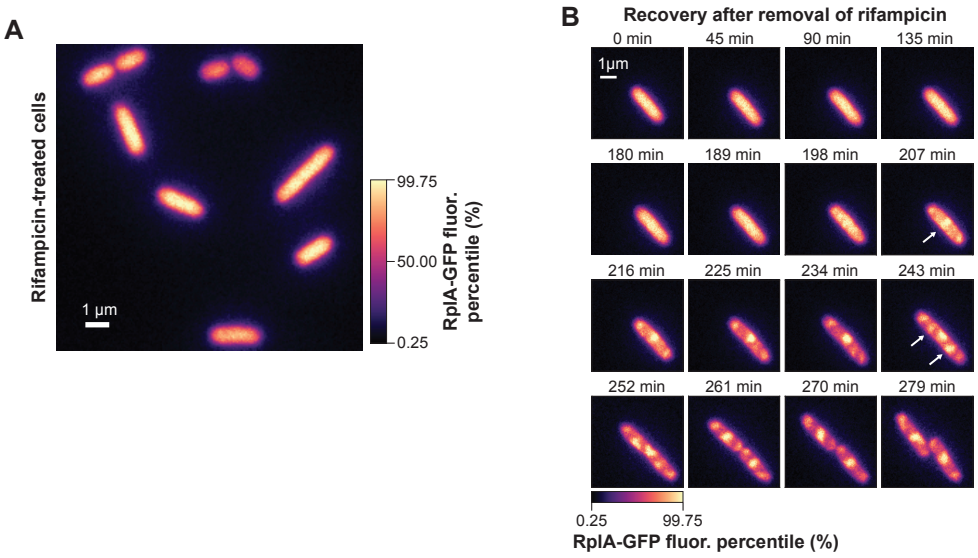

Figure 1 - figure supplement 3

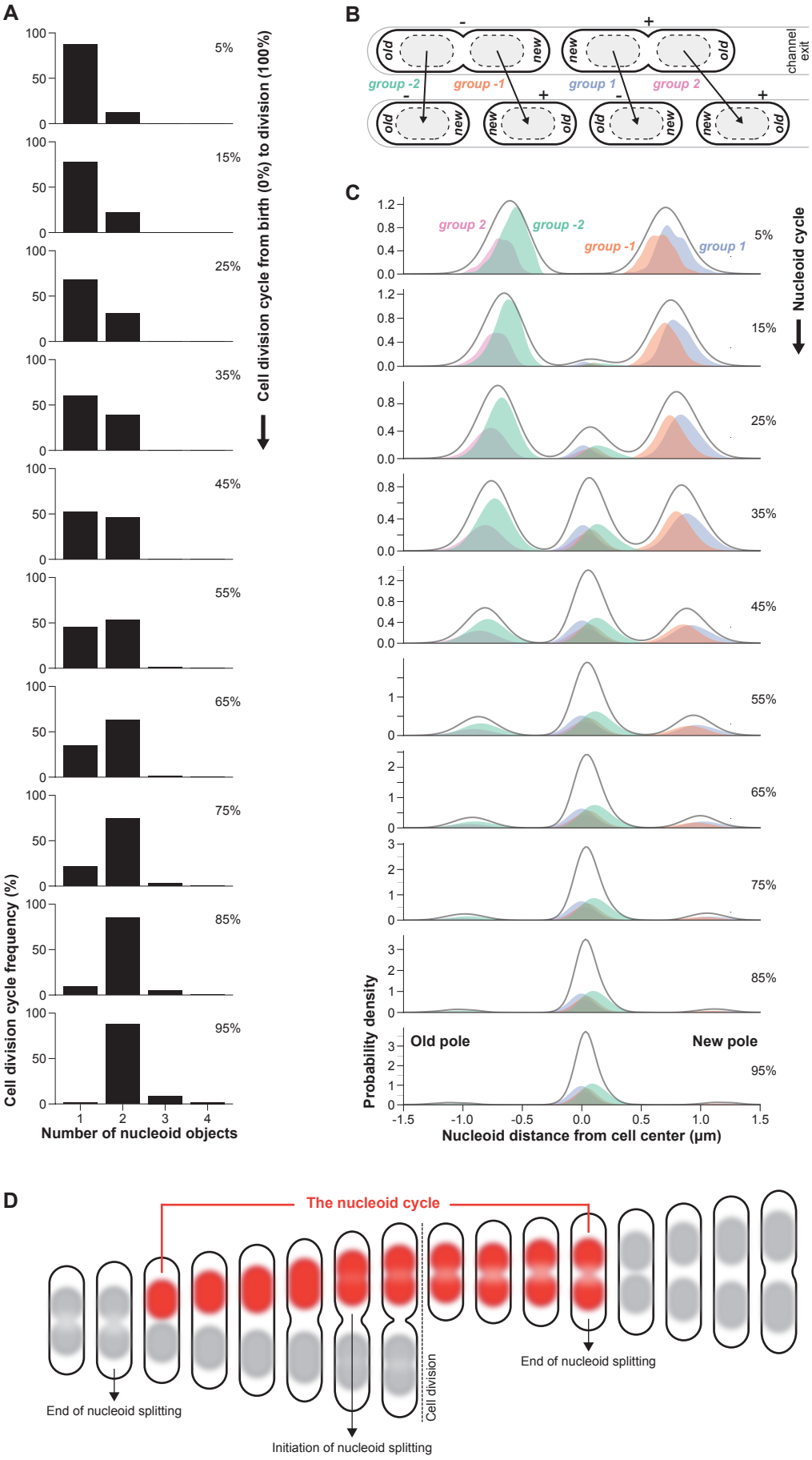

Figure 1 - figure supplement 4

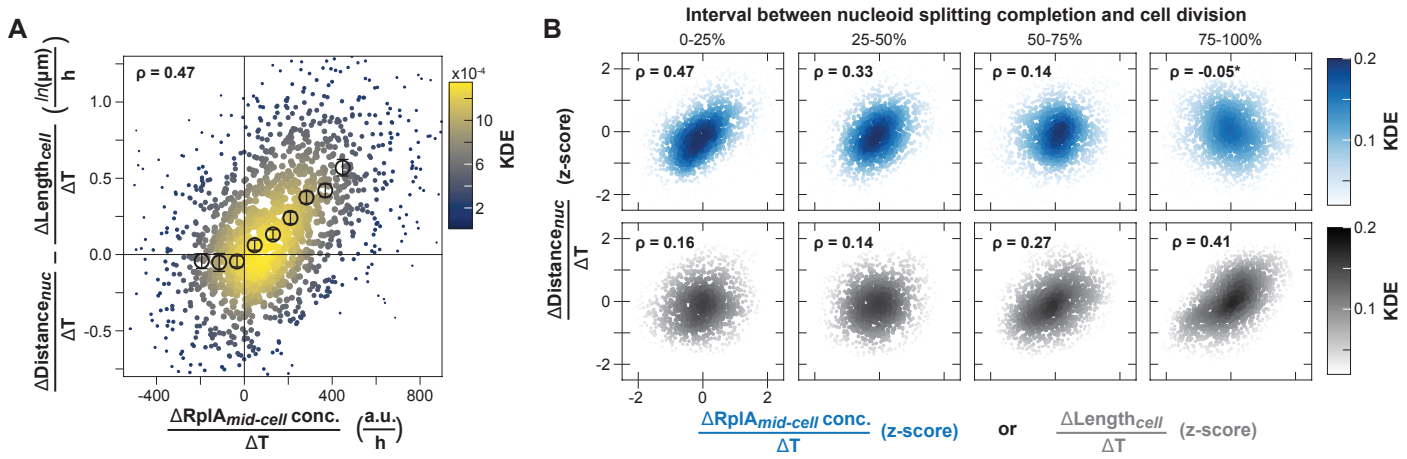

Figure 1 - figure supplement 5

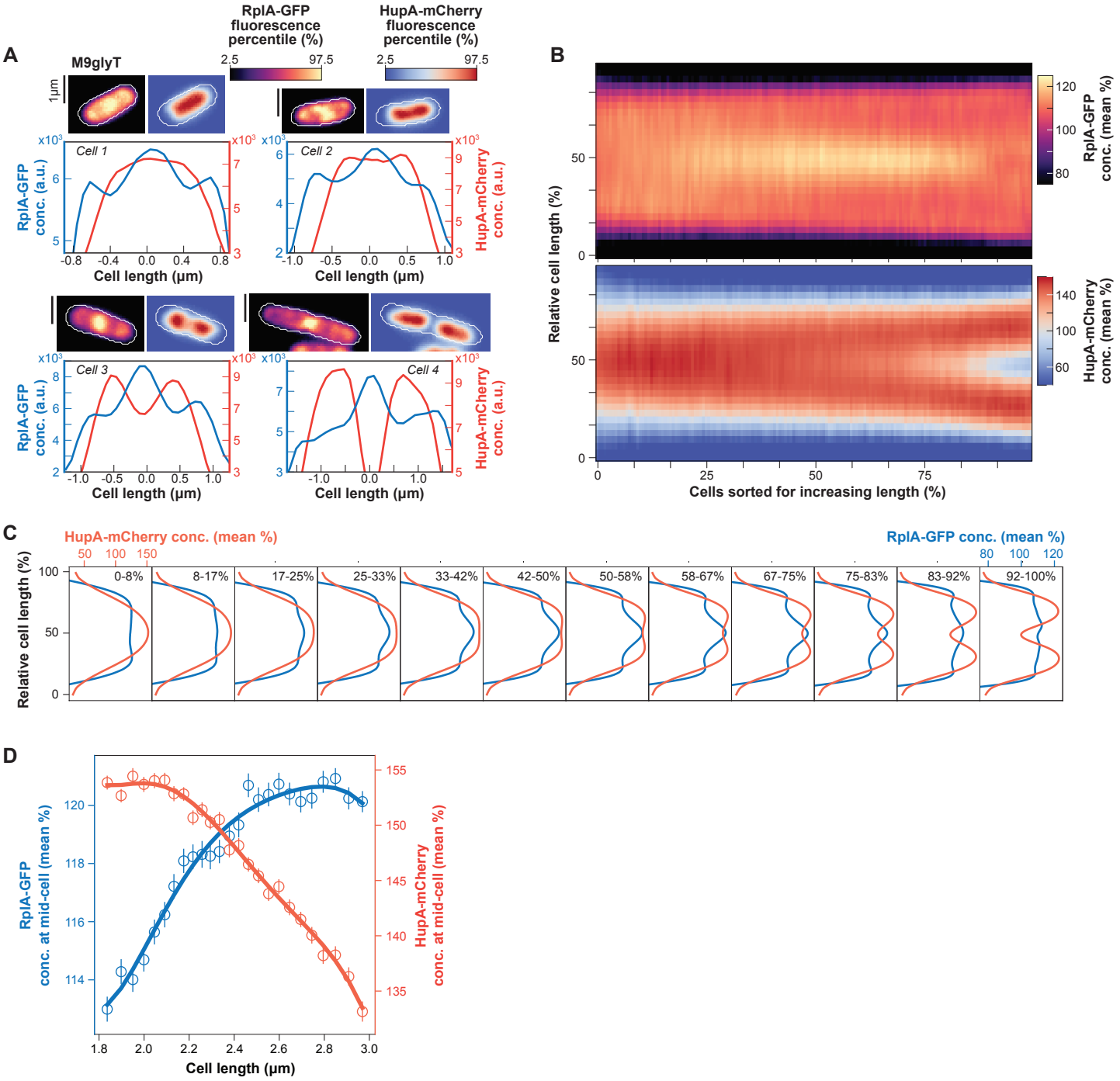

Figure 1 - figure supplement 6

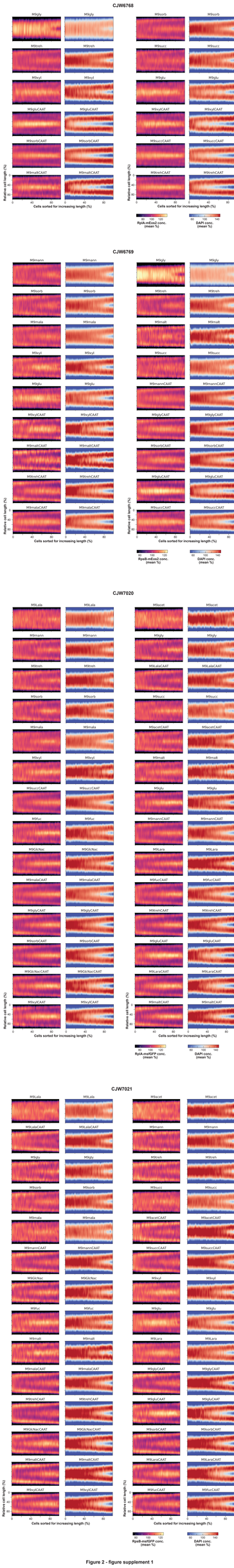

Figure 2 - figure supplement 1

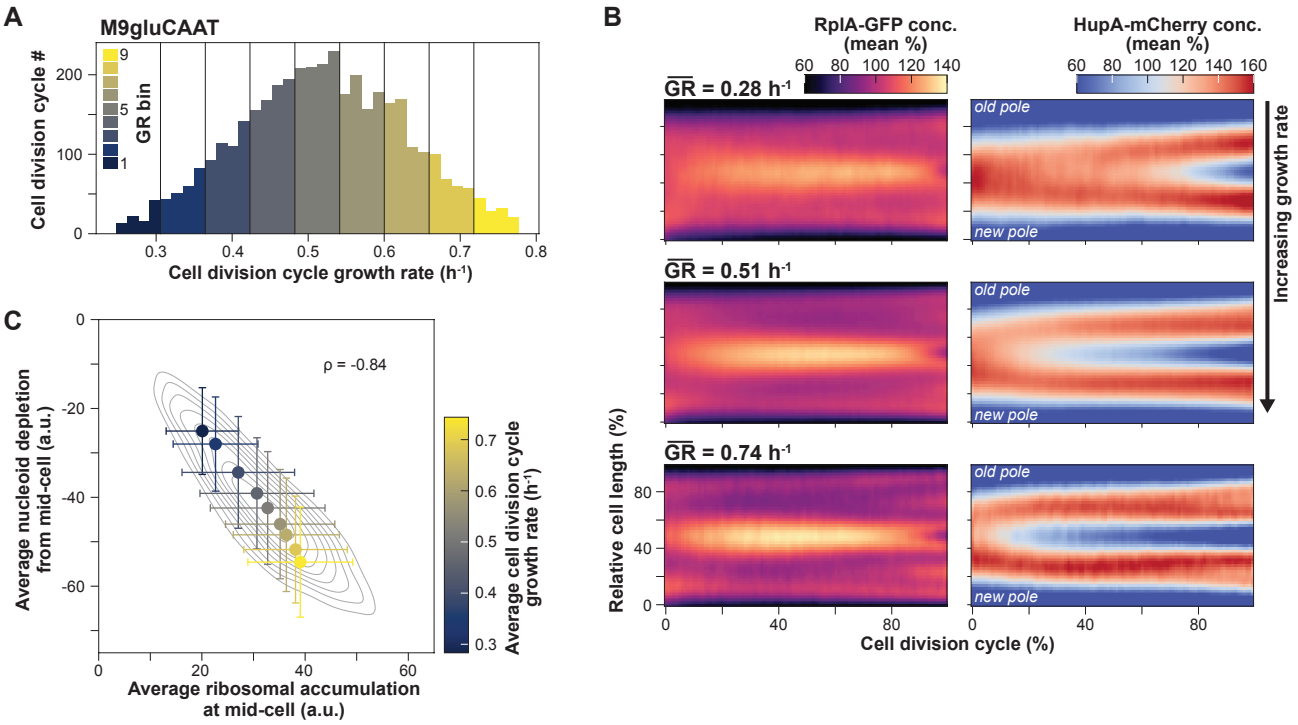

Figure 2 - figure supplement 2

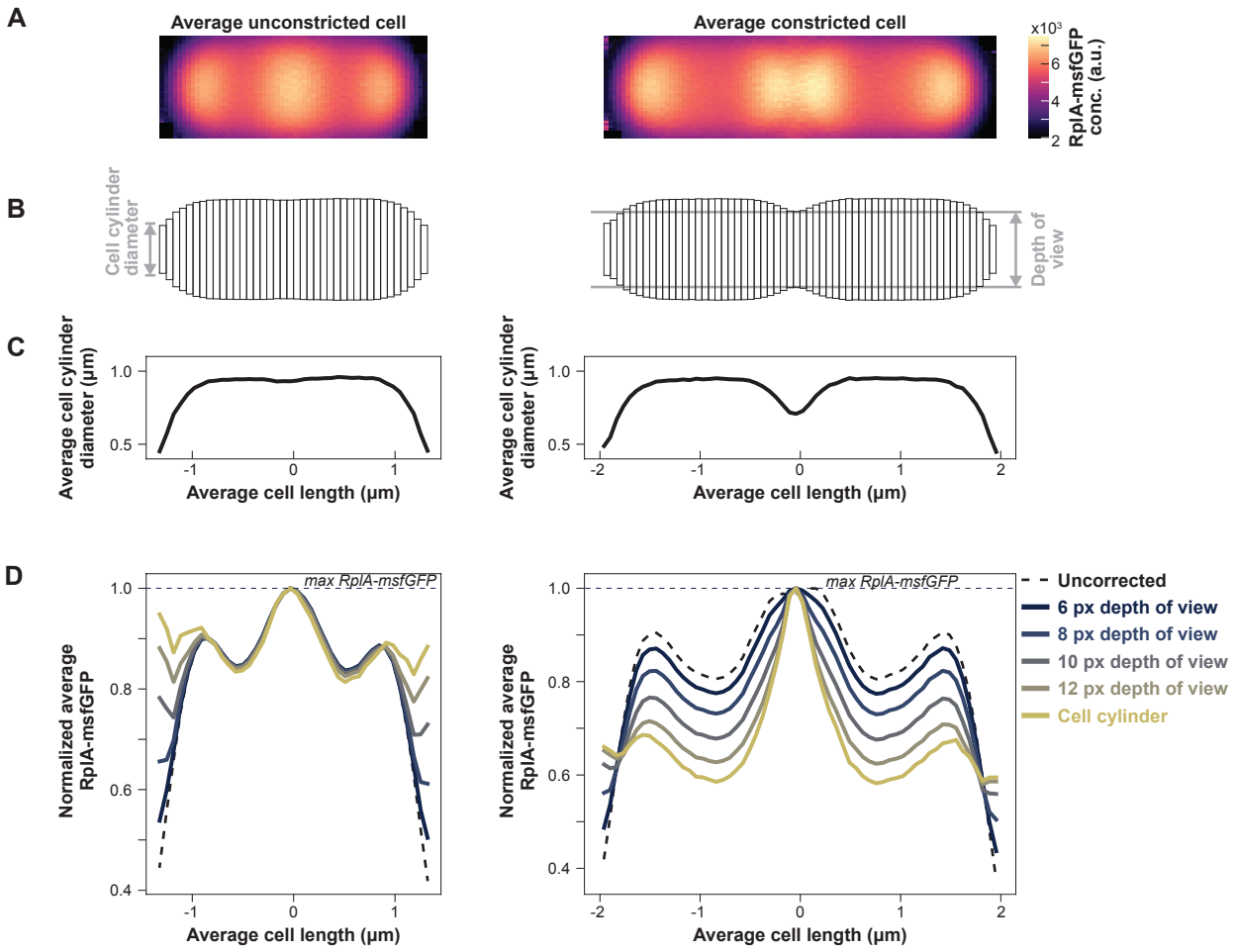

Figure 2 - figure supplement 3

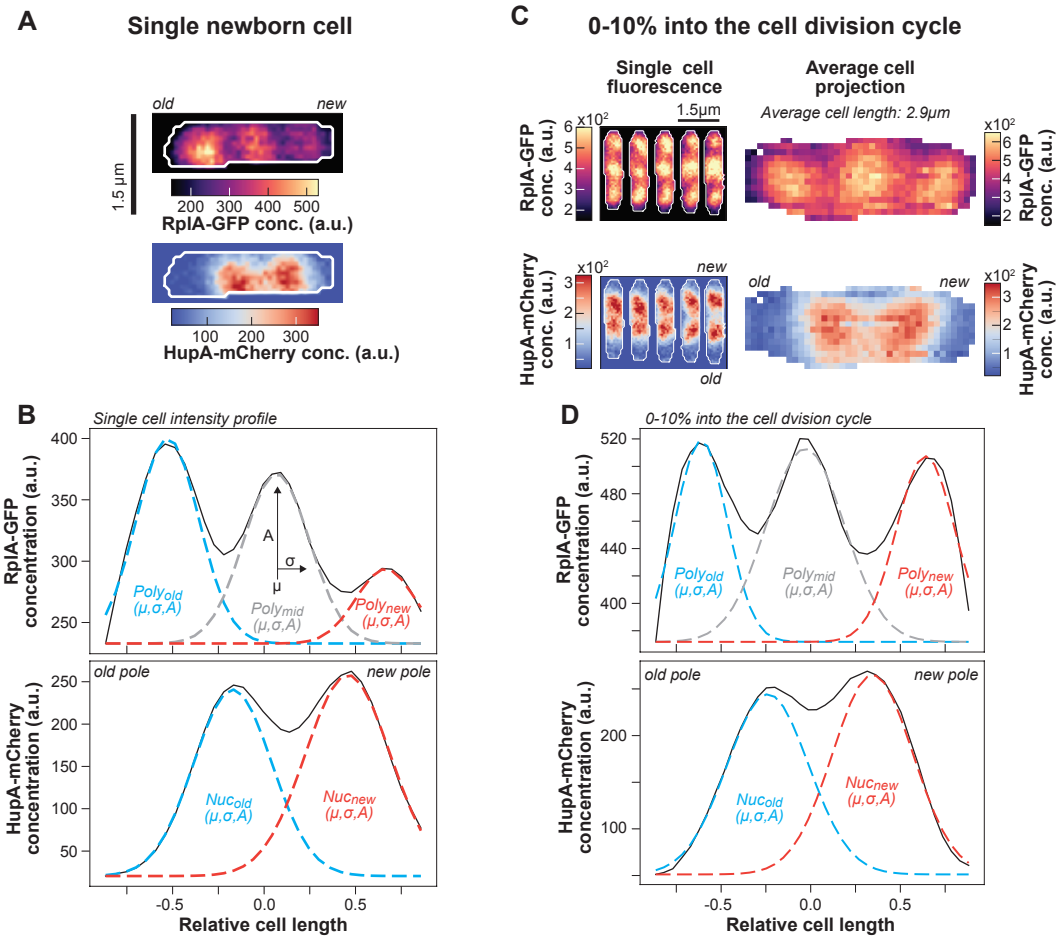

Figure 3 - figure supplement 1

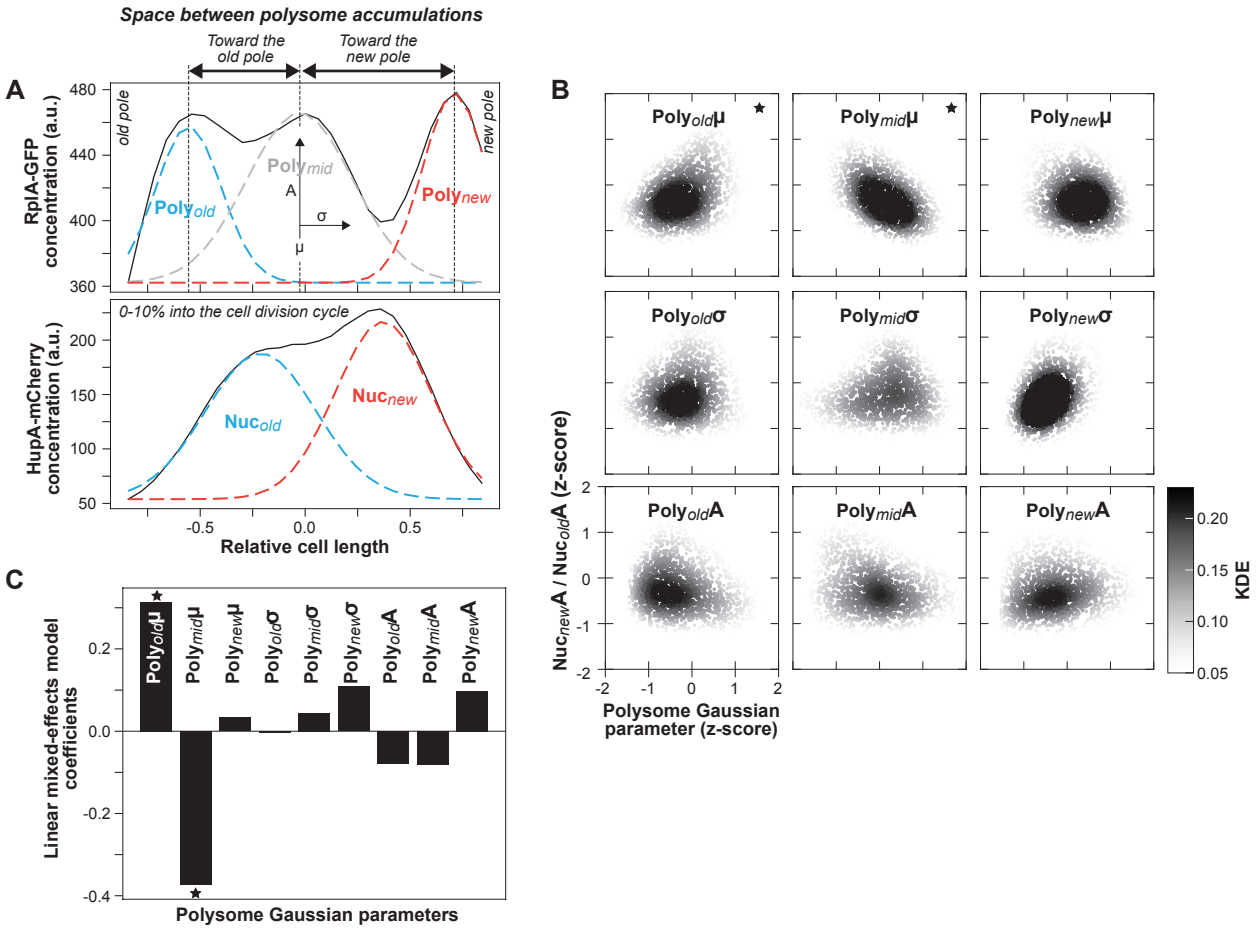

Figure 3 - figure supplement 2

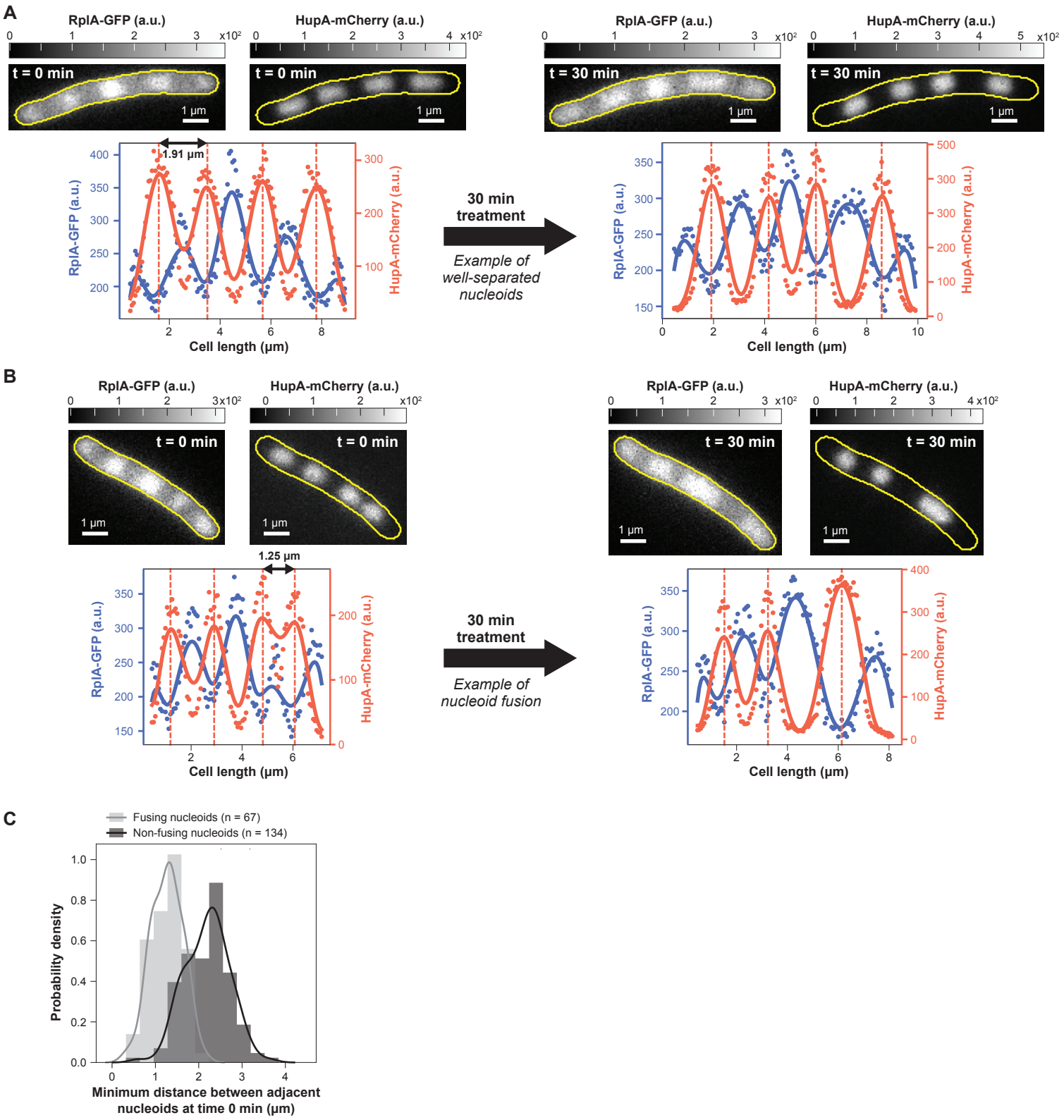

Figure 4 - Figure supplement 1

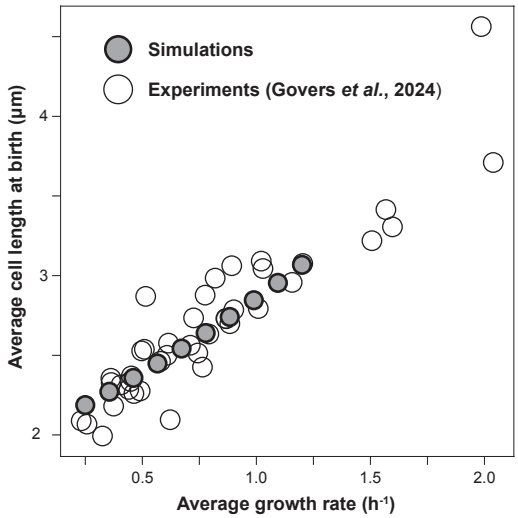

Figure 4 - figure supplement 2

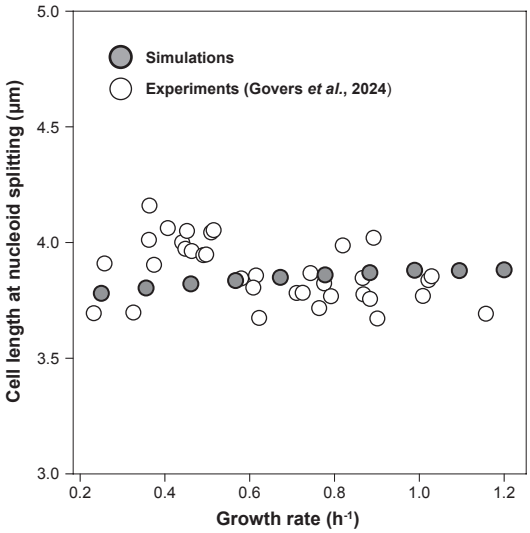

Figure 4 - figure supplement 3

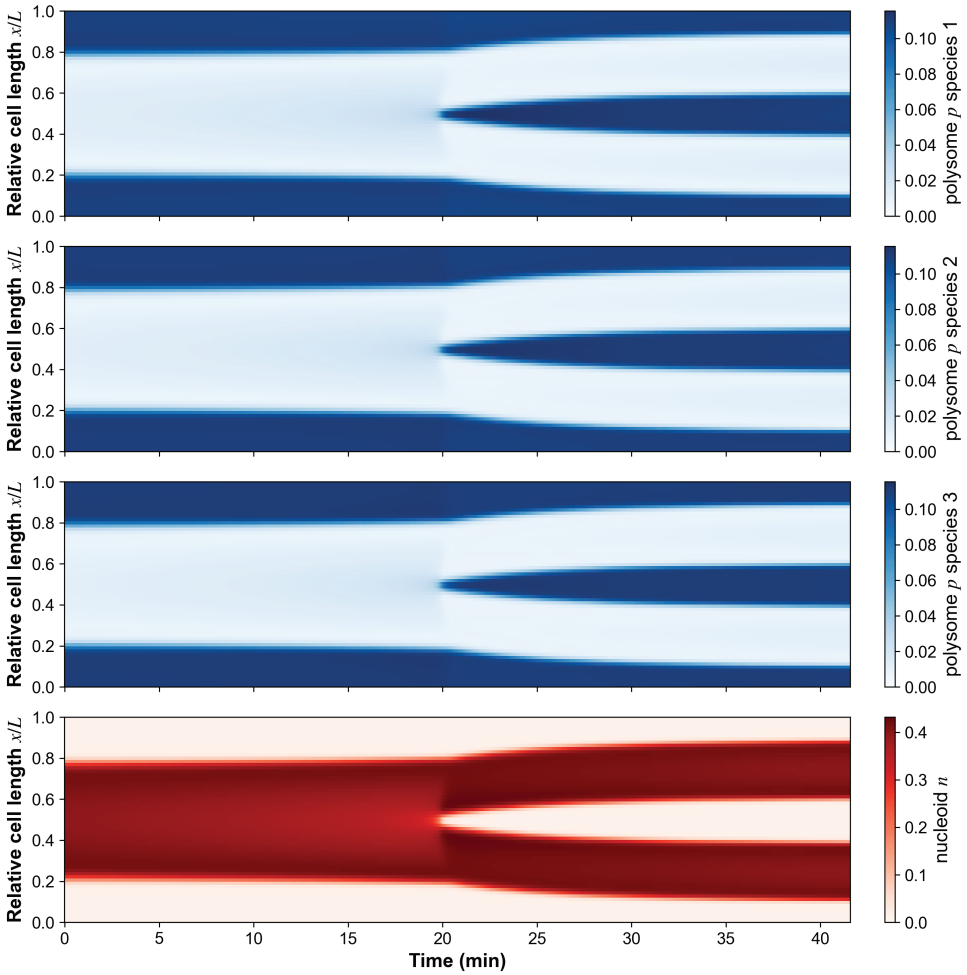

Figure 4 - figure supplement 4

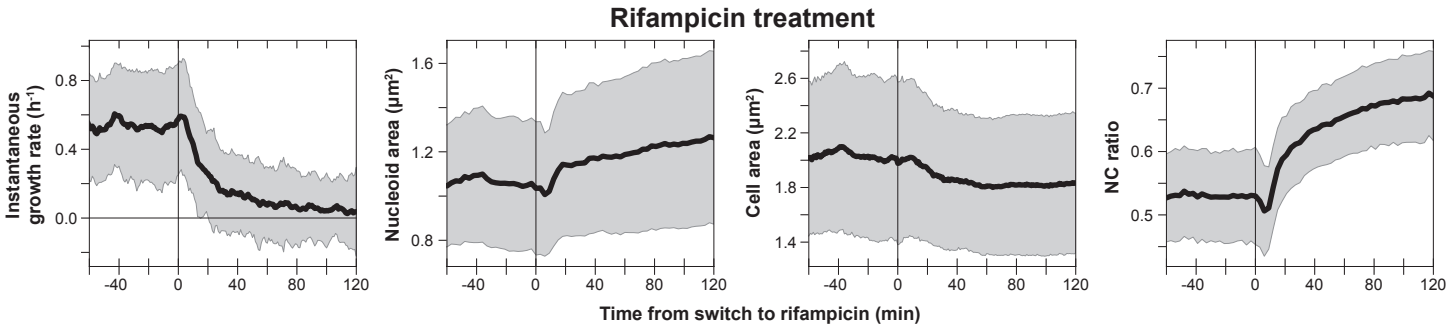

Figure 6 - figure supplement 1

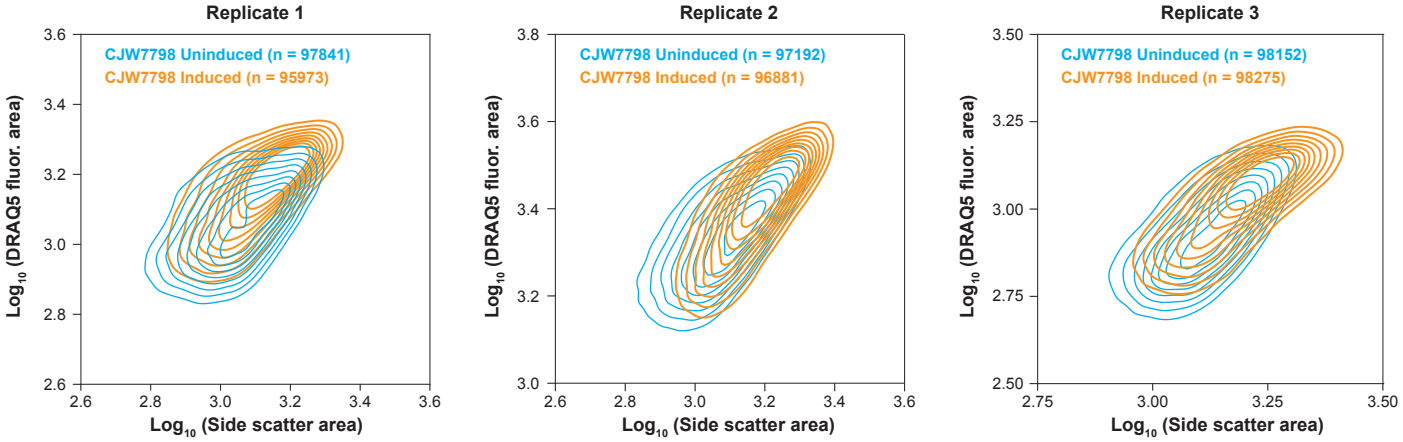

Figure 7 - figure supplement 1

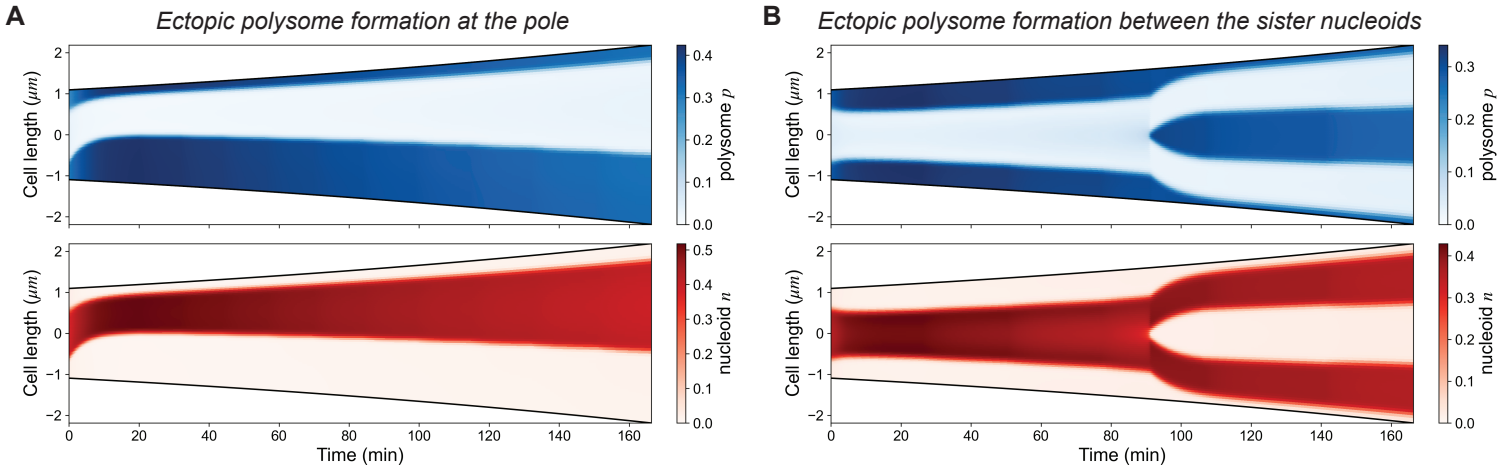

Figure 7 - figure supplement 2

mTagBFP2 over-expression from a plasmid

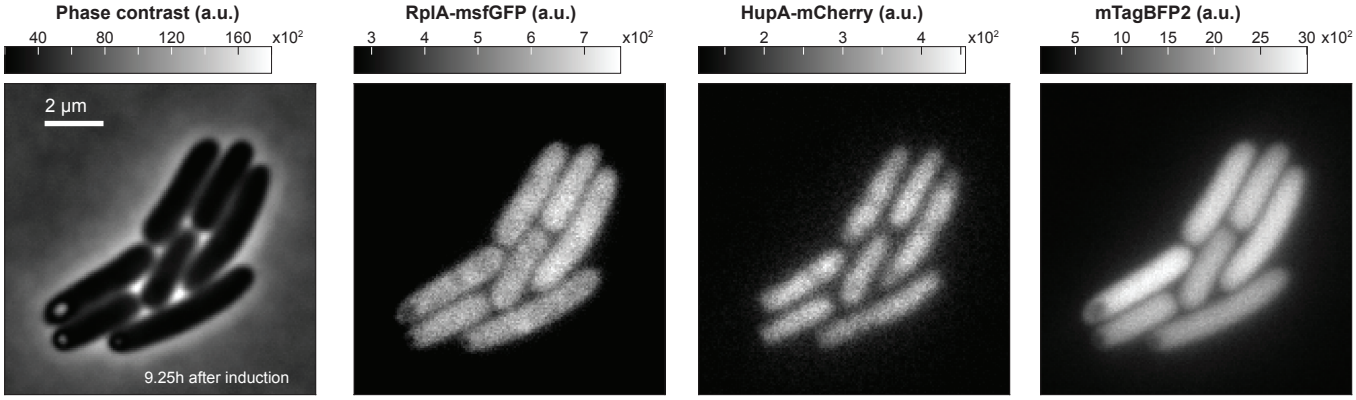

Figure 7 - figure supplement 3

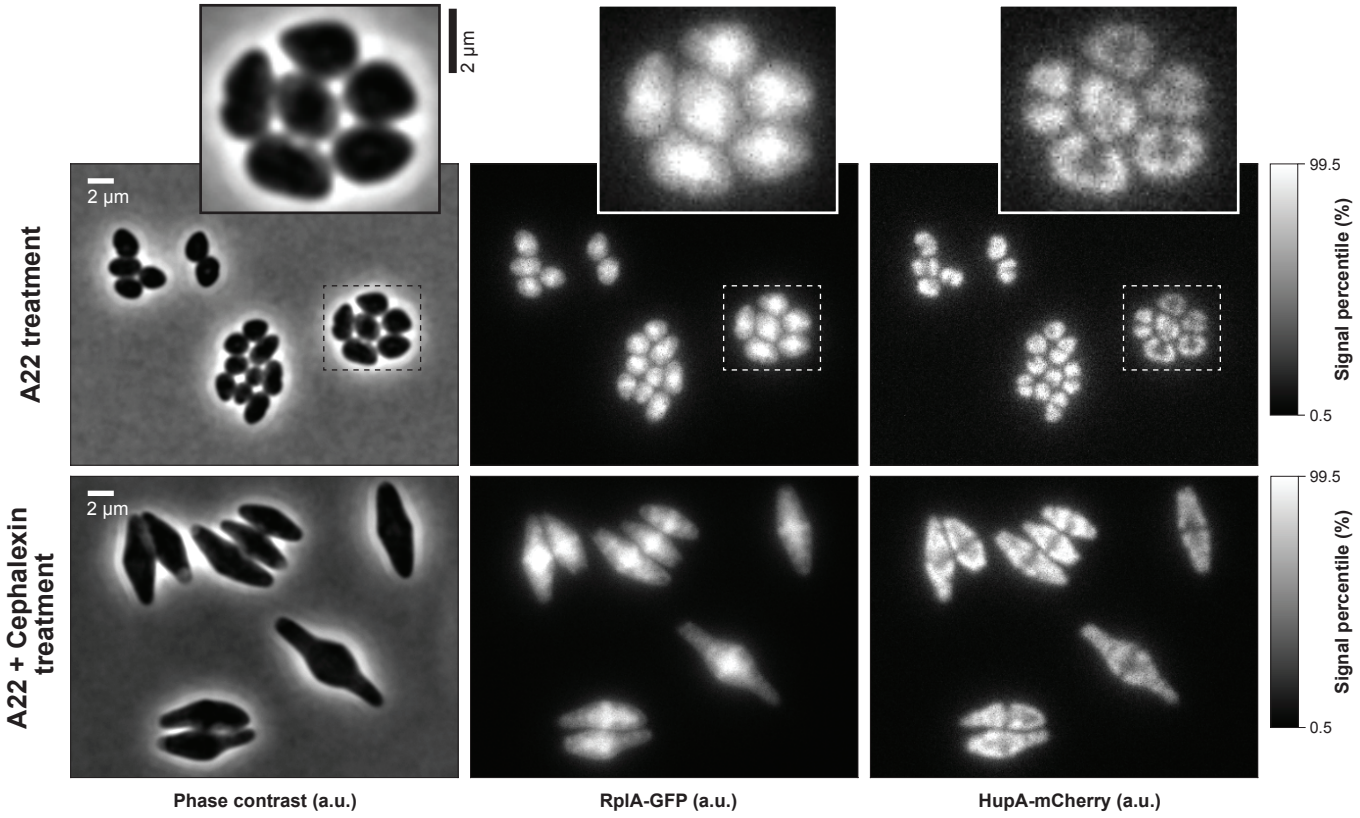

Figure 8 - figure supplement 1